ELECTRON-ELECTRON INTERACTIONS IN SILICON/SILICON-GERMANIUM QUANTUM DOTS

by

HAŞİM EKMEL ERCAN

A dissertation submitted in partial fulfillment of the

requirements for the degree of

DOCTOR OF PHILOSOPHY

(Physics)

at the

UNIVERSITY OF WISCONSIN–MADISON

2021

Date of final oral examination: 3/8/2021

The dissertation is approved by the following members of the Final Oral Committee:
Susan Coppersmith, Professor, Physics
Mark Friesen, Distinguished Scientist, Physics
Mark Eriksson, Professor, Physics
Irena Knezevic, Professor, Electrical and Computer Engineering

Abstract

This thesis discusses the effects of confinement strength on two-electron states in an electrostatically defined quantum dot (QD) in a Si/SiGe quantum well at zero magnetic field, focusing on geometries appropriate for qubits. We account for electron-electron (e-e) interactions via full-configuration interaction calculations as well as the nontrivial interplay between the conduction band valleys of silicon, and disorder at the Si/SiGe interface via tight-binding approach.

We show that the experimental signatures of strong e-e interactions in these devices can be subtle. While the suppression of the singlet-triplet (ST) splitting in two-electron quantum dots formed in direct band gap materials is a clear indication of e-e interactions, in silicon devices this effect can be masked by the additional valley degree of freedom of the conduction band electrons, if the Si/SiGe interface is flat. Interfacial-disorder-induced valley-orbit coupling, on the other hand, can induce this suppression. To study these phenomena, we explore the effects of different interface profiles on the ST splitting.

The presence of the valley degree of freedom in silicon quantum dots enables the existence of excited two-electron states whose excitation energy is less sensitive to e-e interactions than

their counterparts based on orbital excitations. We show that, by virtue of this difference in the sensitivity to e-e interactions, the confinement strength can be used to change the valley vs. orbital character of the first-excited state, with the former yielding excitation energies that are more resilient to charge noise.

We further discuss the role of e-e interactions in two recent experiments demonstrating (1) the use of valley-orbit states to probe Si/SiGe interface, and (2) a spectroscopically-dense set of low-lying energy levels.

Acknowledgments

This thesis is a product of a scientific ecosystem. There are many individuals who deserve the sincerest thanks and gratitude. Among them, first and foremost my advisors Prof. Susan Coppersmith and Dr. Mark Friesen come. Their invaluable support and guidance made this work possible. They have been generous with their time and patient with my failures. They have taught me many lessons on how to conduct a scientific research and how to tell a good scientific story. Thank you Sue, thank you Mark.

Next, I would like to thank Prof. Mark Eriksson for the opportunities of collaboration, and also his numerous suggestions and feedback in preparation for various talks and presentations. In our meetings, I always appreciated Mark's interest in the work I have done, and his effort to find its experimental implications. From the Eriksson group, I especially thank JP Dodson and Joelle Corrigan, who were the driving forces in these collaborations. I enjoyed working with them. I also would like to thank Dr. Sam Neyens, Tom McJunkin and rest of the Eriksson group for many useful conversations and presentations.

I would like to thank current and previous members of the theory group Dr. Joydip

Ghosh, Dr. José Carlos Abadillo-Uriel, Dr. Adam Frees, Dr. Yuan-Chi Yang, Leah Tom, and Merritt Losert with whom I have had many useful discussions.

For the opportunity to benchmark some of my initial computations against theirs, I thank Dr. Mark Gyure and Samuel Quinn.

I also would like to thank Prof. Robert Joynt and his students Dr. Daniel Crow and Dr. Vickram Premakumar for the collaboration in my first project, and many fruitful conversations.

For their time and effort, I would like to express my gratitude to the thesis committee members Prof. Susan Coppersmith, Dr. Mark Friesen, Prof. Mark Eriksson, and Prof. Irena Knezevic.

During my time in Madison, I have had many friends whose company I enjoyed, and support I appreciated: Joel Andersson, Laura Moquin, Justin Walker, Bo Diandian Peng, Nick Anderson, Fang Yun Lim, Kerem Morgül, Yuanyuan Ren, Fırat Yaşar, Çağlar Tanrıkulu, Neslihan Atatimur, Taylan Acar, Mustafa Duman, Vefa Göksel, Serkan Sakar, Ahmet Kabakulak, Bahar İnankur, Pete Mooney, Ian Pozdol, Charity Pozdol, Tara Sliwinski, and Sara Larsen; thank you all. Also, my dear friends who are thousands of miles away but still with me with their messages and calls: Deniz Gezer, Arda Kaplan, Gizem Konukseven, and Ufuk Toraman; thank you.

I also would like to thank my parents Yıldız and Hüseyin, and my brother Alperen for their unconditional love and support. Lastly, I thank my partner Cemre for being the joy of my life. The best part of finishing this adventure will be coming back to you.

Contents

List of Figures

List of Tables

Chapter 1

Introduction

1.1 Introduction

In the last forty years, since Richard Feynman's famous proposal [1], the field of quantum computing has seen many breakthroughs. Developments of quantum algorithms, such as Shor's factoring algorithm [2], have shown that building a quantum computer can solve well-defined and interesting computational problems more efficiently than classical computers and sparked interest in realizing these machines. Today, scientists and engineers are designing and learning to manipulate qubits implemented in various physical platforms including superconducting circuits [3], photons [4], trapped ions [5] and semiconductors [6]. On the applications side, quantum chemistry simulations [7] and optimization problems [8] are areas of active research. With the recent claims of experimental demonstrations that programmable quantum devices can indeed feasibly complete certain computational tasks that

are unfeasible for classical computers [9, 10], quantum computing has become a subject of mainstream interest, with the caveat that these computational tasks are not yet practically useful but are important proofs of principle.

Although there is an ongoing search for practical applications of intermediate-scale implementations that are already realized [11], it is generally believed that very large number of physical qubits (millions) will be needed to achieve the goal of practically useful quantum computing [12]. Central to this requirement is the sensitivity of quantum systems to environmental noise and the consequent need for quantum error correction, which is based on redundancy to recover from errors [13, 14]. Therefore, scalability of the physical implementations is critical. Semiconductor-based qubits are promising in this regard, due to their potential for scalability, which stems from the extensive knowledge base and technological infrastructure built around semiconductors, due to the central role they played in classical computing hardware.

Semiconductor nanostructures can host qubits when they are engineered to trap electrons (or holes) in localized potentials with discrete energy levels, similar to the electronic structure of atoms. Suitable localized potentials are obtained from dopant atoms or quantum dots. For quantum dots, this confinement can be achieved or modified by applying appropriate voltage signals to lithographically-defined metallic gates [15], or by employing self-assembled growth techniques to form charge-trapping islands [16]. Currently, gate-defined quantum dots are more established as qubit platforms, although self-assembled dots are also of interest, due to their optical control and transport properties [17]. Alternatively, dopant-based qubits have

the advantage of very long lifetimes, although due to the small size of their electron wave functions, implementing multiqubit gates is challenging.

Since the milestone proposal of Loss and DiVincenzo [18], various designs of gate-defined quantum dot qubits have been proposed and implemented. These include spin-based [19, 20, 21, 22], charge-based [23, 24, 25, 26], and hybrid [27, 28, 29] platforms. Initial experimental progress in the field was in GaAs/AlGaAs heterostructures [30]. However, due to the presence of ubiquitous nuclear spins, which suppress the qubit coherence by interacting with the spins of the electrons in these devices, attention subsequently turned to Si-based devices, due to the high natural abundance of nuclear spin-zero isotopes, and the possibility of isotropically purifying the silicon to have no nuclear spins [31]. Si/SiGe and Si metal-oxide-semiconductor heterostructures are now commonly used to form gate-defined quantum dot qubits.

In this thesis, we study gate-defined quantum dots in Si/SiGe heterostructures that contain two electrons. In addition to their role in qubit implementations, including quantum dot hybrid qubits [27, 29] and singlet-triplet qubits [19, 20], doubly-occupied quantum dots are excellent systems for studying the interplay between e-e interactions and the disorder at the Si/SiGe interface.

The strength of electron-electron interactions depends on the strength of the confinement. Although the interaction energies increase with increasing confinement, interacting multielectron solutions approach to their noninteracting counterpart when the increase in the single-electron energies is faster. In contrast, decreasing the confinement strength leads to stronger effective interactions that suppress multielectron energy splittings from their

noninteracting values. This is the typical case for quantum dots formed in direct band gap materials like GaAs, where the single electron energies are strictly orbital in nature, and such behavior has been thoroughly studied in literature [32, 33, 34, 35]. Silicon, on the other hand, has an extra degree of freedom coming from its degenerate conduction band minima, referred to as valleys. In bulk Si, this degeneracy is six-fold. In Si/SiGe heterostructures, however, the tensile strain from the lattice mismatch lifts the energies of the valleys in the plane of lateral confinement by about 200 meV, making them inaccessible to low-temperature conduction band electrons in quantum dots [31]. The remaining two-fold degeneracy is broken by a sharp quantum well with a characteristic energy splitting that is usually referred as valley splitting [36]. Valley splitting also depends on the confinement strength, when there is disorder at the Si/SiGe interface that causes hybridization of valley and orbital degrees of freedom [37]. Therefore, multielectron energy spectra in Si/SiGe quantum dots are determined by a nontrivial interplay among e-e interactions, confinement energy, valley splitting and the disorder at the quantum well interface. This full range of phenomena has not been thoroughly explored before. Understanding this interplay is the goal of this thesis.

1.2 Thesis outline

The following two chapters, Chapters 2 and 3, of this thesis focus on the theoretical explorations of interacting electrons in Si/SiGe quantum dots. The next two chapters, Chapters 4 and 5, describe the collaborations with the group of Prof. Mark Eriksson at UW-Madison in theoretical analysis of multielectron Si quantum dot experiments. I carried out tight-binding

and full-configuration interaction calculations and assisted with the theoretical analysis in this collaborations.

In Ch. 2, we study the singlet-triplet (ST) splitting of two electrons in a single dot. We consider a range of orbital confinements relevant to experiments and analyze the effects of different interface profiles on the ST splitting. We show that the suppression of ST splitting from its noninteracting value depends not only on the e-e interaction strength, but also on the strength of valley-orbit coupling. We also describe our computational methods, which employ both tight-binding and full-configuration interaction approaches.

In Ch. 3, we focus on a transition in a first-excited state of two electrons in a single dot that we predict to occur, which is induced by changing the confinement strength. We show that this transition significantly affects the coupling of the first-excited state to a nearby charge trap, with a corresponding impact on the dephasing rates associated with the ST splitting.

In Ch. 4, we discuss measurements of one- and two-electron energies in a single dot. We argue that, in conjunction with electrostatic simulations, our approach could provide an important new probe of the Si/SiGe interface morphology.

In Ch. 5, we discuss measurements of an unusually dense set of low-lying energy levels in a double quantum dot performed by J. Corrigan et al. in the Eriksson laboratory. Using the theoretical machinery described above, we argue that strong e-e interactions are the underlying reason for such behavior.

Appendix E contains our work previously published work on quantum error correction.

Chapter 2

Strong electron-electron interactions in Si/SiGe quantum dots

This chapter is adapted from the manuscript "Strong electron-electron interactions in Si/SiGe quantum dots" by H. Ekmel Ercan, S. N. Coppersmith, and Mark Friesen, which will be submitted for publication.

2.1 Introduction

Silicon quantum dots are of great current interest because of their desirable properties as qubits [18, 31, 6, 38, 29, 39, 40, 41, 42, 43], including the high natural abundance of spin-0 nuclear isotopes, and the possibility of leveraging the infrastructure of the semiconductor industry for scale-up. Device uniformity plays a key role in scale-up, and recent, new fabrication schemes have demonstrated improved control over geometry-influenced device

parameters, including dot confinement energies and tunnel barriers [44, 45, 46, 47, 48, 49]. However, new physics enters the picture for dots and qubits with more than one electron [50, 29, 51, 52, 53, 54, 55], making it more difficult to achieve uniformity. Electron-electron (e-e) interactions present a particular challenge, both from control and design perspectives, since they are so sensitive to many factors. A comprehensive and quantitative theoretical understanding of e-e interactions and the contributing physics is therefore highly desirable.

Strong e-e interactions occur in dots with low electron densities give rise to electron localization in the form of Wigner molecules [56, 32, 34, 57, 33], which are finite-size analogs of Wigner crystals [58, 59]. Experimental signatures of Wigner molecules include the suppression of multi-electron excitation energies, which has been observed in GaAs [60] and Ga[Al]As [35] dots and carbon nanotubes [61]. A detailed understanding of these charge distributions is particularly important for qubit applications, because of the need to precisely control the qubit energy splittings and tunnel couplings. Here we show that e-e interactions are particularly subtle for dots formed in SiGe/Si/SiGe quantum wells, because of the degeneracy of the low-lying conduction-band valleys [62, 63, 64]. These many-body effects depend on the interplay between the underlying valley degree of freedom, which is strongly affected by disorder at the Si/SiGe quantum well interface [65, 36, 66, 37, 67, 68, 69, 70, 71], and the additional orbital and spin degrees of freedom.

The importance of e-e interactions can be estimated from the Wigner ratio $R_W = E_{\mathrm{Coul}}/E_{\mathrm{orb}}$, relating the Coulomb energy, E_{Coul}, to the single-electron orbital splitting, E_{orb}.

Here, we assume a simple parabolic confinement potential, $m_t\omega^2 x^2/2$, where m_t is the effective mass in the plane of the quantum well. The corresponding orbital energy is given by $E_{\rm orb} = \hbar\omega$, the dot radius is given by $a_0 = \sqrt{\hbar/m_t\omega}$, and the characteristic Coulomb energy is given by $E_{\rm Coul} = e^2/4\pi\epsilon a_0$. As expected, the Coulomb energy increases with confinement strength; however, the orbital energy increases faster, resulting in e-e interactions that increase with dot size. For two-dimensional (2D) circular dots, it has been theoretically estimated that Wigner molecules should emerge when the Wigner parameter $R_W \gtrsim 1.5$ [32]. Such behavior has been experimentally confirmed in GaAs dots [35]. For Si dots, the $R_W = 1.5$ criterion corresponds to $\hbar\omega = 18$ meV; however, orbital energies are typically of order $\hbar\omega \sim 1$ meV, which corresponds to $R_W = 6$. We therefore expect Si qubits to be in the strongly interacting regime.

Valley physics plays a critical role with regards to e-e interactions. For SiGe/Si/SiGe quantum wells, the presence of a sharp interface lifts the two-fold degeneracy of the conduction-band valleys. However, this valley splitting is suppressed well below the orbital splitting, due to the unavoidable interfacial disorder present in realistic devices [36, 37]. The valley ratio $E_{\rm Coul}/E_{\rm val}$ is therefore even larger than $R_W = E_{\rm Coul}/E_{\rm orb}$. While several previous calculations explore e-e interactions in silicon dots [72, 73, 74, 75, 76], including Wigner molecule effects [77], none includes the realistic disorder profiles that are key for understanding the valley physics.

In this chapter we investigate the combined effects of e-e interactions and valley-orbit couplings (VOC) on the energy states of a single quantum dot containing two electrons. We

focus on the ground state (a singlet), and the first two excited triplet states. Such single-dot ST energy splittings are key for many quantum computing applications. This obviously includes ST qubits, particularly when tuned towards the readout regime [19, 20].

For the quantum hybrid qubit, the qubit energy splitting is largely determined by the ST splitting in the dot containing two electrons [27, 28, 29, 78, 79, 80, 81, 82, 83]. Large ST splittings are also key requirements for readout methods based on Pauli spin blockade [84, 85, 86, 87].

Special nonperturbative techniques are needed to treat strong e-e interactions, particularly in the Wigner molecule regime, where two-electron wavefunctions have very different charge distributions than the low-lying single-electron eigenstates. Here, we use the full configuration interaction (FCI) method, in which multi-electron Hamiltonians are expanded in large sets of "configurations," which are in turn constructed from symmetrized products of single-electron eigenstates. Special techniques are also required to treat VOC, which arises due to atomic-scale disorder at the Si/SiGe quantum-well interface. (Here, we use the terminology "valley-orbit coupling" to describe the mixing of valley and orbital states that would otherwise represent good quantum numbers in the absence of interfacial disorder. This is in contrast with some other authors that use the term interchangeably with "valley splitting".) In this case, we employ a minimal tight-binding (TB) model [62, 88, 37, 89] to compute the single-electron basis states that are incorporated into the FCI calculations. This combination of methods is powerful and unique, allowing us to explore the diverse and unexpected behavior observed in Si qubit experiments [82, 90].

The main results of the present calculations are summarized as follows. A key experimental parameter for tuning e-e interactions is the orbital (i.e., lateral) confinement potential; we adopt this as the main tuning parameter in our simulations. We then explore the combined effects of e-e interactions and VOC in stages. First, we effectively turn off the VOC by considering a perfectly flat quantum well interface, with no atomic-scale disorder. In this case, "valley" and "orbital" are good quantum numbers for the single-electron eigenstates, and these symmetries are also conferred upon the two-electron wavefunctions. The resulting ground state is a singlet, while the lowest excited states are triplets, comprised of configurations with either excited valley states or excited orbital states, but not both. For weak confinement, the orbital triplet has the lowest energy, while for strong confinement, the valley triplet has the lowest energy. Although the charge distributions of all two-electron wavefunctions are affected by e-e interactions, and may even form Wigner molecules for weak confinement, it is interesting that only the orbital ST splitting is found to depend on the confinement strength. The valley ST splitting is protected by the valley symmetry, and remains unaffected by the confinement, with a value nearly identical to the valley splitting. As a result, the low-energy excited state switches from an orbital triplet (for weak confinement) to a valley triplet (for strong confinement). This crossover occurs in a regime that is typically relevant for quantum dot qubit experiments.

Next, we introduce atomic-scale steps at the quantum-well interface, resulting in VOC that hybridizes the valley and orbital states, and suppresses the valley splitting. Typically, we want a VOC that is fairly weak, so that it yields ST splittings appropriate for qubit

Table 2.1: Some symbols and abbreviations used in this work.

Symbol	Description
S	Low-energy singlet
$\mathrm{T}_{\mathrm{val}}$	Low-energy valley triplet
$\mathrm{T}_{\mathrm{orb}}$	Low-energy orbital triplet
ST	Single-triplet (qubit)
FCI	Full configuration interaction
TB	Tight binding
e-e	Electron-electron (interactions)
FFT	Fast Fourier transform
VOC	Valley-orbit coupling
E_{val}	Valley splitting
E_{orb}	Orbital splitting
E_{S}	Singlet energy
$E_{\mathrm{T}_{\mathrm{val}}}$	Valley-triplet energy
$E_{\mathrm{T}_{\mathrm{orb}}}$	Orbital-triplet energy
$E_{\mathrm{ST}_{\mathrm{val}}}$	$E_{\mathrm{T}_{\mathrm{val}}} - E_{\mathrm{S}}$
$E_{\mathrm{ST}_{\mathrm{orb}}}$	$E_{\mathrm{T}_{\mathrm{orb}}} - E_{\mathrm{S}}$
E_{ST}	$\min(E_{\mathrm{ST}_{\mathrm{val}}}, E_{\mathrm{ST}_{\mathrm{orb}}})$
E_{Coul} or E_{ee}	Coulomb-interaction energy
D	Dot diameter
W	Step separation
x_s	Step position
$d = \lvert x_s \rvert$	Distance from dot to nearest step

applications. In this regime, 'valley' is no longer a good quantum number; however, the triplet states remain approximately valley-like or orbital-like, and the valley ST splitting is approximately equal to the valley splitting. The orbital ST splitting is suppressed by VOC – in some cases quite significantly – and the different triplet states hybridize, so that the first excited state can be tuned continuously from valley-like to orbital-like, as a function of the confinement strength.

An important take-home message from this analysis is that, in the strongly confined regime, when large ST splittings are observed in experiments, they provide evidence of weak interfacial disorder; the measured ST splitting is then nearly equal to the valley splitting. In this regime, the ST splitting is robust against small changes in the device tuning. However, as the confinement is further reduced, there is eventually a transition to a very different regime, marked by strong e-e interactions and suppressed ST splittings.

The chapter is organized as follows. A summary of symbols and abbreviations is presented in Table 2.1. In Sec. 2.2, we describe the two-electron quantum dot Hamiltonian, and the TB and FCI methods used to solve it. An overview of our main results is presented in Sec. 2.3.1, with further details described in the remainder of the section. In Sec. 2.4, we summarize our results and conclude. The Appendices provide technical details about the methods used.

2.2 Methods

This section presents the system Hamiltonian and calculational methods used in this work. Sec. 2.2.1 presents the Hamiltonian, Sec. 2.2.2 describes the TB methods used to

compute the single-electron eigenstates, and Sec. 2.2.3 describes the FCI methods used to compute the two-electron eigenstates.

2.2.1 Hamiltonian

We consider a quantum dot containing two electrons, with Hamiltonian

$$H^{2e} = H^{1e}(\boldsymbol{r}_1) + H^{1e}(\boldsymbol{r}_2) + H_{\text{int}}(\boldsymbol{r}_1, \boldsymbol{r}_2), \tag{2.1}$$

where H^{1e} are the single-electron Hamiltonians, $H_{\text{int}} = \frac{e^2}{4\pi\epsilon_0\epsilon_r}\frac{1}{|\boldsymbol{r}_1-\boldsymbol{r}_2|}$ is the Coulomb interaction, e is the electron charge (with $e > 0$), ϵ_0 is the vacuum permittivity, and $\epsilon_r = 11.4$ is the dielectric constant of low-temperature Si [91]. Here, $\hat{z}$ is defined as the crystallographic [001] axis, although the quantum-well interface may not be perfectly aligned with $\hat{z}$, as depicted in Fig. 2.1(a).

The single-electron Hamiltonians are defined as

$$H^{1e} = H_{\text{K}} + H_{\text{E}} + H_{\text{QW}}, \tag{2.2}$$

where the kinetic energy H_{K}, the lateral confinement potential H_{E}, and the vertical confinement potential H_{QW} are described below.

To account for VOC and atomic-scale disorder, we adopt an atomistic Hamiltonian in the x-z plane. We specifically consider the empirical two-band TB model of Refs. [62], as illustrated in Fig. 2.1(d), which is known to give valley splitting results comparable to more

realistic models [62, 88, 36]. To improve the computational efficiency of our calculations, we adopt a continuous Hamiltonian in the third dimension (along $\hat{y}$). The only constraint imposed by this choice is that the interfacial disorder profile (e.g., the atomic steps) must be uniform along $\hat{y}$, as shown in Fig. 2.1(a); this constraint does not affect any of our conclusions. With a proper choice of confinement potentials, $H^{1e} = H^{1e}_{\mathrm{x,z}} + H^{1e}_{\mathrm{y}}$, the resulting single-electron calculations are separable. The kinetic energy is thus given by

$$H_{\mathrm{K}} = \frac{-\hbar^2}{2m_t}\frac{\partial^2}{\partial y^2} + \sum_{i,j=0,\pm1,\ldots} \left(t_1 \left|i,j+1\right\rangle \left\langle i,j\right| + t_2 \left|i,j+2\right\rangle \left\langle i,j\right| + t_3 \left|i+1,j\right\rangle \left\langle i,j\right| + \mathrm{h.c.}\right), \quad (2.3)$$

where the indices i and j refer to TB sites along the $\hat{x}$ and $\hat{z}$ axes, respectively. The $\hat{z}$ hopping parameters, $t_1 = 0.68$ eV and $t_2 = 0.61$ eV, are chosen to give the correct longitudinal effective mass for Si, $m_l = 0.916\ m_0$, and the correct positions of the valley minima in the Brillouin zone, $k_0 = \pm 0.82(2\pi/a)$, where $a = 5.43$ Å is the Si lattice constant, and the grid spacing is taken to be $\Delta z = a/4$ [88]. The $\hat{x}$ hopping parameter, $t_3 = -0.026$ eV, is chosen to yield the correct transversal effective mass for silicon, $m_t = 0.191\ m_0$. Here, we choose a grid spacing of $\Delta x = 2.79$ nm for most of our calculations [1]. We note that grid spacings along $\hat{x}$ can be much larger than along $\hat{z}$, as there are no fast valley oscillations along $\hat{x}$.

The quantum well confinement potential is defined as

$$H_{\mathrm{QW}} = \sum_{i,j=0,\pm1,\ldots} \left[E_0 + V_{\mathrm{QW}}\Theta_{i,j} - e(iF_x\Delta x + jF_z\Delta z)\right] \left|i,j\right\rangle \left\langle i,j\right|, \quad (2.4)$$

[1] The only exception is Fig. 2.3(a). In this case, the grid spacing, Δx, is chosen to be smaller (0.47 nm, yielding $t_3 = -0.93$ eV), since the confinement strength is stronger for this calculation.

as illustrated in Fig. 2.1(b). Here, E_0 is a uniform energy shift, $V_{\mathrm{QW}} = 150$ meV is a typical band offset between Si and SiGe, and $\Theta_{i,j}$ is a step function that takes the value 1 on a SiGe site and 0 on a Si site. $\boldsymbol{F} = (F_x, 0, F_z)$ is a uniform electric field produced by a top-gate electrode, oriented perpendicularly to the average quantum-well interface. In this work, we considered equally spaced, single-atom steps at all interfaces, resulting in an average interface tilt that determines the orientation of $\boldsymbol{F}$. We refer to such disorder as a 'tilted interface.'

Finally, the electrostatic confinement potential is assumed to be harmonic along both $\hat{x}$ and $\hat{y}$:

$$H_{\mathrm{E}} = \frac{1}{2} m_t \omega_x^2 \sum_{i,j=0,\pm 1,\ldots} (i\Delta x)^2 \left|i,j\right\rangle \left\langle i,j\right| + \frac{1}{2} m_t \omega_y^2 y^2, \tag{2.5}$$

as illustrated in Fig. 2.1(c).

2.2.2 Single-electron wavefunctions

The first step in our solution procedure is to compute the single-electron energy eigenstates. We therefore solve $H^{1\mathrm{e}}\phi_i = \varepsilon_i \phi_i$ by leveraging the separability of the Hamiltonian, $H^{1e} = H^{1e}_{\mathrm{x,z}} + H^{1\mathrm{e}}_{\mathrm{y}}$. The TB Hamiltonian $H^{1e}_{\mathrm{x,z}}$ is numerically diagonalized to obtain the wavefunctions $\zeta_{n_{x,z}}(x,z)$, where the labels $n_{x,z}$ denote the valley and orbital modes. We choose the spatial domain in the x-z plane to be large enough that the wavefunctions have already vanished before reaching the boundaries. Some typical wavefunction solutions for $|\zeta_{n_{x,z}}(x,z)|^2$ are shown in Fig. 2.1(e) for a tilted interface. Note that confinement along $\hat{z}$ is strong enough that only the lowest subband is relevant for our calculations. As $H^{1\mathrm{e}}_{\mathrm{y}}$ is taken to describe a harmonic oscillator in this work, the corresponding wavefunctions $\eta_{n_y}(y)$ may

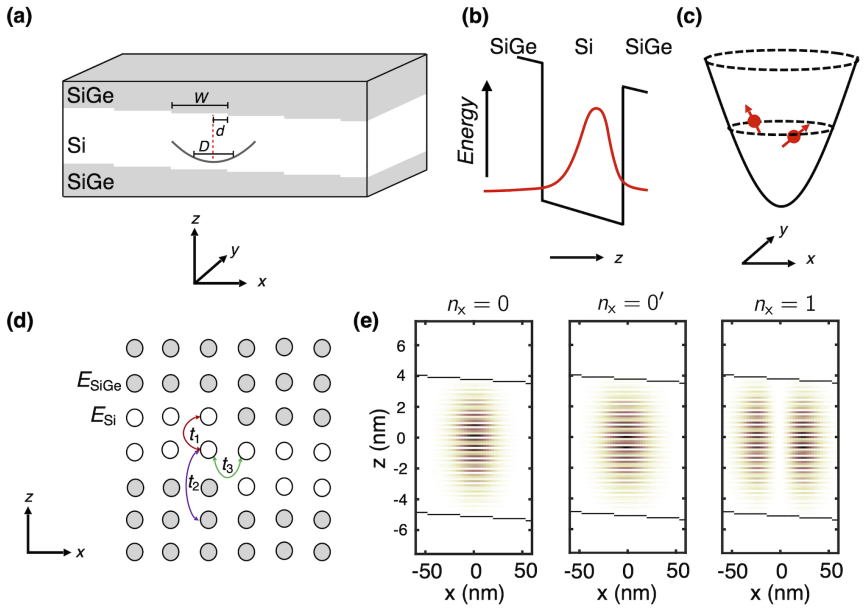

Figure 2.1: Simulation and TB geometries used for single-electron calculations. (a) Schematic of the Si/SiGe heterostructure in the vicinity of the quantum well. The Si quantum well is depicted as white, while the SiGe barriers are depicted as gray. Interfacial disorder is represented as single-atom steps of width W. A quantum dot of diameter D is formed within the quantum well, with separation d between the center of the dot and the nearest step edge. (b) Band offsets at the heterostructure interface, with an applied electric field perpendicular to the interface, confine electrons in the quantum well. The red curve represents the z-envelope of an electron wavefunction. Fast valley oscillations of the wavefunction are not shown. (c) Electrostatic confinement in the x-y plane is provided by top gates (not shown). We approximate the 2D potential as harmonic. (d) TB model and hopping parameters t_1, t_2, and t_3 in the x-z plane. On-site parameters for SiGe (gray) and Si (white) allow for the inclusion of atomic steps at the interface. Note that the lattice shown here is only schematic; the number of TB sites used in the calculations is actually much higher ($\sim 10^4$). (e) Typical TB density results for the ground state ($n_x = 0$), the first valley-excited state ($n_x = 0'$), and the first orbitally excited state ($n_x = 1$). Although atomic steps at the interface cause VOC, it is usually possible to distinguish valley-like and orbital-like excitations. Note that confinement along $\hat{y}$ is treated independently here, due to the separation of variables, and that excited z subbands do not enter our calculations as their energies are very high.

be obtained analytically, as described in Sec. A.2. The full single-electron wavefunctions $\phi_{n_{x,z},n_y}(x,y,z) = \zeta_{n_{x,z}}(x,z)\eta_{n_y}(y)$ are then employed as basis states in the FCI calculations, described below.

2.2.3 Two-electron wavefunctions

The single-electron wavefunctions, computed above, represent exact solutions in the absence of Coulomb interactions, $H_{\rm int}(\boldsymbol{r}_1, \boldsymbol{r}_2)$. However, the strong e-e interactions of interest here cannot be treated pertubatively. We therefore adopt the well-known FCI procedure to solve for the two-electron wavefunctions [92]. This exact diagonalization technique is frequently used in quantum chemistry applications and has also been used to study quantum dot systems [56, 93, 94, 95, 96, 60, 97, 98, 99, 75, 76, 100, 101, 102].

In the FCI approach, we use a complete basis set of single-electron wavefunctions $\{\phi_i\}$ to construct a complete basis set of two-electron wavefunctions $\{\psi_\alpha\}$. The basic procedure has two steps. First, we combine the orbital wavefunctions with spin wavefunctions to form spin orbitals. Here, we use the shorthand notataion $\chi_{2i} = \phi_i \otimes \uparrow$ and $\chi_{2i+1} = \phi_i \otimes \downarrow$. Next, we combine two of these spin orbitals and ensure that they have proper fermionic symmetry by computing their Slater determinants, $\psi_\alpha = |\chi_m \chi_n\rangle$, using the notation of Ref. [92] to denote Slater determinants. The resulting states are referred to as configurations. The set of all possible configurations, obtained from all possible spin-orbital combinations, forms a complete basis set for expanding the two-electron Hamiltonian. A general eigenstate Ψ of

H^{2e} can therefore be expressed as

$$\Psi = \sum_{\alpha=0}^{\infty} c_\alpha \psi_\alpha. \tag{2.6}$$

Slater determinants are not necessarily spin eigenstates; however it is straightforward to combine configurations to obtain such spin-adapted configurations, $\psi_\alpha^{(\mathrm{ST})}$ [92]. Hence, we can also write

$$\Psi = \sum_{\alpha=0}^{\infty} c_\alpha^{(\mathrm{ST})} \psi_\alpha^{(\mathrm{ST})}. \tag{2.7}$$

In practice, it is not possible to work with an infinite basis set. We therefore truncate the single-electron bases to a set of size K, which is large enough that the results are not significantly affected when K is increased. Typically, we find that $K = 42$ is sufficient for our simulations, corresponding to six single-electron orbital shells. The full calculation therefore involves $2K$ spin orbitals and $\binom{2K}{2} = 3486$ configurations.

Calculating the H^{2e} matrix elements involves solving two types of integrals: $\langle\psi_\alpha| H^{1e}(\boldsymbol{r}_i) |\psi_\beta\rangle$ and $\langle\psi_\alpha| H_{\mathrm{int}} |\psi_\beta\rangle$. The first type can easily be reduced to single-electron integrals whose values are known from the single-electron calculations. The remaining Coulomb integrals are, by far, the most computationally expensive part of the simulation, since the number of unique integrals scales as K^4. It is therefore desirable to identify an efficient computational method for performing these integrals. Here, we adopt a scheme [103] that allows us to exploit fast Fourier transform (FFT) algorithms, which are numerically efficient. Additionally, having incorporated separability into our single-electron Hamiltonians, we can exploit the harmonic oscillator wavefunctions $\eta_{n_y}(y)$ to compute the y integrals

analytically. This allows us to replace the 3D Coulombic interaction $1/r$ with an effective 2D interaction $\tilde{f}$ in the $k_x - k_z$ Fourier plane. The resulting electrostatic potential from the electron 1 is given by

$$V(x,z) = \int dk_x dk_z e^{2\pi i(k_x x + k_z z)} \tilde{f}(k_x, k_z) \tilde{\rho}^{(1)}(k_x, k_z), \tag{2.8}$$

where $\tilde{\rho}^{(1)}(k_x, k_z)$ is the Fourier transform of $\rho^{(1)}(x,z) \equiv \zeta_i^*(x,z)\zeta_j(x,z)$, as obtained from the discrete TB calculation. Here, $V(x,z)$ and $\tilde{\rho}^{(1)}(k_x, k_z)$ are obtained using an FFT routine. The full Coulomb integral then has the form $e\int dxdzV(x,z)\rho^{(2)}(x,z)$, which we perform as a discrete summation in real space. Our FCI computational strategy is summarized in more detail in Sec. A.1, while the details of the FFT-based integration method are described in Sec. A.2.

2.3 Results

In this section, we present our results for two-electron wavefunctions and ST splittings. We first provide an overview of the physics of two-electron wavefunctions in a Si quantum dot, followed by a more focused discussion of behavior observed as a function of confinement, for both circular and elliptical dots, and for dots with different disorder profiles. Geometries without interfacial disorder (i.e., without VOC) are easier to understand, and they provide a baseline for interpreting the more realistic, yet complicated, behaviors observed when VOC is present.

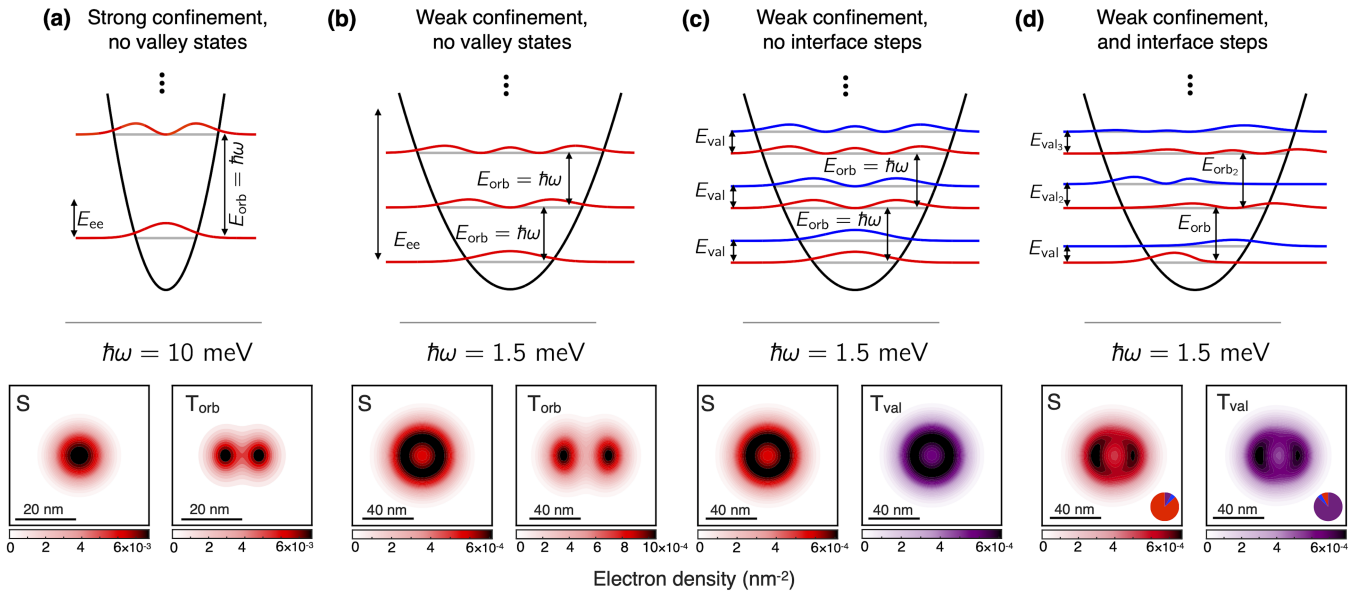

Figure 2.2: Summary of main results. Top row shows schematic single-electron wavefunctions. New physics ingredients, indicated by labels, are introduced into the calculations, one by one. The relations between different energy scales are also indicated: (a) $E_{ee} \ll E_{orb}$ (no valleys); (b) $E_{orb} \ll E_{ee}$ (no valleys); (c) $E_{val} \lesssim E_{orb} \ll E_{ee}$ (no interface steps); (d) $E_{val} \lesssim E_{orb} \ll E_{ee}$ (dot centered at an interface step). Color coding: orbital excitations (red), valley excitations (blue). Second row shows two-electron densities, obtained from FCI calculations. Confinement energies are specified ($\hbar\omega$), and the vertical electric field is (a) 40 MV/m, (b-d) 1.5 MV/m. Some distinctive features include (a) Wavefunctions dominated by low-energy configurations; (b) Wigner molecules shaped like (S) a doughnut, or (T_{orb}) a dumbbell; (c) S and T_{val} have identical shapes; (d) A single interface step breaks circular confinement symmetry. Color coding: same-valley eigenstates (red or blue), opposite-valley eigenstates (red + blue = purple). In (d), the broken valley symmetry induced by interfacial disorder causes orbital and valley states to hybridize, with the weights of same-valley and opposite-valley configuration indicated in the pie charts.

2.3.1 Overview of the physics

Here, we provide an overview of the physics of two-electron dots, including the effects of e-e interactions and interfacial disorder. We begin with the simplest case of weak e-e interactions, with no valleys and no disorder. (Note that, since the relative strength of e-e interactions is governed by $E_{\rm ee}/E_{\rm orb}$, the weakly interacting regime may also be viewed as the strongly confined regime; we will use this terminology interchangeably.) We then add each of these ingredients to our calculations, one at a time, to achieve a realistic description of the two-electron system. A schematic summary is presented in Fig. 2.2.

A system with weak e-e interactions, no valleys, and no disorder is easy to describe. Such situations can arise when the valley and orbital splittings are both much larger than other experimental energy scales. In the noninteracting limit, the two-electron wavefunctions are well-known from quantum mechanics textbooks, and are equivalent to low-energy configurations: the ground state is a spin singlet with spatial configuration given by $\phi_0(\mathbf{r}_1)\phi_0(\mathbf{r}_2)$, and the low-energy spin triplet has the spatial configuration $[\phi_0(\mathbf{r}_1)\phi_1(\mathbf{r}_2)-\phi_1(\mathbf{r}_1)\phi_0(\mathbf{r}_2)]/\sqrt{2}$. For the noninteracting case, the ST energy splitting is therefore given by $E_{\rm ST} = E_{\rm orb} = E_1 - E_0$. In Fig. 2.2(a), we show (schematically) the low-energy single-electron basis states, $\phi_0, \phi_1, \ldots,$ and the corresponding probability densities of the two-electron singlet and triplet states. For the triplet, we note that ϕ_1 is doubly degenerate (e.g., p_x vs. p_y), leading to degenerate triplets, of which we have only shown one.

We now include strong e-e interactions, with $E_{\rm ee} \gg E_{\rm orb}$, but still no valleys. Such a situation can arise when the dot is very large. In this regime, the energy cost for adding

new configurations to the two-electron wavefunctions is low compared with the potential benefits of using these configurations to reduce $E_{\rm ee}$. This leads to the formation of Wigner molecules, as shown in Fig. 2.2(b) for the low-energy singlet and triplet. For the singlet case, we note that the circular symmetry of the confinement potential is also conferred upon the two-electron wavefunction, yielding a Wigner molecule shaped like a doughnut. In general, the configurations that make up singlet wavefunctions have very different probability distributions than those of triplet wavefunctions, beginning already with the lowest-energy configurations, as described above. However in the strongly interacting limit, when a very large number of configurations contribute to each solution, the singlet and triplet wavefunctions grow more similar in appearance and in energy. This is because minimizing $E_{\rm ee}$ is the driving force for both the singlet and triplet calculations, and when many degrees of freedom are available for doing this, the resulting charge distributions take the same shape. Consequently, $E_{\rm ST}$ is strongly suppressed in the weakly confined regime, and ultimately approaches zero.

Next, we add valleys, but not interfacial disorder. For definiteness, we assume that $E_{\rm val} < E_{\rm orb}$, which is typical for most experiments. As seen in Fig. 2.2(c), each orbital state now splits into a pair of states (red and blue) with the same wavefunction envelope. The envelopes are modulated by fast valley oscillations (not shown), which are 90 degrees out of phase, yielding appropriately orthogonalized wavefunctions [36]. Due to the lack of interfacial disorder, the valley degree of freedom remains a good quantum number. Thus for strongly interacting electrons, the two-electron wavefunctions are formed of many configurations that

must all have the same valley character: either two electrons in the same valley state, or two electrons with opposite valley states. In particular, the ground-state singlet is formed of same-valley configurations. However, there are now two types of low-energy triplets: The first is formed of same-valley configurations, which we refer to as an orbital triplet, T_{orb}; The second is formed of opposite-valley configurations, which we refer to as a valley triplet, T_{val}. In the following sections, we analyze the ST splittings obtained for these two triplet states, defined as $E_{ST_{orb}}$ and $E_{ST_{val}}$.

Generally, the S and T_{orb} states have the same shape and behavior as the S and T states described above, for the case where no valleys were considered. However, T_{val} behaves differently. To understand this, we first note that 'valley' is a good quantum number for single-electron wavefunctions. This symmetry also extends to two-electron solutions, except that the Coulomb interaction term, H_{int}, breaks the symmetry very slightly. In the following section, and in Sec. A.3, we clarify the weak effects of this symmetry breaking. However, for the present purposes, we simply note that there is an approximate symmetry ensuring that T_{val} has the same configuration expansion as S, except with each spatially symmetric configuration replaced by a spatially antisymmetric configuration, with one of the lower valley states replaced by an excited valley state. This (approximate) symmetry is apparent when we compare the S and T_{val} wavefunctions in Fig. 2.2(c). Here, since the S wavefunction is formed exclusively of same-valley configurations (its probability density is colored red). The T_{val} probability density is formed of opposite-valley configurations (colored red + blue = purple). However, the shapes of the probability distributions appear identical. In addition to their

nearly identical shapes, the wavefunction energies are nearly identical, with $E_{\mathrm{ST}_{\mathrm{val}}} \approx E_{\mathrm{val}}$. This intriguing and important result will be explored in detail, below.

Finally, we consider the most physically relevant scenario, which includes disorder at the quantum well interface, which induces VOC and breaks the valley symmetry. As a result of VOC, the orbital and valley characters of the single-electron basis states hybridize, yielding pairs of valley states with dissimilar envelopes. This behavior is depicted in Fig. 2.2(d). (Note that the single-electron envelopes in the figure are merely schematics, which we have exaggerated for visual clarity.) The phases of the fast valley oscillations (not shown) are also affected by VOC, and vary from orbital to orbital. Despite the VOC, we note that it is usually possible to identify valley-like or orbital-like excitations in our TB wavefunctions, particularly when E_{val} is well separated from E_{orb}. In the remainder of this chapter, we therefore refer to them simply as valley or orbital states, when it makes sense to do so.

The broken valley symmetry extends to the two-electron states shown in Fig. 2.2(d), since the configurations are no longer strictly same-valley or opposite-valley. The presence of interfacial steps also breaks the circular symmetry of the confinement potential, so the probability densities take a shape intermediate between a doughnut and a dumbbell. The color of the probability density indicates that the S wavefunction is mainly formed of same-valley configurations (red with a blue tinge). Similarly, the $\mathrm{T}_{\mathrm{val}}$ probability density is formed mainly of opposite-valley configurations (purple with a red tinge). The actual same-valley (red) vs. opposite-valley (purple) configuration weights are specified in the pie charts shown as insets; in all the other panels, the colors are pure-red or pure-purple.

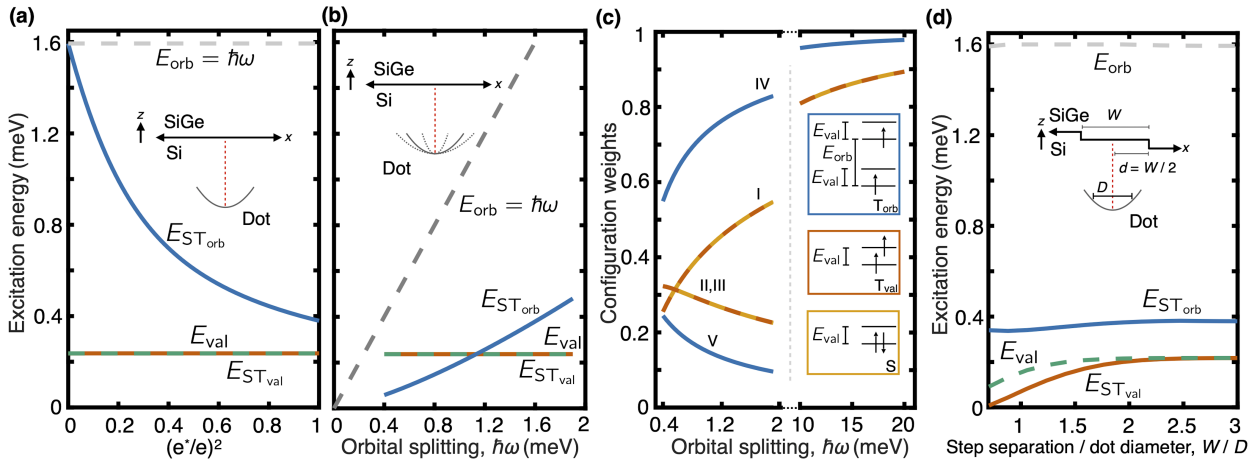

Figure 2.3: Effects of e-e interactions and VOC in silicon quantum dots. In (a), (b), and (d), we compare the single-electron valley splitting (cyan-dashed) and orbital splitting (gray-dashed) to the two-electron orbital (blue) and valley (red) singlet-triplet splittings, for a circular quantum dot. In (a), (b), and (c), there is no step disorder at the quantum well interface, and the e-e interactions are controlled by (a) the artificially modified Coulomb interaction strength $(e^*/e)^2$, or (b),(c) the orbital confinement strength $\hbar\omega$. In both cases, $E_{\mathrm{ST}_{\mathrm{orb}}}$ is suppressed well below its noninteracting value E_{orb}, as consistent with strongly interacting electrons, while $E_{\mathrm{ST}_{\mathrm{val}}} \approx E_{\mathrm{val}}$ is essentially unaffected by e-e interactions. (a) $E_{\mathrm{orb}} = \hbar\omega = 1.6$ meV. (b) $e^* = e$. Here, the lowest triplet state switches from $\mathrm{T}_{\mathrm{orb}}$ (low $\hbar\omega$), whose energy depends strongly on the confinement, to $\mathrm{T}_{\mathrm{val}}$ (high $\hbar\omega$), whose energy is nearly the same as S. (c) Weights of the lowest configurations, I to V (Table 2.2), for the S, $\mathrm{T}_{\mathrm{orb}}$, and $\mathrm{T}_{\mathrm{val}}$ results shown in (b). The weights of S and $\mathrm{T}_{\mathrm{val}}$ coincide, as consistent with $E_{\mathrm{ST}_{\mathrm{val}}} \approx$ const.. The wavefunctions only converge to their lowest configurations, depicted in the insets, for very strong confinement, indicating that the electrons are strongly interacting in the normal operating regime. (d) Excitation energies for a dot with VOC, induced by a tilted interface. Here, $E_{\mathrm{orb}} = \hbar\omega = 1.6$ meV corresponds to a dot of diameter $D = 2\sqrt{\hbar/m^*\omega} = 31.7$ nm, centered halfway between two steps ($d = W/2$). $E_{\mathrm{ST}_{\mathrm{val}}}$ is largest when the steps are very wide. For all calculations, the quantum well width is 10 nm, the barrier height is 150 meV, the dot is circular, and the vertical electric field is 1.5 MV/m, except on the right-hand side of (c), where the electric field is increased to 10 MV/m, to avoid filling higher subbands.

Finally, we note that ST splittings for dots with VOC will be discussed in later sections. However, we note that, since the approximate valley symmetry protecting $E_{\mathrm{ST_{val}}}$ is broken by the interfacial disorder, it is no surprise that $E_{\mathrm{ST_{orb}}}$ and $E_{\mathrm{ST_{val}}}$ are now both affected by e-e interactions.

2.3.2 Characterizing e-e interactions

In this section, we provide an in-depth analysis of the effects of e-e interactions. To begin, we return to the case of no interfacial disorder, and therefore, no VOC.

We first recall that the ratio $E_{\mathrm{Coul}}/E_{\mathrm{orb}}$ characterizes the strength of e-e interactions. However, the experimental tuning knob for the confinement energy, $\hbar\omega$, affects both E_{orb} and E_{Coul}. We can disentangle these parameters, theoretically, by holding $\hbar\omega$ fixed while tuning the effective charge used in the calculations, e^*. In Fig. 2.3(a), we plot several excitation energies as a function of the effective Coulomb interaction strength, $(e^*/e)^2$, for typical quantum dot parameters, in the absence of interfacial disorder. When $e^* = 0$, we observe results consistent with the noninteracting limit, described above, for which $E_{\mathrm{ST_{orb}}} = E_{\mathrm{orb}}$. When $e^* > 0$, $E_{\mathrm{ST_{orb}}}$ is quickly suppressed, which can be understood by considering the lowest-energy configurations for S, $\mathrm{T_{val}}$, and $\mathrm{T_{orb}}$, as depicted in the insets of Fig. 2.3(c). Since both electrons occupy the same orbital for S, and since this is the smallest orbital, the Coulomb energy is greater for S than it is for $\mathrm{T_{orb}}$. Therefore, as $(e^*/e)^2$ rises, the energy spitting $E_{\mathrm{ST_{orb}}}$ drops. The trend continues as the interaction strength grows, and many configurations begin to contribute to the wavefunctions. The fact that $E_{\mathrm{ST_{orb}}}$ reaches

a value for which $E_{\mathrm{ST}_{\mathrm{orb}}} \ll E_{\mathrm{orb}}$ at full interaction strength, $e^* = e$, indicates that the electrons are strongly interacting.

Turning to $\mathrm{T}_{\mathrm{val}}$, we see that $E_{\mathrm{ST}_{\mathrm{val}}} = E_{\mathrm{val}}$ in the noninteracting limit, $e^* = 0$, as expected. However, in stark contrast with the behavior of $E_{\mathrm{ST}_{\mathrm{orb}}}$, we find that $E_{\mathrm{ST}_{\mathrm{val}}} \approx E_{\mathrm{val}}$ over the whole range of coupling strengths. As discussed in the previous section, this remarkable behavior can be attributed to the valley symmetry present in the absence of VOC, and persists (approximately), even when the interactions are strong.

The nature of the valley symmetry can be understood from the Coulomb matrix elements giving rise to the weak symmetry breaking. Full details of this discussion are presented in Sec. A.3. We summarize those findings here by considering the single-electron spatial wavefunctions $\phi_\alpha(\mathbf{r})$ and $\phi_\alpha{}'(\mathbf{r})$, where $\phi_\alpha{}'(\mathbf{r})$ refers to the valley-excited version of the $\phi_\alpha(\mathbf{r})$ orbital. To a good approximation, $\phi_\alpha(\mathbf{r})$ and $\phi_\alpha{}'(\mathbf{r})$ have the same envelopes, but their fast valley oscillations differ in phase by 90 degrees [36]. Because of these fast oscillations, we would always expect the Coulomb integral,

$$\int d\mathbf{r}_1 \phi_\alpha(\mathbf{r}_1) \phi^{*\prime}_\beta(\mathbf{r}_1) V(\mathbf{r}_1, \mathbf{r}_2) \approx 0, \tag{2.9}$$

to vanish, for any α or β, whenever $V(\mathbf{r}_1, \mathbf{r}_2)$ is a slowly varying function. However, $V(\mathbf{r}_1, \mathbf{r}_2)$ is the Coulomb interaction, and is therefore singular when $\mathbf{r}_1 = \mathbf{r}_2$, yielding matrix elements that are nonvanishing. Consequently, the valley symmetry is lifted by Coulomb interactions. However, the resulting matrix elements are orders of magnitude smaller than unprotected

matrix elements. A second type of integral plays a role in ensuring that $E_{\mathrm{ST_{val}}} \approx E_{\mathrm{val}}$:

$$\int d\mathbf{r}_1 \phi_\alpha(\mathbf{r}_1)\phi_\beta^*(\mathbf{r}_1)V(\mathbf{r}_1,\mathbf{r}_2) \approx \int d\mathbf{r}_1 \phi_\alpha{}'(\mathbf{r}_1)\phi_\beta^{*\prime}(\mathbf{r}_1)V(\mathbf{r}_1,\mathbf{r}_2). \tag{2.10}$$

In this case, the approximate equality occurs because $\phi_\alpha(\mathbf{r})$ and $\phi_\alpha{}'(\mathbf{r})$ have nearly identical envelopes [72].

To further characterize e-e interactions, we plot excitation energies as a function of the orbital splitting in Fig. 2.3(b), and we plot the corresponding configuration weights ($|c_\alpha^{\mathrm{ST}}|^2$) in Fig. 2.3(c), as defined in Eq. (2.7). Again we observe the remarkable difference in behaviors of $E_{\mathrm{ST_{orb}}}$ and $E_{\mathrm{ST_{val}}}$. Here, we also observe a crossing between the triplet states, which plays an important role in experiments [82]. Specifically, for large quantum dots (small $\hbar\omega$), the excitation energy is a strong function of $\hbar\omega$, while for small quantum dots (large $\hbar\omega$) it is not. We define the minimum excitation energy as $E_{\mathrm{ST}} = \min(E_{\mathrm{ST_{val}}}, E_{\mathrm{ST_{orb}}})$.

In Fig. 2.3(c), we plot the weights of the dominant configurations for S, $\mathrm{T_{orb}}$, and $\mathrm{T_{val}}$. The spatial components of these configurations are defined in Table 2.2, with the lowest-energy configurations illustrated in the insets of the figure. (In the large-$\hbar\omega$ portion of the figure, we note that it was necessary to apply a large electric field, to avoid populating higher subbands in the quantum well.) Here, the valley symmetry causes the S and $\mathrm{T_{val}}$ configuration weights to overlap. There is a further degeneracy of levels II and III due to the circular symmetry of the confinement potential. In the limit of strong confinement (i.e., weak interactions) the two-electron wavefunctions are well approximated as single configurations, with the weights of all other configurations strongly reduced. It is important to note, however,

Table 2.2: Lowest-energy configurations comprising S, T_{val}, and T_{orb}. The notation $(n_x, n_y; n_{\bar{x}}, n_{\bar{y}})$ denotes properly normalized and symmetrized (or anti-symmetrized) spatial wavefunctions, formed as products of the single-electron states $\phi_{n_x,n_y}(1)$ and $\phi_{n_{\bar{x}},n_{\bar{y}}}(2)$. Here, n_x (n_y) denotes orbital quantum numbers for harmonic confinement along $\hat{x}$ ($\hat{y}$), and the primed notation indicates an excited valley state. Configurations I (S and T_{val}) and IV (T_{orb}) are depicted in the insets of Fig. 2.3(c).

	S	T_{val}	T_{orb}
I	$(0,0;0,0)$	$(0,0;0',0)$	-
II	$((1,0;1,0)+(0,1;0,1))/\sqrt{2}$	$((1,0;1',0)-(0,1;0',1))/\sqrt{2}$	-
III	$((0,0;2,0)+(0,0;0,2))/\sqrt{2}$	$((0,0;2',0)+(0,0;0',2)-(0',0;2,0)-(0',0;0,2))/2$	-
IV	-	-	$(0,0;1,0)$
V	-	-	$(1,0;2,0)$

that a 90% convergence of the weights is only achieved for $\hbar\omega > 20$ meV. For weaker confinements, we find that $E_{\mathrm{ST}_{\mathrm{orb}}} \ll E_{\mathrm{orb}}$. This $\hbar\omega = 20$ meV confinement level is much larger than typical dots [46, 104, 90], including MOS dots [105]. Moreover, the valley splittings in typical dots are also much lower than 20 meV. Taken together, these results emphasize the importance of both strong e-e interactions and valley splitting for all Si devices, and particularly for Si/SiGe quantum wells.

2.3.3 Characterizing VOC

In this section we explore the effects of single-atom steps at the quantum well interface, and the resulting VOC, for one and two-electron wavefunctions.

Isolated step

Valley splitting is determined by the valley phase at the quantum well interface [36]. Since that phase differs by $\sim \pi$ on neighboring atomic layers, a single-atom step at the interface can cause significant interference effects that suppress the valley splitting and generate VOC [37]. The presence of VOC hybridizes valley states in different orbitals; so the mixing fraction, defined as follows, provides a direct measurement of VOC in single-electron wavefunctions:

$$M_0 = \sum_{m_{x,z}=1,1',2,2',\ldots} \left| \left\langle \zeta_0 \middle| \zeta_{m_{x,z}}^{(\mathrm{flat})} \right\rangle \right|^2. \tag{2.11}$$

Here, $\zeta_0(x,z)$ is the ground state TB wavefunction in the presence of an atomic step, $\zeta_{m_{x,z}}^{(\mathrm{flat})}(x,z)$ are TB wavefunctions computed in the absence of steps, and the sum is taken over

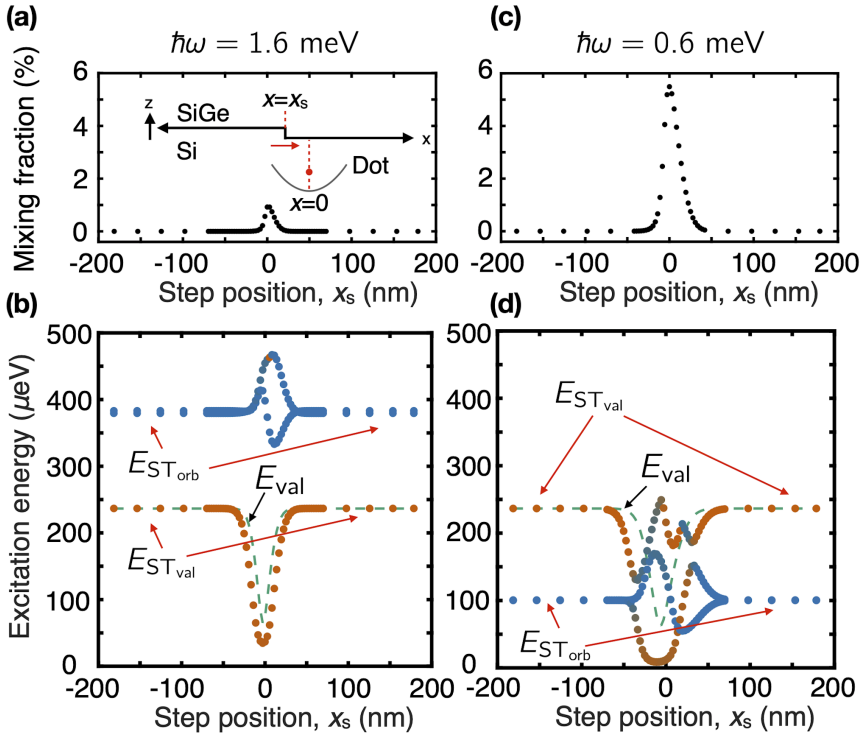

Figure 2.4: Effects of a single-atom step on valley splitting and VOC in one- and two-electron wavefunctions. (a) and (b) correspond to a small dot. (c) and (d) correspond to a large dot. In all cases, the quantum well is 10 nm thick and the vertical electric field is 1.5 MV/m. (a),(b) Mixing fractions, as defined in Eq. (2.11), plotted as a function of the step position, as depicted in the inset. A large mixing fraction indicates strong VOC in single-electron dots. (c),(d) Energy excitations as a function of the step position. Dashed cyan lines show the valley splitting of the lowest orbital level. Blue circles correspond to $E_{\mathrm{ST}_{\mathrm{orb}}}$ and red circles correspond to $E_{\mathrm{ST}_{\mathrm{val}}}$, where the colors reflect the total weight of same-valley configurations vs. opposite-valley configurations. Here we plot two $\mathrm{T}_{\mathrm{orb}}$ energy levels, which are degenerate in the $|x_s| \gg 0$ regime. The combination of VOC and e-e interactions suppresses $E_{\mathrm{ST}_{\mathrm{val}}} < E_{\mathrm{val}}$, but has a mixed effect on $E_{\mathrm{ST}_{\mathrm{orb}}}$. In (d), the triplet states anticross, causing the orbital vs. valley characters to switch.

all excited orbital states. (Note that VOC only occurs in the x-z sector of the wavefunctions, due to the separation of variables.)

We expect to observe larger VOC effects when a dot is closer to a step. In Figs. 2.4(a) and 2.4(c), we plot the mixing fraction as a function of the step coordinate, x_s (see inset for explanation), for two different dot sizes. M_0 is clearly peaked for small $|x_s|$, and it is more strongly peaked for large dots because the energy splittings are smaller. In Figs. 2.4(b) and 2.4(d), we also see that M_0 is strongly correlated with the suppression of the valley splitting (dashed curves).

The effects of a step on two-electron excitation energies are also shown in Figs. 2.4(b) and 2.4(d). Here, red circles correspond to $E_{\mathrm{ST}_{\mathrm{val}}}$ and blue circles correspond to the two $E_{\mathrm{ST}_{\mathrm{orb}}}$ excitations, which are degenerate in the asymptotic regime, $|x_s| \gg 0$. In the first case, the dot is small, so $E_{\mathrm{orb}} > E_{\mathrm{val}}$ and $E_{\mathrm{ST}_{\mathrm{orb}}} > E_{\mathrm{ST}_{\mathrm{val}}}$ in the asymptotic regime. In the region near $x_s \approx 0$, $E_{\mathrm{ST}_{\mathrm{val}}}$ deviates from E_{val} because VOC breaks the approximate valley symmetry that previously protected $E_{\mathrm{ST}_{\mathrm{val}}}$. Moreover, VOC now allows e-e interactions to have an effect on $E_{\mathrm{ST}_{\mathrm{val}}}$. We therefore find that $E_{\mathrm{ST}_{\mathrm{val}}} < E_{\mathrm{val}}$, for the same reasons that $E_{\mathrm{ST}_{\mathrm{orb}}} < E_{\mathrm{orb}}$ in the presence of e-e interactions. On the other hand, VOC has a more mixed effect on $E_{\mathrm{ST}_{\mathrm{orb}}}$, whose behavior is nonmonotonic near $x_s \approx 0$. For the larger dot shown in Fig. 2.4(d), $E_{\mathrm{orb}} < E_{\mathrm{val}}$ and $E_{\mathrm{ST}_{\mathrm{orb}}} < E_{\mathrm{ST}_{\mathrm{val}}}$ in the asymptotic regime, $|x_s| \gg 0$. In this case, the $\mathrm{T}_{\mathrm{orb}}$ and $\mathrm{T}_{\mathrm{val}}$ levels anticross, and we find that their orbital and valley characters switch at the anticrossing. Since e-e interactions are very strong for a large dot, $E_{\mathrm{ST}_{\mathrm{val}}}$ is suppressed very strongly below E_{val}. In all cases, we find that E_{ST} is strongly suppressed near a step.

Tilted interface

Another typical form of interface disorder occurs when the interface is tilted slightly away from the crystallographic axis; this can occur, for example, when the heterostructure is grown on a slightly miscut substrate. Here, we model such tilt by introducing uniformly distributed atomic steps at the interface. As for the case of a single step, the dot-step separation, W, plays an important role in determining the VOC.

In the present case, the dot may overlap with several steps, so dot diameter $D = 2\sqrt{\hbar/m_t\omega}$ (depicted in the inset of Fig. 2.3(d)) also plays a role in determining the VOC. More specifically, we can expect the ratio W/D to have a strong effect on both the single-electron valley splitting and the two-electron splitting $E_{\mathrm{ST}_{\mathrm{val}}}$. We explore this effect in Fig. 2.3(d) for the case where $d = W/2$; the other system parameters are the same as Fig. 2.3(a), with $e^* = e$. When $W \gg D$, we recover the excitation energies of Fig. 2.3(a). When $W \lesssim D$, the valley splitting is suppressed and would eventually go to zero for $W \to 0$. As in Fig. 2.4, we find that $E_{\mathrm{ST}_{\mathrm{val}}} < E_{\mathrm{val}}$, and that $E_{\mathrm{ST}_{\mathrm{orb}}}$ is only weakly affected by VOC.

We consider the full interplay between parameters W, D, and d. To begin, we solve for the dot energy excitations over all possible combinations of the following step parameters: $W/D \in \{3/5, 1, 2\}$, $d/W \in \{0, 1/4, 1/2\}$, and $\hbar\omega/\mathrm{meV} \in \{0.5, 1, 1.5, 1.9\}$. These results are reported in Sec. A.4. Here, we combine the results into a more cohesive form, based on the following observation: although the valley phases differ by $\sim \pi$ (i.e., nearly maximally) for interfacial steps separated by a single atom [36], steps separated by two atoms experience much smaller interference effects [37]. We can account for this even/odd behavior by defining

a parameter

$$Q = \left| 1 - 2 \sum_{i=\text{odd}} \int_{s_i} |\Psi_{\text{S}}(\mathbf{r}_1, \mathbf{r}_2)|^2 d\mathbf{r}_1 d\mathbf{r}_2 \right|, \tag{2.12}$$

where the integral represent a sum of contributions from every other step. For strongly localized dots, the corresponding values of Q are illustrated in Figs. 2.5(b) and 2.5(c). The function can be used to describe VOC for a single-step interface or a many-step interface; it can also be extended to one-electron systems or many-electron systems. In all cases, $Q = 0$ indicates strong VOC and $Q = 1$ indicates weak VOC.

In Fig. 2.5 we plot E_{ST} and E_{val} as a function of Q, obtaining results that collapse fairly well onto straight lines (note the large R values), with slopes that depend on $\hbar\omega$. The data collapse suggests that Eq. (2.12) indeed describes the effect of VOC on both one- and two-electron excitation energies. The collapse is poorer for E_{val} (cyan data), as expected, because E_{val} is a single-electron quantity, whereas Q (as defined here) and E_{ST} are two-electron quantities.

The two E_{ST} slopes in Fig. 2.5 correspond to the different excitation regimes in Fig. 2.3(b), which are dominated by T_{orb} for weak confinement $\hbar\omega < 1.1$ meV, or T_{val} for strong confinement $\hbar\omega > 1.1$ meV. (The dot with $\hbar\omega = 1$ meV sits at the crossover, and behaves similarly to the strongly confined dots.) For the case where T_{val} dominates, $E_{\text{ST}} \to 0$ when $Q \to 0$ because E_{val} is strongly suppressed near a step, similar to Fig. 2.4(c). For the case where T_{orb} dominates, $E_{\text{ST}} \to 0$ for the same reason, because the low-energy triplet takes on a strong valley-like character, similar to Fig. 2.4(d). The inset shows that E_{ST} goes to zero

much faster than E_{val}, as consistent with Fig. 2.3(d), due to the fact that the broken valley symmetry allows e-e interactions to strongly modify and suppress E_{ST}.

While the behavior embodied in Eq. (2.12) is useful as a guide, it does not fully describe the range of behaviors that are observed for strongly interacting electrons at disordered interfaces. For example, we observe some cases with low Q values but relatively high E_{ST} values, up to ~ 40 μeV (see left-hand inset). Such outliers are infrequent, however, and do not spoil the general correlations observed in Fig. 2.5; they also do not correspond to ST splittings that are large enough to be practical for quantum computing.

The main take-home message from this VOC analysis is that interfacial steps suppress E_{ST} and are therefore detrimental for quantum computing. To take a specific example, the qubit energy should be much larger than the thermal energy, for initialization or readout purposes. For electrons in Si/SiGe devices, this typically corresponds to 100 mK, for which $k_B T \approx 8.6$ μeV [106, 81, 107]. To be safe, qubits therefore require $E_{\mathrm{ST}} > 80$ μeV. To achieve such values, Fig. 2.5 suggests that we need $Q > 0.4$, indicating that at least 70% of an electron's probability should be centered on a single step (or on steps separated by two atomic layers). Moreover, the single-electron valley splitting should be on the order of 150 μeV.

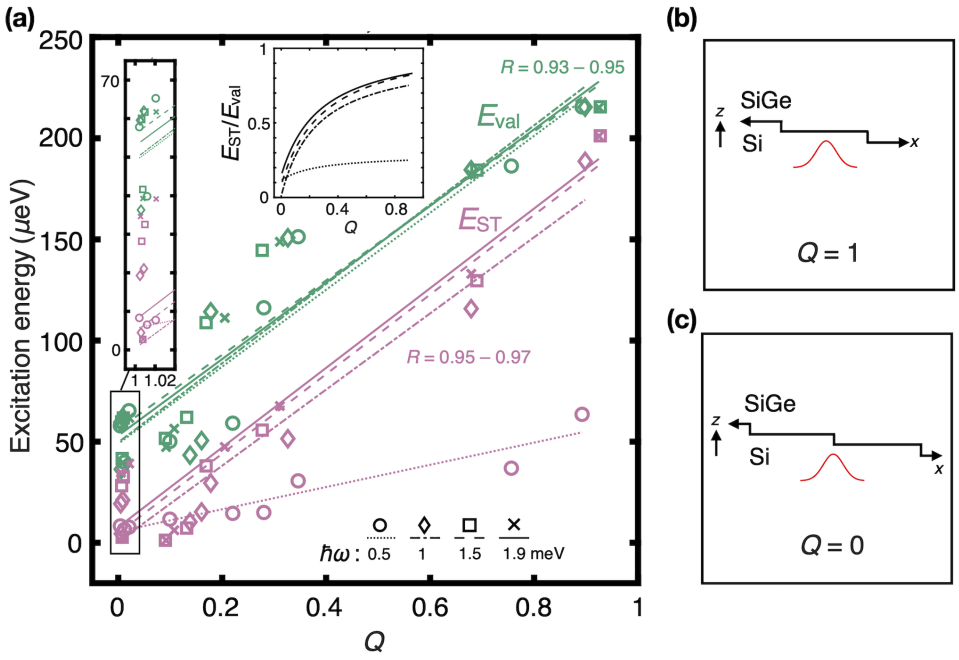

Figure 2.5: One and two-electron excitation energies for dots at a tilted interface, for a range step widths, dot diameters, and dot-step separations. [See inset of Fig. 2.3(d) for illustration.] (a) Results are combined using a single parameter Q, defined in Eq. (2.12), which describes the localization of an electron on one or more steps, as illustrated in (b) and (c). $E_{\rm ST}$ exhibits two distinct slopes as a function of Q, depending on its $\rm T_{orb}$ or $\rm T_{val}$ character, with $E_{\rm ST} \to 0$ for $Q \to 0$, corresponding to strong VOC. For all calculations, we assume a circular dot in a 10 nm wide quantum well, with an electric field of 1.5 MV/m and $\hbar\omega$ as indicated in the figure.

2.3.4 Elliptical dots

We now examine the effects of anisotropy in the 2D confinement potential on the singlet-triplet splittings. We find that changing the confinement potential from circular to elliptical affects our results quantitatively, but not qualitatively.

Once again, we begin with a flat interface, with no steps. We assume a parabolic confinement potential, as before, but we allow for separate confinement strengths, $\hbar\omega_x$ and $\hbar\omega_y$, along $\hat{x}$ and $\hat{y}$. In Fig. 2.6(a), we plot $E_{\rm ST}$ as a function of both $\hbar\omega_x$ and the anisotropy ratio, $\hbar\omega_y/\hbar\omega_x$. For any given $\hbar\omega_x$, $E_{\rm ST}$ is maximized when the confinement is isotropic, $\hbar\omega_y = \hbar\omega_x$. This is easy to understand because breaking the circular symmetry causes the degeneracy of the two-electron orbital triplets to be lifted, as shown in the lower panel of Fig. 2.6(a) (blue curves). The singlet-triplet splitting, $E_{\rm ST}$, is the energy difference between the lowest of these two curves and the singlet curve (yellow), and the peak in $E_{\rm ST}$ occurs where these triplet states cross in energy. For the confinement energy $\hbar\omega_x = 800$ μeV assumed in this plot, indicated by the dashed line in the top panel, $\mathrm{T_{orb}}$ is always the dominant excitation.

Next, we add a uniform tilt to the interface to induce VOC, with results shown in Fig. 2.6(b). As discussed in previous sections, the combination of VOC and strong e-e interactions suppresses the overall magnitude of $E_{\mathrm{ST_{val}}}$. The steps also break circular symmetry, as seen in Fig. 2.3(d), so there are two sources of anisotropy. The bottom panel of Fig. 2.6(b) shows the two-electron energy levels for $\hbar\omega_x = 1000$ μeV. Here, $\mathrm{T_{val}}$ (red curve) is suppressed below $\mathrm{T_{orb}}$ over most of the anisotropy range of interest, making $\mathrm{T_{val}}$ the

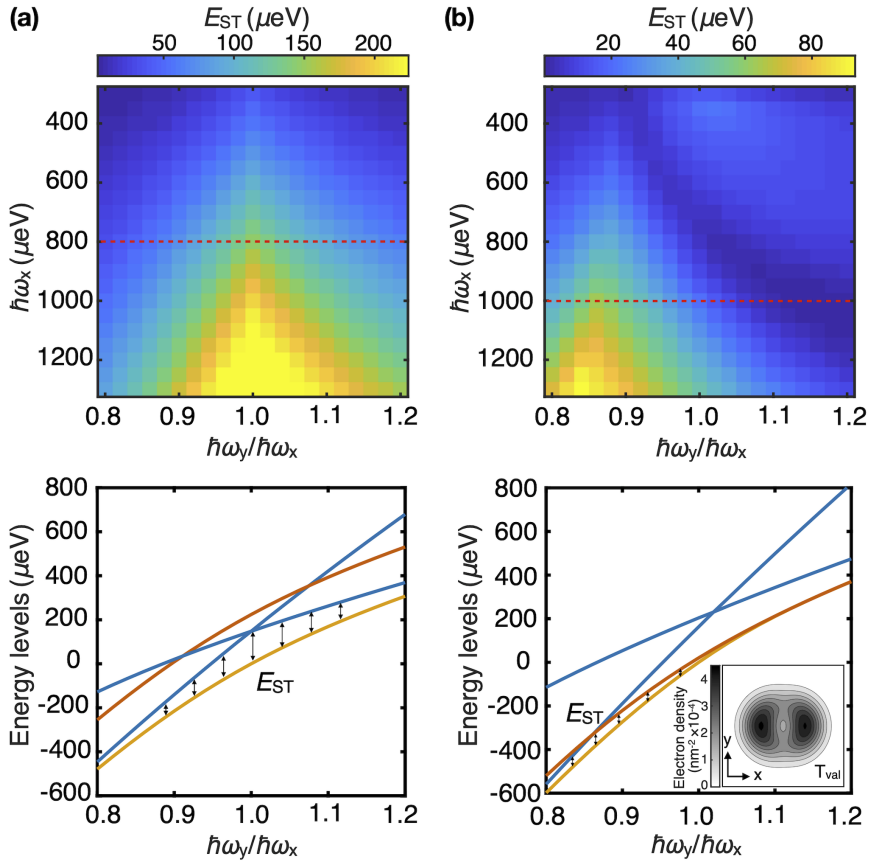

Figure 2.6: Effects of anisotropic confinement, with and without interface steps. All calculations assume 9.1 nm quantum wells, and a vertical electric field of 0.6 MV/m. Top panels show the dependence of $E_{\rm ST}$ on the 2D confinement parameters $\hbar\omega_x$ and $\hbar\omega_y/\hbar\omega_x$ for the case of (a) a flat interface, (b) a 0.23° tilted interface, with a step separation of $W \approx 34$ nm, and a dot-step separation of $d \approx 0.4W$. Bottom panels show the energies of the singlet (yellow), the valley triplet (red), and the two orbital triplets (blue), as a function of $\hbar\omega_y/\hbar\omega_x$, for the value of $\hbar\omega_x$ indicated by red-dashed lines in the top panels. (a) $E_{\rm ST}$ peaks at the symmetry point $\hbar\omega_y = \hbar\omega_x$. Away from this point, the circular symmetry is lifted, and the $T_{\rm orb}$ levels become non-degenerate. (b) $E_{\rm ST}$ peaks at $\hbar\omega_y/\hbar\omega_x < 1$, due to the combination of confinement- and step-induced anisotropy. $E_{\rm ST}$ is small compared to (a), due to the combination of VOC and e-e interactions. Inset: two-electron density of the low-energy triplet at point $\hbar\omega_x = \hbar\omega_y = 800$ μeV when $d = 0$, showing the effect of step-induced anisotropy.

dominant excitation. $E_{\mathrm{T}_{\mathrm{val}}}$ crosses the energy level of one of the orbital triplets at around $\hbar\omega_y/\hbar\omega_x = 0.85$, causing the peak in E_{ST}.

In Fig. 2.6(b), we see that the peak in E_{ST} shifts to the left, as a consequence of having two different anisotropy sources. To understand this, we first note that when $\hbar\omega_x < \hbar\omega_y$, and when there are no steps, the first orbitally excited single-electron state has a node in the $\hat{x}$ direction. The structure along $\hat{x}$ for single-electron wavefunctions also extends to two-electron wavefunctions. The key observation here is that elongation of the wavefunction along $\hat{x}$ occurs on the right-hand side of Fig. 2.6(a). Now, when we include a single step in the x-z plane, but remove all other anisotropy, our FCI calculations show that the emerging Wigner-molecule structure also occurs in the $\hat{x}$ direction, as shown in the inset of Fig. 2.6(b). Here, the key observation is that this behavior is similar to what we already found on the right-hand side of Fig. 2.6(a). Hence, the step acts like an effective, built-in softening of the x confinement, which results in the peak in Fig. 2.6(b) shifting to the left. In this case, we note again that selection rules prevent excitations from occurring along the $\hat{y}$ direction, for two-electron wavefunctions.

2.4 Summary and Conclusions

In this chapter we have studied the combined effects of strong electron-electron interactions and interface disorder in two-electron quantum dots in silicon heterostructures. Our calculations combine full configuration interaction and tight-binding methods to treat interaction effects and valley-orbit coupling nonperturbatively and consistently.

Electron-electron interactions become more important as the dot size increases. Our calculations show that for dots in Si/SiGe quantum wells, in the experimentally relevant confinement regime (with typical dot sizes of several tens of nanometers), electron-electron interactions are strong. For a smooth quantum well interface, without disorder, the valley degree of freedom does not couple to the orbital degree of freedom. Two-electron excitations therefore take the form of well-defined and qualitatively distinct valley triplets or orbital triplets. Interactions have a strong effect on the energy of these two-electron states, but for typical dot sizes, the singlet-to-valley-triplet excitation energy is very close to the single-electron valley-splitting energy, even when interactions modify the shape of the valley triplets substantially.

Atomic steps at the quantum well interface are known to suppress the valley splitting. They are the main source of valley-orbit coupling, which hybridizes the single-electron valley and orbital eigenstates, and allows strong electron-electron interactions to suppress the valley-triplet excitation energy, relative to the valley splitting. Steps also reduce the confinement symmetry in a dot, effectively reducing the confinement in the direction perpendicular to the steps. The step density, and the position of step(s) relative to the dot, both have a strong effect on the singlet-triplet splitting. Importantly, the observation of a large singlet-triplet splitting is a good indictor of a large valley splitting, and suggests that atomic steps (if present) do not have a strong effect on the dot.

Finally, we note that the results described here also pertain to qubits formed in MOS systems, such as Si/SiO_2 interfaces or Si finFETs [108, 109, 53, 54, 55, 110, 111]. However,

for these systems, the electric fields are typically higher than in SiGe/Si/SiGe quantum wells, which enhances the valley splitting. The confinement energies also tend to be much higher. As a result, electrons in MOS dots are less likely to be strongly interacting.

In conclusion, we have presented calculations showing that electron-electron interactions are significant in multi-electron Si/SiGe quantum dots. We have also shown that valley physics is nontrivial in these devices, particularly for strongly interacting electrons, with implications for the energy spectrum. Interfacial disorder adds an extra layer of complexity, as it couples the valley and orbital degrees of freedom. The current study provides key insights into the physics of multi-electron quantum dots in silicon, which is essential for the rational design and operation of qubits.

This work was supported in part by ARO through Award No. W911NF-17-1-0274 and the Vannevar Bush Faculty Fellowship program sponsored by the Basic Research Office of the Assistant Secretary of Defense for Research and Engineering and funded by the Office of Naval Research through Grant No. N00014-15-1-0029. The views and conclusions contained in this document are those of the authors and should not be interpreted as representing the official policies, either expressed or implied, of the U.S. Government. The U.S. Government is authorized to reproduce and distribute reprints for Government purposes notwithstanding any copyright notation herein. This research was performed using the compute resources and assistance of the UW-Madison Center For High Throughput Computing (CHTC) in the Department of Computer Sciences. The CHTC is supported by UW-Madison, the Advanced Computing Initiative, the Wisconsin Alumni Research Foundation, the Wisconsin

Institutes for Discovery, and the National Science Foundation, and is an active member of the Open Science Grid, which is supported by the National Science Foundation and the U.S. Department of Energy's Office of Science.

Chapter 3

Charge noise resilience of Si/SiGe singlet-triplet splitting: valleys and e-e interactions

This chapter is adapted from the manuscript "Charge noise resilience of Si/SiGe singlet-triplet splitting: valleys and e-e interactions" by H. Ekmel Ercan, Mark Friesen, and S. N. Coppersmith, which will be submitted for publication.

3.1 Introduction

Charge noise is a dominant source of decoherence in quantum dot (QD) qubits that limits qubit gate fidelities [112, 113, 114]. Approaches for suppressing the effects of charge noise include material and surface improvements [115, 116], using pulse sequences such as

dynamical decoupling that enable self-compensation of errors [117, 118], using strong driving together with special pulse shaping techniques [119], and encoding qubits in multiple QDs allowing the use of sweet spots, i.e. regions in control-parameter space that yield qubit energies resistant to environmental perturbations [120, 86, 26, 121, 122, 123, 124, 125, 81, 126].

Experiments have shown that qubits fabricated in QDs with multiple electrons can have particularly favorable properties [50, 127, 51, 52, 53, 54, 55]. Theoretical studies of GaAs dots have demonstrated that dots with multiple electrons can be more resilient to charge fluctuations [98, 128, 100]. However, investigating multi-electron wave functions in Si is fundamentally different than for GaAs because the electrons have both orbital and valley degrees of freedom. The orbital levels are determined by the electrostatic confinement potential, while the valley degrees of freedom arise from the X valleys of the conduction band, with the valley degeneracy lifted by the quantum well interface [36]. Exploring whether using multi-electron wave functions can suppress the susceptibility of silicon qubits to charge noise requires incorporating electron-electron (e-e) interactions as well as valley-orbit coupling (VOC) effects that depend on atomic-scale physics at the quantum well interface.

Here we investigate the effects of charge noise on two-electron singlet-triplet (ST) splitting in a single QD using theoretical techniques that capture valley and multi-electron physics, incorporating strong e-e interactions as well the atomic-scale effects of disorder at the Si/SiGe interface, in the regime in which the single-particle orbital splittings are larger than the valley splittings, as is typical for quantum dots in Si/SiGe heterostructures used for qubit

experiments [129, 130, 131, 104, 90, 46, 82]. We show that a confinement-controlled characteristic change in the wave functions of the first-excited state can result in a dramatic change in the sensitivity of ST splitting to a nearby charge trap (CT) for small changes in the confinement strength.

The large change in the susceptibility to charge noise arises because the charge density distribution of the lowest energy triplet state with valley character is very similar to that of the ground state and therefore the two states respond similarly to charge fluctuations, while the charge density of the lowest energy triplet state with orbital character differs significantly from that of the singlet ground state. Fig. 3.1 shows schematics of the in-plane electron densities of the ground state singlet, the valley triplet, and the orbital triplet states. Whether the lowest two-particle excited state has a valley or orbital character depends on the confinement strength, which can be characterized using the single-particle orbital energy splitting $\hbar\omega$. Electron-electron interactions also play important role because they substantially lower the energy of the orbital triplet relative to the the valley triplet. When the dot size is small enough, the valley triplet has lower energy than the orbital triplet, because $\hbar\omega$ is much larger than the single-particle valley splitting, and also because the parameter governing the scale of the e-e interactions relative to the orbital energy splitting is proportional to $1/\sqrt{\omega}$) and hence vanishes as $\omega \to \infty$. However, as we show below, the orbital triplet can have lower energy than the valley triplet at experimentally relevant dot confinements.

Our theoretical method combines a tight-binding (TB) calculation that enables the char-

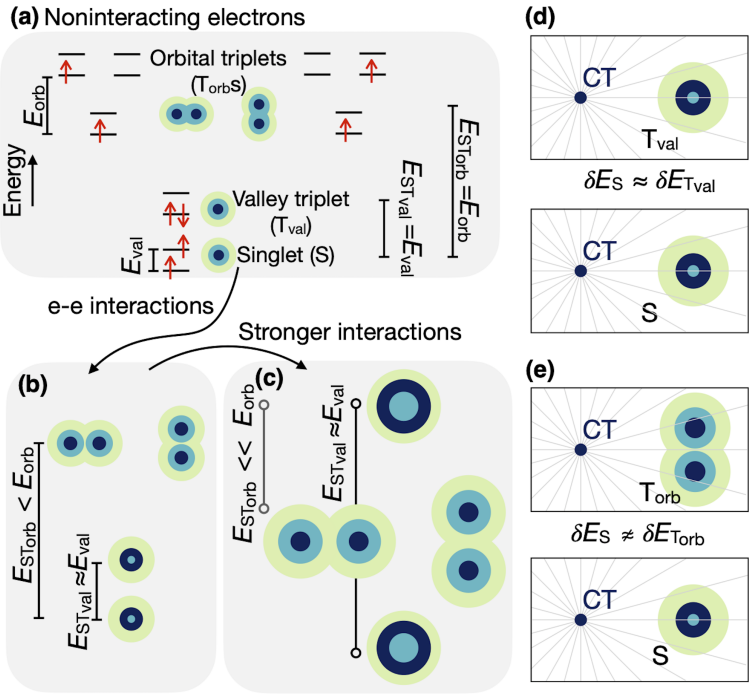

Figure 3.1: Effects of electron-electron interactions and the electric field of a charge trap (CT) on the singlet-triplet (ST) splitting E_{ST} in a doubly-occupied quantum dot in a Si/SiGe heterostructure. Electron densities are shown schematically with darker colors indicating higher density. (a) For non-interacting electrons, the two-particle valley ST splitting $E_{\mathrm{ST_{val}}}$ is equal to the single-particle valley splitting E_{val} and the two-particle orbital ST splitting $E_{\mathrm{ST_{orb}}}$is equal to the single-particle orbital splitting E_{orb}. Electron densities of S and $\mathrm{T_{val}}$ states are similar whereas the electron densities of S and $\mathrm{T_{orb}}$ states are not. Typically, as shown here, $E_{\mathrm{val}} < E_{\mathrm{orb}}$ and $E_{ST} = E_{\mathrm{ST_{val}}}$. (b) Electron-electron interactions suppress $E_{\mathrm{ST_{orb}}}$ whereas E_{val} is practically unaffected. (c) When the interactions are strong enough, $E_{\mathrm{ST_{orb}}}$ is smaller than $E_{\mathrm{ST_{val}}}$ and $E_{ST} = E_{\mathrm{ST_{orb}}}$. (d-e) Electron densities of the S, $\mathrm{T_{val}}$, and $\mathrm{T_{orb}}$ states in the electric field of a CT. (d) The change in $E_{\mathrm{ST_{val}}}$ due to a CT is relatively small, while (e) the change in $E_{\mathrm{ST_{orb}}}$ is relatively large.

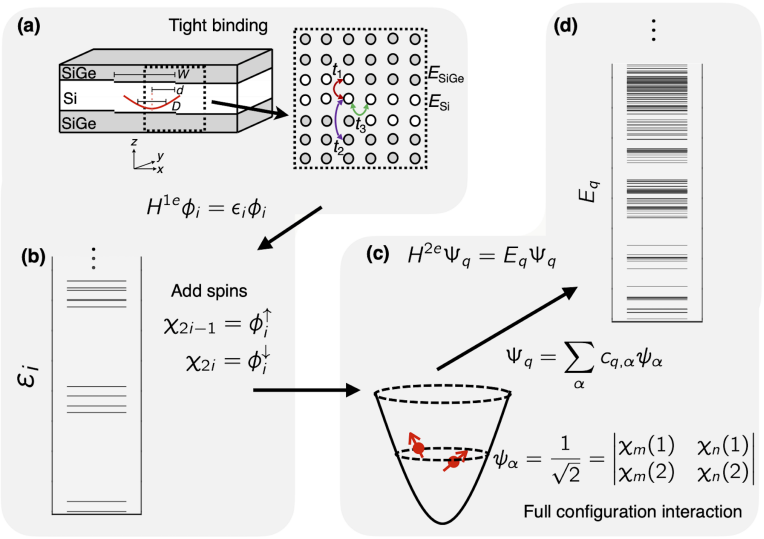

Figure 3.2: Overview of theoretical method for calculating properties of two electrons in a Si/SiGe quantum dot. Tight-binding (TB) methods that incorporate atomic-scale disorder that gives rise to valley-orbit coupling are combined with full-configuration interaction (FCI) methods to incorporate the effects of strong e-e interaction effects. (a) Schematic of the two-dimensional TB calculation. Out-of-plane hopping parameters t_1 and t_2 are chosen to reproduce the silicon valley minima location and curvature [88], while t_3 is the in-plane hopping parameter. On-site terms E_{Si} and E_{SiGe} determine the band offset between the Si layer and the SiGe layer, $E_{\mathrm{Si}} - E_{\mathrm{SiGe}} = 150$ meV, appropriate for 30% Ge. (b) Single-electron energies ε_i and wave functions ψ_i are obtained using TB. (c) FCI step: All possible Slater determinants Φ_α are generated using the truncated set of TB solutions χ_m with spin degrees of freedom added. The two-particle interacting Hamiltonian H_{2e} (Eq. 3.5) is diagonalized in this Slater basis, with enough single-particle energy eigenstates included to ensure convergence. (d) Two-electron energies E_q and wave functions Ψ_q are obtained.

acterization of the valley physics of Si, including valley-orbit coupling induced by disorder at the Si/SiGe interface, with a full configuration interaction (FCI) treatment of strong e-e interactions (see Fig. 3.2). In the TB calculation, shown schematically in Fig. 3.2(a), the Hamiltonian for the electrons in the 3D heterostructure is assumed to be separable in the $x-z$ plane and the y direction, corresponding to straight interface steps along y. This simplification allows the effects of interface disorder on the valley physics as a function of x to be incorporated while still enabling the variations in y to be treated analytically, enabling the calculation to reach full convergence on a practical time scale. In this framework, the single-electron Hamiltonian can be written as

$$H^{1e} = H_{\mathrm{K}} + H_{\mathrm{E}} + H_{\mathrm{QW}}. \tag{3.1}$$

Here, the kinetic energy is

$$H_{\mathrm{K}} = \frac{-\hbar^2}{2m_t}\frac{\partial^2}{\partial y^2} + \sum_{i,j=0,\pm1,\ldots} \left(t_1 \left|i,j+1\right\rangle \left\langle i,j\right| + t_2 \left|i,j+2\right\rangle \left\langle i,j\right| + t_3 \left|i+1,j\right\rangle \left\langle i,j\right| + \mathrm{h.c.}\right), \tag{3.2}$$

where the hopping parameters $t_1 = 0.68$ eV and $t_2 = 0.61$ eV in z are chosen to reproduce k-space location of the conduction band minima ($k_0 = \mp 0.82(2\pi/a)$, $a = 5.43$ Å is the bulk Si lattice constant [1]) and the longitudinal effective mass of silicon, $m_l = 0.916\ m_0$ for grid spacings of $\Delta z = a/4$ [88], while $t_3 = -0.026$ eV in x is chosen to yield the transversal effective mass of silicon, $m_t = 0.191\ m_0$, for the grid spacings of $\Delta x = 2.79$ nm

[1] In Si/SiGe heterostructures, Si is strained due to lattice mismatch. In this work, we use bulk Si parameters as modified parameters that take strain into account differ slightly from the bulk [36]

our calculations. Grid spacings in x can be much larger than spacing along z, as there are no fast oscillations in x. The quantum well potential is

$$H_{\mathrm{QW}} = \sum_{i,j=0,\pm1,\ldots} \left[E_0 + V_{\mathrm{QW}}\Theta_{i,j} - e(iF_x\Delta x + jF_z\Delta z) \right] |i,j\rangle \langle i,j| \,, \tag{3.3}$$

where $\Theta_{n,m}$ is a step function that takes the value 1 on a SiGe site and 0 on a Si site, $V_{\mathrm{QW}} = 150$ meV is the band offset between Si and SiGe, e is elementary charge, and $\boldsymbol{F}^{\mathrm{e}}$ is the electric field perpendicular to the interface due to the gate electrodes ($|\boldsymbol{F}^{\mathrm{e}}|$=0.6 MV/m). E_0 is a uniform on-site energy that shifts the energy minimum but does not effect the energy splittings that we are interested in. The interface disorder is implemented in the choice of $\Theta_{n,m}$. In this work, we considered interfacial tilts modeled with uniformly-distributed single atomic steps of height $a/4$. The electrostatic potential is modeled by harmonic oscillators:

$$H_{\mathrm{E}} = \frac{1}{2} m_t \omega_x^2 \sum_{i,j=0,\pm1,\ldots} (i\Delta x)^2 |i,j\rangle \langle i,j| + \frac{1}{2} m_t \omega_y^2 y^2, \tag{3.4}$$

As a first step we solve for $H^{1\mathrm{e}}\phi_i = \varepsilon_i \phi_i$, where $H^{1e} = H^{1e}_{\mathrm{x,z}} + H^{1\mathrm{e}}_{\mathrm{y}}$, and obtain the single-electron energy spectrum, for which a typical level structure is shown in Fig. 3.2(b).

The Hamiltonian for two electrons including Coulomb interactions is

$$H^{2\mathrm{e}} = H^{1\mathrm{e}}(\boldsymbol{r}_1) + H^{1\mathrm{e}}(\boldsymbol{r}_2) + \frac{e^2}{4\pi\epsilon_0\epsilon_r} \frac{1}{|\boldsymbol{r}_1 - \boldsymbol{r}_2|} \,, \tag{3.5}$$

where ϵ_0 is the permittivity of free space, and $\epsilon_r = 11.4$ is the dielectric constant of low-temperature Si [91]. Dielectric constant of SiGe is expected to be slightly higher but we

treat it the same as Si, as a small fraction of electrons penetrate into SiGe. We solve for the eigenvalues and eigenstates of $H^{2e}\Psi_q = E_q\Psi_q$ by using the FCI method [92], in which H^{2e} is diagonalized in a basis of Slater determinants generated from spin-orbitals χ_j, that are based on a truncated set of ψ_i, as shown in Fig. 3.2(c). Analytical integration of y degree of freedom in calculation of interaction terms allows reducing the numerical problem to two dimensions by replacing the $1/r$ potential with an effective potential (see Ch. 2).

3.2 Results

3.2.1 FCI simulations

When e-e interactions and valley-orbit coupling arising from interface steps are both absent, the two-electron ground state is a spin singlet (S) with both electrons occupying the ground single-electron level, and the valley ST splitting ($E_{\mathrm{ST_{val}}}$) is equal to the energy difference between the ground state and lowest valley-excited level. The in-plane charge densities of the S and $\mathrm{T_{val}}$ states are similar, so their energies are affected similarly by small changes in the electromagnetic environment, as indicated in Fig. 3.1(d). The orbital valley splitting $E_{\mathrm{ST_{orb}}}$ between S and the triplet states that have one of the electrons in an excited orbital level ($\mathrm{T_{orb}}$) is equal to the single-electron orbital splitting (E_{orb}). The in-plane charge densities of the S and $\mathrm{T_{orb}}$ states differ significantly, so changes to the electromagnetic environment affect them differently, giving rise to a stronger dependence of $\mathrm{T_{orb}}$ on charge

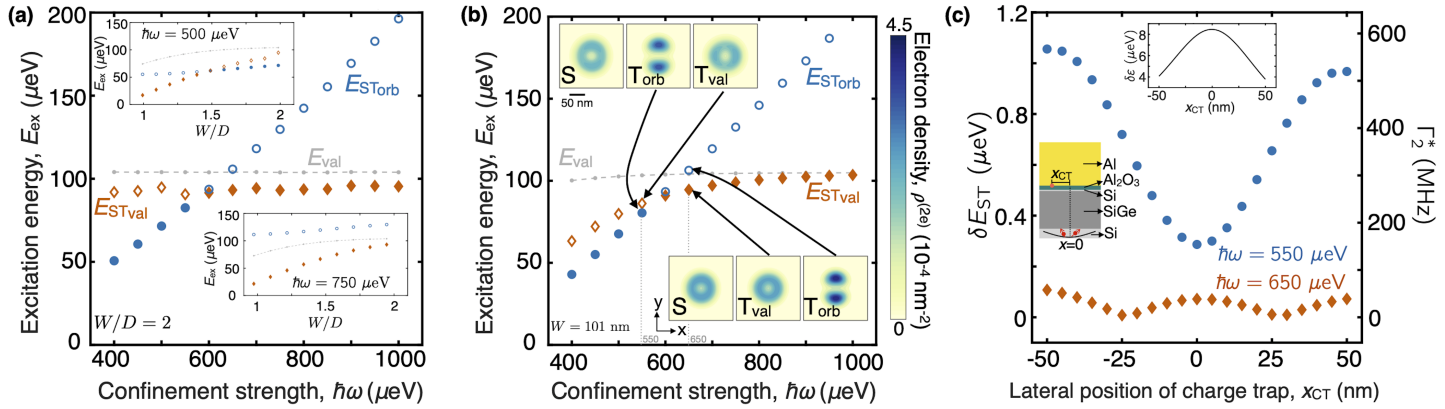

Figure 3.3: Singlet-triplet splitting and its shift due to a charge trap. (a) Valley and orbital singlet-triplet splittings $E_{\mathrm{ST_{val}}}$ and $E_{\mathrm{ST_{orb}}}$ versus confinement strength $\hbar\omega$. Main panel: when the valley-orbit coupling is weak (the uniformly tilted interface profile has the ratio of step width w to dot diameter D of $w/D = 2$, where $D = \sqrt{\hbar/m_t\omega}$, and the distance to the nearest step of $f = w/2$), increasing ω decreases the effective electron-electron (e-e) interaction strength and causes the orbital ST splitting $E_{\mathrm{ST_{orb}}}$ (blue) to increase strongly while having a minimal effect on the valley ST splitting $E_{\mathrm{ST_{val}}}$ (red), resulting in a crossover from $E_{\mathrm{ST_{orb}}} < E_{\mathrm{ST_{val}}}$ for small ω to $E_{\mathrm{ST_{val}}} < E_{\mathrm{ST_{orb}}}$ at large ω. This crossover occurs at an experimentally-relevant set of parameter values: $E_{\mathrm{orb}} = 600$ μeV, $E_{\mathrm{val}} = 104$ μeV, $E_{\mathrm{ST}} = 92$ μeV. Insets: $E_{\mathrm{ST_{val}}}$ and $E_{\mathrm{ST_{orb}}}$ at $\hbar\omega = 550$ and 650 μeV as the valley-orbit coupling is decreased by increasing w/D. Increasing the valley-orbit coupling by decreasing w/D decreases the valley ST splitting more than the orbital ST splitting. Solid symbols indicate the lower excitation energies that define the ST splitting. (b)Behavior of valley and orbital singlet-triplet splittings with distance between steps w fixed at $w = 100$ nm, corresponding to 0.08° interfacial tilt. The single-electron valley splitting E_{val} is also shown. The crossover between valley and orbital ST splittings as the confinement strength is increased is again observed, and E_{ST} varies much more strongly with ω when ω is small than when it is large. Insets: Electron densities of the singlet S, orbital triplet $\mathrm{T_{orb}}$, and valley triplet $\mathrm{T_{val}}$ states, at two different confinement strengths. (c) Dephasing rates Γ_2^* at $\hbar\omega = 0.55$ meV (blue) and $\hbar\omega = 0.65$ meV (red) points in (b), as a function of the lateral position of a charge trap. Γ_2^* is significantly lower when $\mathrm{T_{val}}$ is the first-excited state than when $\mathrm{T_{orb}}$ is the first-excited state. Insets: (Left) Schematics of dot and charge trap geometry. Charge trap is located inside Al_2O_3, 0.1 nm below Al gate layer. (Top) Shifts in the detuning ε, for a double dot geometry with dot separation of 200 nm in x direction, due to the occupied charge trap.

noise (Fig. 3.1(e)). These results imply that confinement strengths that are above a certain threshold result in ST splittings that are more resilient to charge noise.

We now consider dots with strong interactions but no valley-orbit coupling. As Fig. 3.1(b) indicates, strong electronic repulsion changes the charge densities of both the S and T_{val} states, but the charge densities of S and T_{val} remain similar to each other. Therefore, the ST splitting can be close to the single-particle excitation energy even when e-e interactions are strong, so long as the first-excited state of the system is T_{val}. However, e-e interactions strongly suppress the orbital splitting, so that the orbital triplet has lowest energy at substantially smaller dot diameters than in the absence of e-e interactions. This suppression, which can be seen as a crossover from the Fermi liquid to the Wigner molecule regime, has been discussed previously [56, 32, 34, 57, 33].

Now we discuss the results of calculations that include both strong e-e interactions and valley-orbit coupling (VOC) induced by steps at the Si/SiGe interface. VOC mixes the valley and orbital states and also lowers the single-electron valley splitting [37]. These calculations enable us to show quantitatively that step separations need be only slightly larger than the dot diameter for the valley ST splitting to be essentially independent of both dot diameter and of small changes in transverse electric fields. We focus on interface configurations and step locations in which the electron wave function is not directly over a step and the single-particle valley splitting is at least 100 μeV, which is necessary for the resulting singlet-triplet splitting to be large enough to suppress thermal excitations to excited levels at the electron temperatures in typical qubit experiments [132, 81, 107]. Our model of the interface has

uniformly spaced atomic steps; this simplification is unimportant because the dot typically extends over a very small number of steps. In these calculations, we use three parameters to define dot-interface relation: distance from the center of the dot to the nearest step (d), dot diameter ($D = 2\sqrt{\hbar/m_t\omega}$), and distance between two consecutive steps (w).

Fig. 3.3(a) shows $E_{\rm ST}$ (filled blue or red symbols) as a function of confinement strength $\hbar\omega$, when $d = w/2$ and w/D is held fixed at 2. For the parameter values chosen, $E_{\rm val} \approx 105$ μeV and $E_{\rm ST_{val}} \approx 90$ μeV/ The valley singlet-triplet splitting $E_{\rm ST_{val}}$ is nearly independent of $\hbar\omega$ on the plot, consistent with the intuition that the VOC effects are governed by w/D. For the parameters used, one finds that the lowest triplet state is $\rm T_{orb}$ when $\hbar\omega \lessapprox 600$ μeV. The value of $\hbar\omega$ at the crossover from valley-like triplet to orbital-like triplet is much larger than in the noninteracting case because e-e interactions strongly suppress the excitation energy $E_{\rm ST_{orb}}$ (blue) and the orbital energy splitting $\rm T_{orb}$. The insets of Fig. 3.3(a) show that lower w/D ratios for $f = w/2$ yield significant reduction in ST splittings, making it harder to achieve values over ~ 80 μeV needed for qubit applications. In Sec. B.1 we show that for when $f = 0$ and the center of the wave function is directly over the step, the singlet-triplet splitting is suppressed still further.

In experiments, the distance between steps in a quantum well interface is fixed in a given sample, so in Fig. 3.3(b) we show the results of calculations in which the the step separation is held fixed. In this situation, $E_{\rm ST_{val}}$ varies significantly with the confinement $\hbar\omega$ at smaller confinements (large w/D), but $E_{\rm ST_{val}}$ varies much less with $\hbar\omega$ when $\hbar\omega$ is larger.

The change in nature of the lowest energy two-particle triplet state from valley-like to

orbital-like excitation can have substantial effects on qubit coherence. For example, the logical basis states of the quantum dot hybrid qubit are the two lowest energy eigenstates in a double occupied quantum dot [27, 29], so a fluctuation in the singlet-triplet splitting of the doubly-occupied quantum dot leads directly to qubit dephasing. Here we focus on dephasing caused by the effects of charge noise that changes the electromagnetic environment, specifically on the effects of adding an additional charge from an impurity. The insets in Fig. 3.3(b) show the electron densities in the dot at confinement values $\hbar\omega = 550$ and 650 μeV, which bracket the transition at which the triplet state changes between valley and orbital excitation. Comparing these calculated wave functions to the schematic drawings of Fig. 3.1, one again sees that there is a the sharp contrast in the similarity of the electron densities of the S and T_{val} states, as opposed to S and T_{orb} states suggests that the variation in $E_{ST_{val}}$ induced by remote charge fluctuations should be smaller than the variation in $E_{ST_{orb}}$. Therefore, stronger confinements that favor T_{val} over T_{orb} as the first-excited state are expected to be advantageous yielding longer dephasing times for oscillations between the logical basis states.

3.2.2 Perturbation theory calculation of the shift in singlet-triplet splitting due to a charge trap

To quantify this effect, we estimate the shifts in ST splittings due to a charge trap to first-order in perturbation theory. Therefore, the shift in $E_{ST_{val}}$ due to the electrostatic potential V of an occupied charge trap is

$$\delta E_{\mathrm{ST_{val}}} \approx |\mathrm{e}| \times |\langle \mathrm{T_{val}}| V |\mathrm{T_{val}}\rangle - \langle \mathrm{S}| V |\mathrm{S}\rangle| \,. \tag{3.6}$$

Although we consider circular dots ($\omega_x = \omega_y$), that normally yield doubly-degenerate orbital triplets (as schematically shown in Fig. 3.1), the interfacial disorder breaks this degeneracy, allowing the use of nondegenerate perturbation theory for the shift in $E_{\mathrm{ST_{orb}}}$ as well:

$$\delta E_{\mathrm{ST_{orb}}} \approx |\mathrm{e}| \times |\langle \mathrm{T_{orb}}| V |\mathrm{T_{orb}}\rangle - \langle \mathrm{S}| V |\mathrm{S}\rangle| \,, \tag{3.7}$$

where $\mathrm{T_{orb}}$ denotes the low-energy orbital triplet shown in Fig. 3.2(b).

We consider a charge trap $\sim$ 50 nm above the dot, inside Al-oxide layer, as suggested by recent experiments [114]. As the charge trap is strongly screened by the metallic gate in this geometry, potetial due to its occupied state can be written as $V = \frac{1.13\mathrm{e}}{4\pi\epsilon_0\epsilon_r}\left(|\boldsymbol{R}-\boldsymbol{r}|^{-1} - |\boldsymbol{R}_{im}-\boldsymbol{r}|^{-1}\right)$, where $\boldsymbol{R}$ is the position of the trap and $\boldsymbol{R}_{im}$ is the position of its mirror image. The expression for V consists of the first two dominant terms in the method of images solution that takes different dielectric constants of the layers into account [133, 134]. The inset of Fig. 3.3(c) schematically show the geometry where we consider 40 nm SiGe, 1 nm Si, 5 nm Al_2O_3, and 45 nm Al layers above the surface of Si layer where the dot is formed. Here, the distance between the trap and the gate surface is very important as it determines the strength of the metallic screening. To estimate it, we consider a double-dot geometry with an interdot separation of 200 nm, and calculate the shifts in detuning due to the occupied trap. In the inset of Fig. 3.3(c), we also show the detuning

shift due to a trap 0.1 nm below the gate surface, and in 50 nm lateral proximity of the dot, is in 4-9 μeV range, which is comparable to the experimental values of the detuning fluctuation amplitudes σ_ε in Si/SiGe dots that are in 0.87-11 μeV range [135, 81, 136, 40]. Finally, the main panel of Fig. 3.3(c) shows the shifts in the ST splitting at $\hbar\omega = 550$ μeV and at $\hbar\omega = 650$ μeV as a function of the x position of the trap (the dot is centered at $x = 0$, both the dot and the trap are centered at $y = 0$). Note that at $\hbar\omega = 550$ μeV the first-excited state is an orbital triplet and at $\hbar\omega = 650$ μeV it is a valley triplet.

To further connect our calculations with experiments, we want to estimate dephasing rates. For a double-dot, charge-noise-induced dephasing follows the relation $\Gamma_2^* = \frac{1}{\sqrt{2}\hbar}|\partial E_Q/\partial\varepsilon|\sigma_\varepsilon$ [113, 137, 89]. So, we estimate dephasing rates as $\Gamma_2^* \approx \frac{1}{\sqrt{2}\hbar}\frac{\delta E_{\mathrm{ST}}}{2}$ using the shifts in ST splittings calculated as in Eq. 3.6 and 3.7. We note that, with the assumption of equal trapping and detrapping rates, the standard deviation of the shifts in the ST splittings is half of the amplitude of these shifts, bringing the factor of 2 in the denominator. The right-hand-side vertical axis on the main panel of Fig. 3.3(c) shows these dephasing rate estimations. We find that by changing the confinement strength by 100 μeV dephasing rate can change by at least one to four, depending on the lateral position of the trap. We also observe that the dephasing rates at $\hbar\omega = 550$ μeV, associated with $E_{\mathrm{ST}_{\mathrm{val}}}$, take values comparable to experimental values of a few MHz [81].

3.3 Summary

Using a combination of tight-binding and full-configuration interaction calculations, we have shown that in a two-electron Si/SiGe QD, a significant change in dephasing time Γ_2^* can be observed by tuning the confinement strength through a transition where the similarity of the charge densities of the lowest two states significantly change, and therefore amplitude of the fluctuations of their energy difference due to charge noise is different. The mechanism that allows this is a transition in the first-excited state in strongly-correlated electron regime that can be controlled via effective e-e interaction strength, i.e. confinement strength. In addition to strong e-e interactions, valley physics of silicon and interface-disorder-induced valley-orbit coupling play crucial role in this mechanism. These results contribute to the physical understanding of charge noise effects on Si/SiGe QDs.

This work was supported in part by ARO through Award No. W911NF-17-1-0274 and the Vannevar Bush Faculty Fellowship program sponsored by the Basic Research Office of the Assistant Secretary of Defense for Research and Engineering and funded by the Office of Naval Research through Grant No. N00014-15-1-0029. The views and conclusions contained in this document are those of the authors and should not be interpreted as representing the official policies, either expressed or implied, of the U.S. Government. The U.S. Government is authorized to reproduce and distribute reprints for Government purposes notwithstanding any copyright notation herein. This research was performed using the compute resources and assistance of the UW-Madison Center For High Throughput Computing (CHTC) in the Department of Computer Sciences. The CHTC is supported by UW-Madison, the Ad-

vanced Computing Initiative, the Wisconsin Alumni Research Foundation, the Wisconsin Institutes for Discovery, and the National Science Foundation, and is an active member of the Open Science Grid, which is supported by the National Science Foundation and the U.S. Department of Energy's Office of Science.

Chapter 4

How valley-orbit states in silicon quantum dots probe quantum well interfaces

This chapter is adapted from the manuscript "How valley-orbit states in silicon quantum dots probe quantum well interfaces", which can be found at arXiv:2103.14702, and which is currently under review.

4.1 Introduction

The ability to make uniform and tunable qubits is crucial for large-scale applications. Modern computers use one control electrode per field effect transistor with excellent uniformity, and proposed architectures for quantum chips also rely on a small number of control

lines per qubit, in order to minimize the density of control wires [138, 139]. Progress has recently been made enhancing the homogeneity of the electrical environment by using quantum dot designs that eliminate modulation doping and instead make use of metal surface electrodes to both accumulate and deplete electrons [46]. The resulting structures enable good control over electron occupation, gate voltages, and tunnel couplings between quantum dots with a small number of gate electrodes per quantum dot [48, 47, 49, 107, 140, 41, 141, 142].

Uniformity remains a challenge with regards to conduction band valley energies in silicon [143, 62], and important physical questions need to be addressed. Atomistic disorder is known to play a particularly important (and typically uncontrolled) role in determining the energies of electrons at the bottom of the valleys [65, 66, 67, 68, 69, 71], resulting in a wide range of observed valley splittings in Si/SiGe quantum dots (20–270 μeV, [77, 144, 145, 129, 29, 131, 130, 146, 147, 104]). Critically, the interplay between the factors that determine the valley splitting in quantum dots — the atomic details of the interface (which vary with lateral position), the degree of lateral confinement, and electron-electron interactions within a quantum dot — are not yet fully understood.

This chapter reports quantitative characterization of the relationship between low-lying one- and two-electron valley-orbit states and the quantum dot confinement strength, shape, and position. The pulsed-gate spectroscopy and magnetospectroscopy measurements reveal valley splittings in the range 36–87 μeV, two-electron singlet-triplet splittings between 22–59 μeV, and orbital splittings that can be tuned from 1.69–2.26 meV. Simulations combining full configuration interaction (FCI) [92] with empirical tight-binding (TB) theory [88] are shown

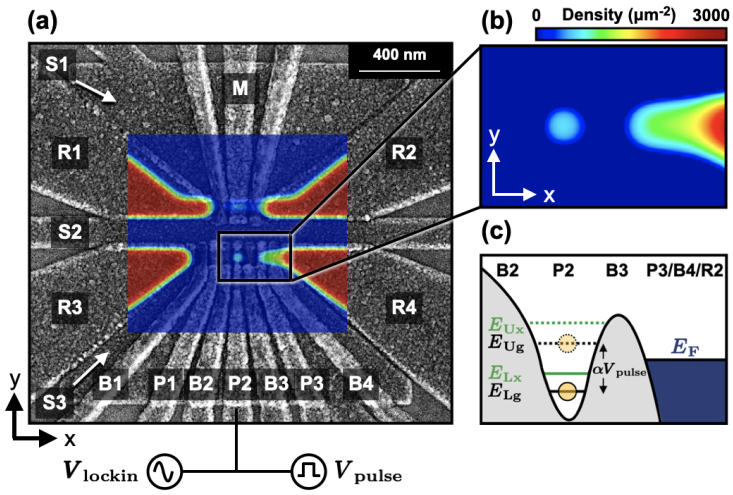

Figure 4.1: (a) A scanning electron microscope (SEM) image of a device lithographically identical to the one measured shows the gate electrode layout in the active region. A COMSOL Multiphysics Thomas-Fermi simulation of the electron density is overlaid on the SEM image. The sensor dot under gate M measures the average charge occupation $\langle n|n\rangle$ of the P2 quantum dot via lock-in amplifier detection at frequency f_{lockin}. (b) The COMSOL simulation shows the charge density of the P2 dot, where the tunnel barrier to the left(right) reservoir is opaque(transparent). (c) Valley-orbit state splittings are measured using pulsed-gate spectroscopy. A square pulse with amplitude V_{pulse} at frequency f_{pulse} is applied to gate P2, rapidly pulsing the chemical potential of the P2 dot between E_{Lg} and E_{Ug}. The change in chemical potential induces detectable shifts in the tunnel rate into and out of the P2 quantum dot, allowing for measurement of excited state energies.

to be in good agreement with the experimental results, and together these methods enable an understanding of the interplay between effects arising from quantum well interface roughness, orbital confinement strength, and electron-electron (e-e) interactions. This combination of experiment and theory not only explains the origin of the energy spectrum but also provides a new method for probing the quantum well interface.

4.2 Experimental methods

Spectroscopy of one- and two-electron valley-orbit states is performed in a device fabricated using a three-layer overlapping aluminum gate architecture [46], as shown in Fig. 4.1(a). A detailed fabrication process can be found in Ref. [107]. The integrated sensor dot under gate M measures the electron occupation of the central quantum dot under gate P2. The triple-dot on the bottom side is tuned into a regime where B1 and P1 form a large tunnel barrier on the left side of P2, suppressing the tunnel rate into reservoir R3. Gates P3 and B4 extend the reservoir R4 into the quantum dot channel, as shown by the electron density heat map in Fig. 4.1(b), allowing for the tunnel barrier beneath gate B3 to tune the tunnel coupling between the P2 dot and right reservoir under R4. The electron temperature is measured to be $T_e = 100$ mK.

One- and two-electron valley-orbit splittings are measured by pulsed-gate spectroscopy using the experimental setup shown in Fig. 4.1(c). A square voltage pulse with amplitude V_{pulse} and frequency f_{pulse} is applied to gate P2, pulsing the ground state of the quantum dot between two levels: E_{Lg} and $E_{\text{Ug}} = E_{\text{Lg}} + \alpha V_{\text{pulse}}$, where $E_{\text{Lg}}(E_{\text{Ug}})$ denotes the ground state of

the dot in the loading(unloading) position, and α is the lever arm for gate P2. A measurable change in the average electron occupation of the dot $\langle n|n\rangle$ occurs when an excited state provides an additional channel for the electron to enter the dot, yielding a measurement of the energy of this excited state [148, 105, 149].

4.3 Results

4.3.1 Measurement results

Fig. 4.2(a, b) show pulsed-gate spectroscopy measurements of the one-electron E_{orb}. The excited orbital state is separated well enough from the ground state such that each peak position is found by fitting to $\cosh^{-2}(\alpha V_{P2}/2k_BT_e)$ [150], where $E_{\text{orb}} = \alpha\Delta V_{\text{orb}}$. As shown in Fig. 4.2(c, d), a similar procedure is used to measure the valley splitting. In this case, there is overlap of the ground and lowest excited state signals that arises from thermal broadening. To extract the peak locations, we make use of an expression for $\langle n|n\rangle$,

$$\langle n|n\rangle = \sum_{i=g,x} \Gamma_i \frac{e^{(E_i-E_F)/E_{0i}}}{e^{(E_i-E_F)/k_BT_e}+1}, \tag{4.1}$$

where $E_i = \alpha V_i$ is the position of each peak in energy, and E_{0i} and Γ_i are fitting parameters for each peak. As shown by the solid line in Fig. 2(d), the experimental data are fit by the derivative of Eqn. 4.1 with respect to the gate voltage ($d\langle n|n\rangle/dV_{\text{P2}}$), enabling extraction of $E_{\text{val}} = \alpha\Delta V_{\text{val}}$.

The two-electron singlet-triplet splitting E_{ST} is measured using both pulsed-gate spec-

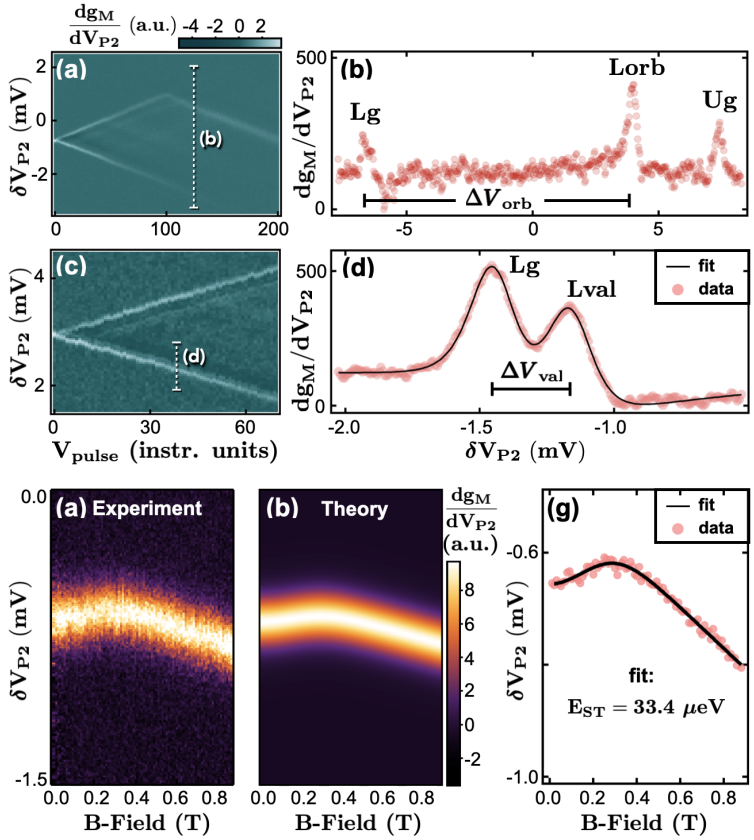

Figure 4.2: (a, b) Measurement of orbital splitting using pulsed-gate spectroscopy. The pulse amplitude is increased until the lowest-lying orbital state is visible, shown in (a). A line cut (dashed line) is taken when the pulse amplitude exceeds the orbital splitting, allowing detection of the ground (Lg) and excited orbital (Lorb) states, shown as the peaks in (b). The orbital splitting is given by $\alpha\Delta V_{\text{orb}}$. (c, d) Using the same method, the valley (E_{val}) and singlet-triplet splittings (E_{ST}) are measured. The red data points clearly show two distinct peaks in (d). The data is fit using Eqn. 4.1, shown as the black line, giving $E_{\text{val}} = \alpha\Delta V_{\text{val}} = 53.2$ μeV. (e-g) Experimental magnetospectroscopy data (e) is reproduced in (f) by treating the dot-reservoir system as a grand canonical ensemble. The experimental peak locations in voltage space are extracted from (e) and plotted in (g) as red circles, which are then fit to Eqn 4.2, yielding $E_{\text{ST}} = 33.4$ μeV.

troscopy (using a similar procedure as above) and magnetospectroscopy [151, 152, 129, 145], as shown in Fig. 4.2(e-g). A full theoretical model for magnetospectroscopy is developed in Sec. C.1 which allows for the experimental data shown in Fig. 4.2(e) to be closely reproduced by the model in Fig. 4.2(f). This model enables fitting the peak position of the data in Fig. 4.2(e), using

$$V_{P2}(B) = \frac{1}{\alpha\beta_e} \ln\left(\frac{e^{\frac{1}{2}\kappa B + \beta_e E_{\mathrm{ST}}}\left(e^{\kappa B}+1\right)}{e^{\kappa B} + e^{2\kappa B} + e^{\kappa B + \beta_e E_{\mathrm{ST}}} + 1}\right), \tag{4.2}$$

where V_{P2} is the gate voltage, $\kappa = g\mu_B\beta_e$ where $\beta_e = 1/k_B T_e$, g is the electron g-factor, μ_B is the Bohr magneton, and B is the magnetic field. The peak positions from Fig. 4.2(e) are extracted and plotted as red circles in Fig. 4.2(g), and the fit (solid line) to Eqn. 4.2 yields for this example $E_{\mathrm{ST}} = 33.4$ μeV.

Using these spectroscopic techniques, E_{val}, E_{ST} and E_{orb} are measured as a function of electrostatic confinement in the x-y plane. The confinement is varied by changing the S3 gate voltage (V_{S3}) between 260–420 mV while compensating with neighboring barrier/plunger gates to maintain a constant electron occupation and tunnel rate into the dot.

Figure 4.3 shows the effects of changing V_{S3} on quantum dot orbital energy, shape, and position. The device schematic pictured in the top left inset shows the approximate location of the P2 dot as the shaded blue region. Changes to the voltage V_{S3} applied to the screening gate, shown as the shaded gray region in the inset, modify the P2 dot confinement, orbital shape, and position. The minimum orbital splitting, plotted as solid circles in Figure 4.3, is found to be non-monotonic with V_{S3}, because of the strong effect S3 has on the electrostatic

confinement of the dot along the y-axis. At high V_{S3}, the y-confinement becomes weak, and the minimum orbital splitting falls off rapidly due to elongation of the dot along the y-axis. Towards the center, the dot becomes isotropic, increasing the minimum orbital splitting up to 2.26 meV at $V_{S3} = 370$ mV. At low V_{S3}, suppression of the minimum orbital splitting occurs due to the compensating barrier and plunger gate voltages needed to stay in the one-electron regime, elongating the dot along the x-axis. Since low V_{S3} creates a tight confinement potential along the y-axis, the x-orbital is the most weakly confined orbital below $V_{S3} = 370$ mV.

4.3.2 Thomas-Fermi simulations

This behavior is well explained by semiclassical (Thomas-Fermi) electrostatic simulations using COMSOL Multiphysics, shown in the bottom inset of Fig. 4.3. The position and orbital shape are simulated at the four points indicated by the shaded purple circles from the experimental data. The outline of each oval represents the shape that encloses 50% of the electron wave function, and the small circles show the center of the electron density for each simulation. The Thomas-Fermi (TF) simulations qualitatively match the experimental findings, where the x-orbital is most weakly confined at low V_{S3} and the y-orbital is most weakly confined at high V_{S3}. In addition to the changes in shape, significant change in the position of the dot is observed in the COMSOL simulations. Over the range shown, the quantum dot position slides down and to the left as V_{S3} increases for a total change in position of 27.5 nm. We note that COMSOL simulations were not used to determine the dot

shape and position above 390 mV, because this regime becomes close to the accumulation threshold for the S3 gate, where uncertainties become large.

4.3.3 TB and FCI simulations

Atomic steps in the quantum well interface play an important role in determining E_{val} and E_{ST}. Fig. 4.4(a) plots E_{val} (filled blue squares) and E_{ST} (filled red circles) as the orbital shape and dot position are varied with V_{S3}, where the shaded region represents the measurement uncertainty. The measured E_{val} and E_{ST} change substantially across the electrostatic configurations, and their large *in situ* tunability arises from motion of the P2 quantum dot with respect to atomic steps at the quantum well interface. As the dot approaches an atomic step, more of the wave function overlaps the step, thereby increasing the valley-orbit coupling which suppresses E_{val} and E_{ST} [37]. To determine the position of atomic steps relative to the quantum dot, we make use of a combination of the experimental measurements, the COMSOL simulations just described, and FCI calculations, the latter of which incorporate valley-orbit coupling that arises from interface roughness. The FCI calculations use a single fitting parameter in order to match the measured values of E_{val} and E_{ST} namely, the position of the dot relative to atomic steps at the quantum well interface.

Figure 4.4(a) shows the results of FCI calculations for E_{val} and E_{ST} as open blue squares and open red circles, respectively. Close agreement with the experimental data is found when the atomic steps are separated by 35 nm. The positions used in the FCI calculations to produce the best fit to the data at each point are plotted in Fig. 4.4(b) as solid colored

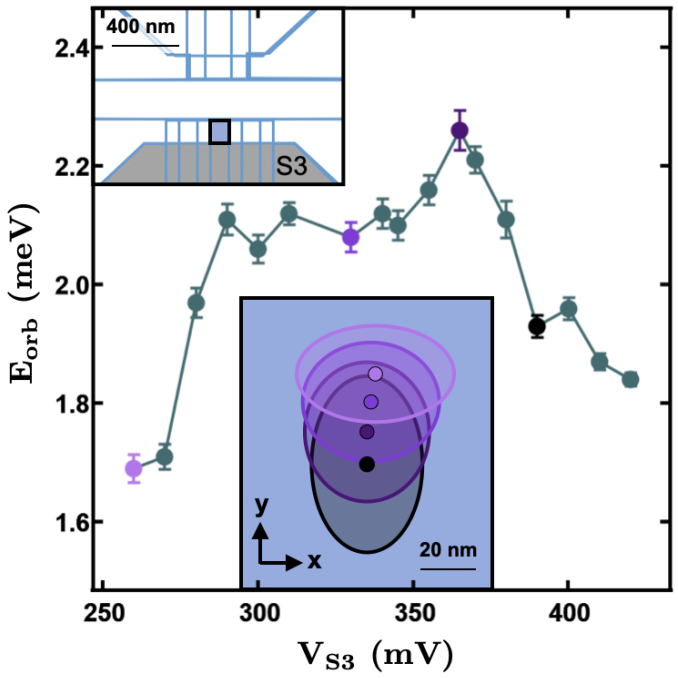

Figure 4.3: Quantum dot orbital shape and position. The top left inset shows a device schematic where the P2 quantum dot is located within the filled blue region and the S3 gate is shown as the filled gray region. The minimum orbital splitting is plotted as a function of V_{S3}. At low V_{S3}, the dot has strong y-confinement and weak x-confinement, leading to a drop in the minimum orbital splitting. As V_{S3} is increased, the dot becomes isotropic, increasing the minimum orbital splitting. At high V_{S3}, the dot has weak y-confinement and strong x-confinement, reducing the minimum orbital splitting again. Thomas-Fermi electrostatic simulations are used to calculate the quantum dot shape and position within the blue region shown in the device schematic. Four points are simulated, shown as the shaded purple circles in the experimental data. The change in shape of the electron density is found to be in agreement with the experimental data. Additionally, the position of the quantum dot for each simulation is illustrated as the small solid circle in the inset, showing that the quantum dot slides down and to the left 27.5 nm.

points. Each point has a colored gradient overlay that represents the spatial extent of the singlet (ground) state with respect to the atomic steps, which are shown as black dashed lines. The gradient steps from darkest to lightest, corresponding to wave function probability thresholds of 75%, 50%, and 25% of its maximum value.

A linear fit to the dot positions calculated from the FCI simulations reveal a total change in position of the dot of 24.7 nm, which is remarkably close to the 27.5 nm change in position extracted from the COMSOL simulations, given that these two methods are based on different physical inputs. This correspondence can also be seen by comparing the FCI results to the open purple circles in Fig. 4.4(b), which shows the central dot position extracted from the four COMSOL simulations. The close agreement provides a measure of validation for an approach that allows an *in situ* method of probing the quantum well interface through a combination of spectroscopic measurements of the quantum dot and theoretical simulations. We note that in future work, more detailed information could be determined by moving the dot along two axes.

The inset of Fig. 4.4(a) reports the ratio $E_{\mathrm{ST}}/E_{\mathrm{val}}$ as a function of E_{orb}, showing that this ratio is significantly below unity for the entire range of parameters measured. Electron-electron interactions suppress E_{ST} below the non-interacting energy E_{val} [61], revealing that there are strong e-e interactions across all orbital splittings studied here (1.69–2.26 meV). To look for any correlations between dot position relative to the steps and the ratio $E_{\mathrm{ST}}/E_{\mathrm{val}}$, the dot positions in Fig. 4.4(b) are color coded by their corresponding orbital energies, with the mapping shown in the inset plot. The random distribution of colors in Fig. 4.4(b)

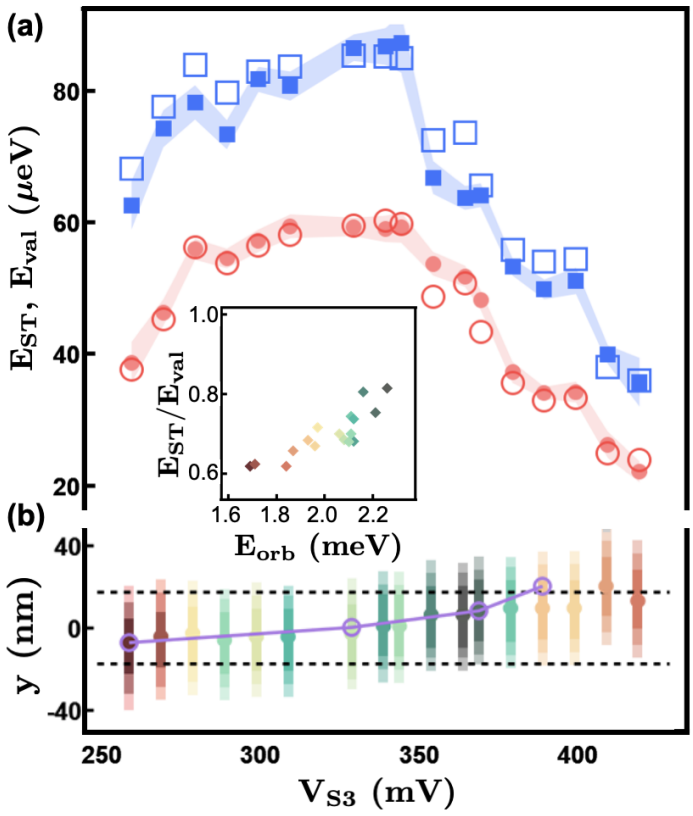

Figure 4.4: (a) The measured valley splitting (E_{val}) and singlet-triplet splitting (E_{ST}) are plotted as a function of V_{S3} as filled blue squares and red circles, respectively, where the measurement uncertainty is indicated by the width of the shaded regions. FCI simulations for E_{val} and E_{ST}, shown as open blue squares and red circles, respectively, quantitatively reproduce the experimental data once the effects of disorder in the form of atomic steps at the quantum well interface are included. (b) The non-monotonic behavior observed in both E_{ST} and E_{val} as a function V_{S3} is well explained by the quantum dot position changing with respect to distinct atomic steps at the quantum well interface. The wave function and position of the P2 dot singlet state is plotted with respect to atomic steps (dashed lines) at the interface, shown as the colored gradients and points. A best fit to the data produces a smooth change in position of the dot across steps spaced approximately 35 nm apart. In addition, the change in position from the Thomas-Fermi simulation, plotted as the purple line and open circles, agrees well with the FCI simulations. The inset plots the ratio $E_{\mathrm{ST}}/E_{\mathrm{val}}$ as a function of the orbital splitting (E_{orb}). The suppression of the ratio $E_{\mathrm{ST}}/E_{\mathrm{val}}$ below unity is a consequence of strong electron-electron interactions.

demonstrates that orbital energy spacing is more important than dot position in determining the suppression of E_{ST} below its non-interacting limit of E_{val}.

4.4 Summary

In summary, we measure large *in situ* tunability of valley, singlet-triplet, and orbital splittings, allowing for determination of the quantitative relationship between these three important energy scales. FCI simulations of the measured valley-orbit states were found to be in good agreement with the data, pointing to a combination of two primary physical parameters driving the relationship between these valley-orbit states: electrostatic confinement strength and quantum dot position relative to steps in the quantum well interface. This improved understanding enables a new *in situ* method of probing the quantum well interface through a combination of spectroscopic data and theoretical simulations.

The derivation of Eqns. 1 and 2, details of the COMSOL simulations, and details of the FCI calculations are provided in the Supplemental Material.

Research was sponsored in part by the Army Research Office (ARO) under Grant Numbers W911NF-17-1-0274 and by the Vannevar Bush Faculty Fellowship program under ONR grant number N00014-15-1-0029. We acknowledge the use of facilities supported by NSF through the UW-Madison MRSEC (DMR-1720415) and the NSF MRI program (DMR-1625348). The views and conclusions contained in this document are those of the authors and should not be interpreted as representing the official policies, either expressed or implied, of the Army Research Office (ARO), or the U.S. Government. The U.S. Government

Chapter 5

Coherent control and spectroscopy of a semiconductor quantum dot Wigner molecule

This chapter is adapted from the manuscript "Coherent control and spectroscopy of a semiconductor quantum dot Wigner molecule", which can be found at arXiv:2009.13572, and which is currently under review.

5.1 Introduction

Semiconductor quantum dots containing more than one electron have extremely desirable properties for constructing and operating qubits. For single spin qubits, manipulating electrons above closed shells makes electric-field driving more effective [54, 53], and certain

qubits like quantum dot hybrid qubits [29] rely on multielectron filling to define the qubit states themselves. Two-electron eigenstate energies are particularly important for quantum dot qubits, since singlet-triplet splittings result in Pauli spin-blockade [153], which provides a readout mechanism for singlet-triplet qubits [20, 154, 122], exchange based qubits [84, 86], and quantum dot hybrid qubits [27, 29]. Pauli blockade can also be used to read out single spin qubits [87], which is useful for high temperature operation [138, 55, 54]. When the characteristic interaction energy between electrons becomes larger than the orbital confinement energy, electronic states develop correlations and localize, leading to the formation of Wigner molecules [56, 32, 155, 33, 156, 157]. Imaging of localization in Wigner molecules has been achieved using scanning electronic [158] and near-field optical [159] methods. The lowest-lying excited states in such molecules have been studied using both optical [160, 60] and transport spectroscopy [35, 161], and the latter method has been used to observe a reduction in symmetric-antisymmetric orbital splittings [61]. Thus, while the transition to Wigner-type localization is known to reduce the gap between the ground and first orbital excited state, the impact on higher lying states has not been observed in experiment, and quantum control of such states has not been explored.

In this chapter we report pulsed microwave coherent control and spectroscopy of an electrostatically-confined semiconductor double quantum dot in the Wigner-molecule regime. We report coherent Rabi control of eight distinct resonances ranging in frequency from 3.3 to 8.3 GHz, corresponding to energies far smaller than the single-particle confinement energy. With Ramsey spectroscopy, we map the energy as a function of double-dot detuning for

two of these resonances. Using full configuration interaction (FCI) calculations, we argue that the origin of this dense manifold of electronic states is strong correlations and Wigner molecule physics. Time-domain simulations of the Rabi experiments are used to explain the evolution of the Rabi oscillations as a function of detuning energy. The full set of experimental spectroscopy results can be fit by a simple model consisting of a set of two-electron states in the right quantum dot tunnel coupled to the lowest lying state in the left dot.

5.2 Experimental methods

Fig. 5.1(a) describes the quantum dots used here, which form in an undoped Si/SiGe heterostructure with three layers of overlapping gates [45]. Fabrication details can be found in Ref. [107]. While the device is capable of hosting three dots, here we make use of the two dots under gates P1 and P2, accumulating the rightmost dot as part of the electron reservoir. We operate the double quantum dot (DQD) with a total of five electrons near the (4,1)-(3,2) anticrossing, as shown schematically in Fig. 1(b-d). Tunnel rates between the two dots and to the left and right reservoirs are set by gates B1, B2, and B3. Charge sensing is performed with dot CS, and its current is measured using a two-stage cryogenic HEMT amplifier [162] mounted on a separate printed circuit board (PCB) connected to the sample PCB by stainless steel coax.

5.3 Results

5.3.1 Pulsed microwave coherent control and spectroscopy

We initialize at setting I, shown in Fig. 5.1(b), into the (4,1) ground state, which has a large splitting between the ground and first excited states. We ramp the detuning across the interdot transition line to a manipulation point (M) in positive detuning where we perform microwave pulse sequences. Rabi and detuned Ramsey pulses at M drive coherent rotations between states in the (3,2) DQD. To perform readout, we adiabatically ramp back across the interdot transition line: while the (3,2) ground state maps to the (4,1) ground state (R_0), the (3,2) excited states maintain their charge configuration (R_1). Latched measurement [163] is used to enhance readout: an electron in the right-hand dot of the (3,2)
charge state at R_1 rapidly tunnels into the right reservoir to form the metastable (3,1) charge state before slowly returning to the (4,1) ground state. The latch duration is determined by the left barrier, which is tuned to have a long tunnel time.

Figure 5.1(e-j) demonstrate coherent spectroscopy of two different transitions of the DQD, using the methods from Ref. [81]. Fig. 5.1(e,f) shows the Rabi and Ramsey control pulses; the Rabi pulse consists of one continuous microwave drive of frequency f_{R}, while the Ramsey pulse has two $\pi/2$ microwave pulses of frequency f_{R} surrounding a dc detuning ramp. The resulting Rabi and Ramsey oscillations are shown in Fig. 5.1(g,h) and Fig. 5.1(i,j) for f_{R} of 8.33 GHz and 7.30 GHz, respectively. The vertical axis δV_{P2} determines the detuning, and the centers of the Rabi chevrons in Fig. 5.1(g,i) correspond to the detuning values where

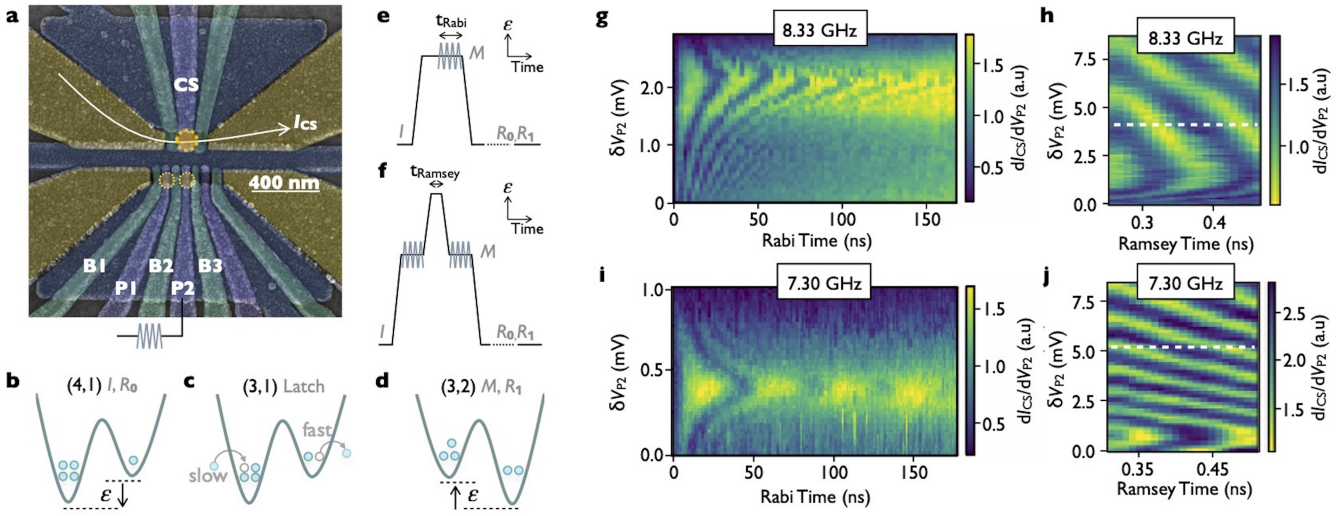

Figure 5.1: Device setup and Rabi and Ramsey measurements. (a) A false-color micrograph of a device lithographically identical to that measured here. Quantum dots are formed under P1 and P2. A current I_{CS} flows under the dot controlled by gate CS and is used to detect the electron occupation of the P1 and P2 dots. (b) The ground state for the 5-electron system at negative detuning ε is the (4,1) charge configuration. It is used for initialization I and during readout R_0. (c) The tunnel rates to the left and right reservoirs are tuned such that (3,1) state is metastable, allowing for latched readout. (d) The ground state for the 5-electron system at positive detuning such that the double dot is in the (3,2) charge configuration, used for manipulation M and readout R_1. (e) Rabi pulse sequence used in this work. (f) Ramsey pulse sequence used in this work, comprised of two $\pi/2$ pulses on either side of a detuning pulse. (g-j) Rabi and detuned-Ramsey measurements of two coexisting states. (g,h) Rabi and Ramsey oscillations using $f_{\mathrm{R}} = 8.33$ GHz. (i,j) Rabi and Ramsey oscillations using $f_{\mathrm{R}} = 7.30$ GHz, taken at the same device tuning but different detuning value from (g,h). For the Rabi measurements in (g, i), δV_{P2} corresponds to a shift of the entire pulse sequence, while for the Ramsey measurements in (h,j), δV_{P2} corresponds to the height of the detuned dc pulse between the microwave bursts. Dashed white lines in (h,j) denote the value of δV_{P2} for which the Ramsey detuning is zero.

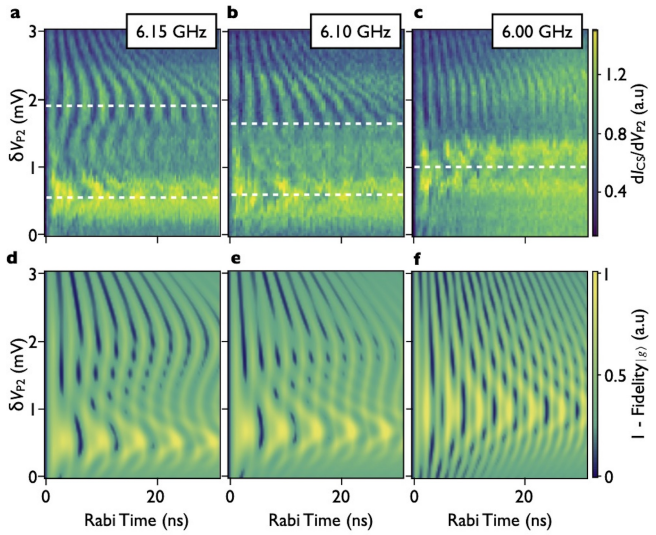

Figure 5.2: Simulations of Rabi oscillations. (a) Rabi oscillations with $f_{\mathrm{R}} = 6.15\,\mathrm{GHz}$, with the centers of two on-resonance oscillations marked by a dashed line. (b) Rabi oscillations with $f_{\mathrm{R}} = 6.10\,\mathrm{GHz}$. Note that the two resonances move closer together along the detuning axes, as compared with (a). (c) Rabi oscillations with $f_{\mathrm{R}} = 6.00\,\mathrm{GHz}$, where the on-resonance locations have completely merged. (d-f) Simulated Rabi oscillations corresponding to (a-c) using the simplified model described in Sec. D.2.

f_{R} is resonant with the transition energy. Ramsey fringes like those in Fig. 5.1(h,j) allow measurement of the energy difference as a function of detuning (Fig. D.1).

Figure 5.2 shows Rabi oscillations with two distinct resonances visible in the same plot. In Fig. 5.2(a), the Rabi drive frequency $f_{\mathrm{R}} = 6.15\,\mathrm{GHz}$, and the detunings corresponding to on-resonance oscillations are indicated by the white dashed lines in the figure. As the driving frequency is reduced to 6.10 GHz (Fig. 5.2(b)), the centers of the Rabi patterns move closer together, and in Fig. 5.2(c) the oscillations overlap at $\delta V_{\mathrm{P2}} = 1\,\mathrm{mV}$. Numerical simulations of these oscillations are shown in Fig. 5.2(d-f), using the model described in Sec. D.2. A key feature of these two oscillations is the difference in width as a function of δV_{P2}; this behavior is reproduced in the theoretical model by different slopes for the respective energy

dispersions, where a flatter slope corresponds to wider oscillations. The unusual merging of the resonances is reproduced in the model with a level-crossing, which we discuss further below.

Figures 5.1 and 5.2 above report four resonances as a function of the gate voltages defining the quantum dot. Additional Rabi measurements over a wide range of frequencies are included in Fig. D.2, D.3. In total this data demonstrates Rabi driving of eight distinct transitions below 10 GHz, an unusual density of resonances that cannot be described by non-interacting two-electron physics. We must therefore consider how electron-electron interactions influence the excited energy level spectrum.

5.3.2 FCI simulations

Here, we use FCI methods to compute the energy levels in the two-electron quantum dot [156]. We find that the best correspondence between theory and experiment is achieved by assuming a valley splitting of 3.81 GHz and an orbital confinement $E_{\mathrm{orb}}/h = 59.2\,\mathrm{GHz}$. It is interesting to first consider the noninteracting case, for which the lowest singlet state is constructed from the two lowest single-electron orbitals, while the lowest triplet is constructed from the ground and first excited states. We obtain these and the other low-lying, non-interacting two-electron eigenstates by simply turning off the Coulomb interactions in the FCI code, obtaining the yellow points in Fig. 5.3(a). In contrast, the fully interacting case is shown in blue (Sec. D.4 and Ch. 2). For the fully interacting case, when interactions are larger than valley or orbital excitation energies, the eigenstates are composed of contributions

from many single-electron states. In Fig. 5.3(a), we observe the emergence of level manifolds; for eigenstates within a given manifold, single-particle contributions and electron correlation effects can be very similar in magnitude, and opposite in sign, resulting in a much smaller energy difference than in the non-interacting limit (Sec. D.5). For the parameters considered here, strong interactions yield a dense set of levels, with a total of 19 excited states below 50 GHz, instead of the two states obtained in the noninteracting limit. Interactions also suppress the energy splitting between the two lowest energy states to below 1 GHz.

Wigner molecules with localized electrons are known to arise in systems with a high ratio $R_{\mathrm{W}} = E_{\mathrm{ee}} \,/\, E_{\mathrm{orb}}$ between the electron-electron interaction energy E_{ee} and the energy of the lowest quantum dot orbital excitation energy E_{orb}. Typical estimates for the formation of Wigner molecules are of order $R_{\mathrm{W}} = 1.5$ [35, 160, 60, 61, 159]. Here, using E_{orb}, we find $R_{\mathrm{W}} = 12.74$, consistent with the formation of a Wigner molecule (Sec. D.5). The estimate for E_{orb} used to compute R_{W} also yields a dot radius of 40 nm, derived from the classical turning point $\sqrt{\hbar/(m_t\omega_x)}$, giving an 80 nm diameter that is consistent with a quantum dot situated in a 90 nm channel underneath a gate 70 nm wide. We note that, if we use any of the two-electron excited state energies reported here to estimate the dot diameter in a noninteracting electron model, it would give a dot diameter over 200 nm, much larger than the size expected from the physical dimensions of the electrostatic gates in the

Figure 5.3(b-e) shows electron density plots corresponding to the blue energy levels in Fig. 5.3(a), separated into four different manifolds, as indicated by the solid, dashed, and dotted bounding boxes. It is clear that these Wigner molecule eigenstates cannot be easily

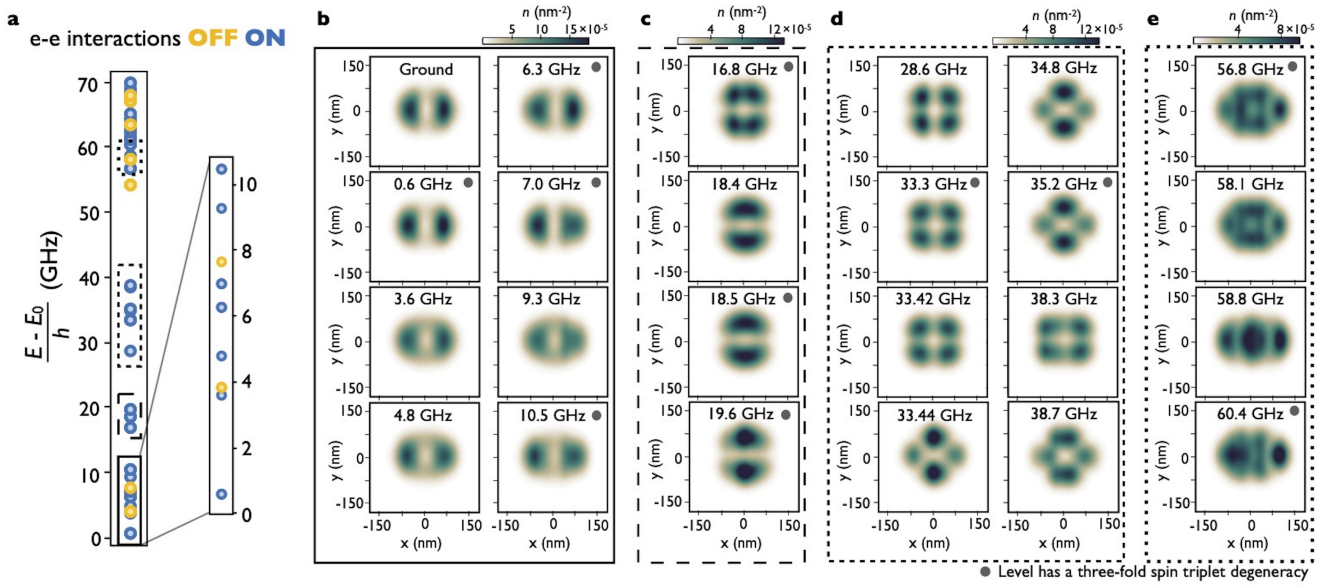

Figure 5.3: Interaction effects. (a) Excited state energies for a two-electron parabolic dot described by the energy $\hbar\omega_x$, with $\omega_x/2\pi = 59.2$ GHz ($\hbar\omega_y = 1.07\ \hbar\omega_x$), calculated using FCI with (blue) and without (yellow) interactions. (b-e) Electron density for the blue levels in (a) with each panel corresponding to a boxed cluster of levels with the corresponding border style.

constructed from low-energy, single-electron orbital states. This manifold structure also helps to explain the energy spectrum in Fig. 5.3(a), since the gaps in the calculated spectrum correspond to changes in the spatial pattern of electron localization. Energy separations within a given manifold can be attributed to slight differences in orbital configurations and to varying contributions from valley excitations. Larger energy gaps between the manifolds correspond to characteristic changes in the electron localization.

5.3.3 Energy spectrum

Figure 5.4(a) shows the eigenvalues of a simple Hamiltonian (Eq. D.3) motivated by the energy levels reported in Fig. 5.3, which we use to fit the Rabi and Ramsey data reported in this work. In Fig. 5.4(b) we plot in teal the difference in energy between the ground and excited states; we plot in yellow the difference between these same states and the first excited state energy ($E_1/h = 0.75$ GHz). Although we do not directly observe this state, E_1, its presence is motivated by the FCI calculations described above, and we infer its existence and energy for reasons discussed below and in Sec. D.6. In the experiments, this state has nonzero initialization occupation both because of non-adiabaticity of the pulse sequence (Sec. D.7) and because of thermal excitation caused by electron temperatures of about 100 mK ($k_BT = 2.1$ GHz).

The data shown in Fig. 5.4(b) correspond to all the Rabi and Ramsey spectra reported in this work, as described in the legend. We plot the spectra from Fig. 5.1(h,j) as purple circles and green triangles, and we fit to them the transitions E_{05} and E_{15}, corresponding

to the differences between the ground and first excited states to the fifth excited state. The resonant frequencies from Fig. 5.2(a-c) are shown as navy blue diamonds (for the resonance that moves up between Fig. 2(a) and Fig. 2(c)) and pink diamonds (for the resonance that moves down between Fig. 2(a) and Fig. 2(c)). As discussed earlier, these points merge with decreasing f_{R}, providing additional evidence that these Rabi oscillations are driven from the ground and first excited state; if these two resonances belonged to the same dispersion, they would merge into a single chevron at the dispersion minimum instead of overlapping, as observed in Fig. 5.2(c) and Fig. D.2. If both transitions occurred as excitations from the ground state, a level crossing would only occur if one of the tunnel couplings was anomalously low (≤ 0.1 GHz) which is not supported by the shape of the Ramsey spectra. Finally, the light blue squares in Fig. 5.4(b) show energies corresponding to Rabi oscillations reported in Fig. D.3. The density of transitions in frequency space

as compared with the FCI calculations support the necessity to consider both E_0 and E_1 transitions. In total, Fig 5.4 summarizes the coherent control of eight different resonances in this Wigner molecule.

For the quantum dot hybrid qubit, it is useful to be able to tune the singlet-triplet splitting, where the energies of interest are bounded by temperature on the low end and ease of microwave engineering on the high end. For silicon dots, the non-interacting singlet-triplet energy is given by the valley splitting, which depends on lateral confinement only through wavefunction overlap with interface roughness [65]. For strongly interacting electrons, this valley-like eigenstate gains contributions from many orbital levels, each of which depends

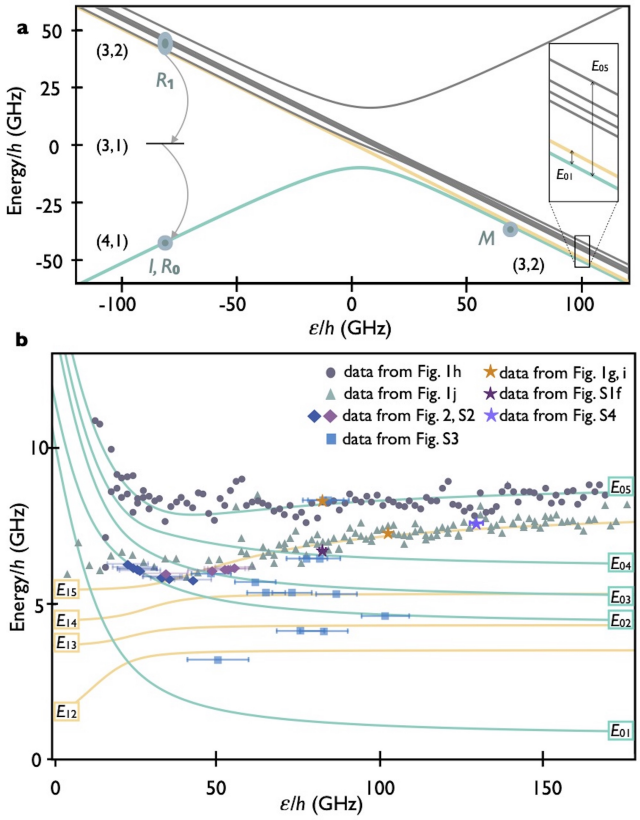

Figure 5.4: Energy spectrum based on a model Hamiltonian. (a) Energy eigenvalues of a model Hamiltonian motivated by the electron interaction effects reported here. Measurement locations from Fig. 1 are indicated. (b) Excited state spectra of the model Hamiltonian. The teal lines are the energy differences between the ground state and energy level n, defined in (a); the yellow lines are differences between the first excited level and the same energy levels in (a). Symbols plotted correspond to frequencies extracted from experiment, as described in the legend.

strongly on lateral confinement. As we show in Fig. D.5(b), the singlet-triplet splitting becomes strongly tunable in the presence of interactions. For the parameters considered here, varying the lateral confinement strength from 55 GHz to 90 GHz in the presence of interactions results in singlet-triplet splittings ranging from 0.18 GHz to 4.42 GHz, a variation of more than a factor of 20; in the non-interacting case this energy varies by only a factor of 2.6.

5.4 Conclusion

In conclusion, we have demonstrated coherent manipulation of a dense ladder of Wigner molecule energy levels. Eight transitions are controlled coherently using Rabi pulse sequences, and two levels are explored in more detail using Ramsey pulse sequences. A six-level model motivated by both experiment and FCI calculations is presented. The presence of such a Wigner-molecular regime with $E_{\mathrm{ee}} \gg E_{\mathrm{orb}}$ provides an additional tool for controlling the energy splittings in gate-defined quantum dots, enabling small changes in confinement to have a large impact on the energy splitting between adjacent levels.

This research was sponsored in part by the Army Research Office (ARO), through Grant No. W911NF-17-1-0274, and by the Vannevar Bush Faculty Fellowship program under ONR grant number N00014-15-1-0029. JC acknowledges support from the National Science Foundation Graduate Research Fellowship Program under Grant No. DGE-1747503 and the Graduate School and the Office of the Vice Chancellor for Research and Graduate Education at the University of Wisconsin-Madison with funding from the Wisconsin Alumni Research

Foundation. We acknowledge the use of facilities supported by the NSF through the UW-Madison MRSEC (DMR-1720415) and by the NSF MRI program (DMR-1625348). The views and conclusions contained in this document are those of the authors and should not be interpreted as representing the official policies, either expressed or implied, of the ARO, NSF, or the U.S. Government. The U.S. Government is authorized to reproduce and distribute reprints for Government purposes notwithstanding any copyright notation herein.

Chapter 6

Conclusion and future work

In this thesis, I have presented a computational strategy that nonperturbatively accounts for strong electron-electron interactions, together with the valley physics of conduction band electrons, and including the effects of interfacial disorder in lithographically-defined quantum dots in Si/SiGe heterostructures. In Ch. 2, a range of confinement and interface profiles were considered, and their effect on one- and two-electron energy splittings were discussed. In Ch. 3, the implications of e-e interactions on the sensitivity of the qubit to charge noise were described. We predicted that a transition of the first-excited state should be induced by changing the confinement strength in an experimentally-relevant regime, and this should lead to a large change in the rate of dephasing between the two qubit levels. In Ch. 4, we demonstrated measurements of one- and two-electron energies and discussed how these provide a new method to probe the quantum well interface when combined with the electrostatic device simulations, and our computational approach presented in the previous chapters. In

Ch. 5, we described observations of a dense set of low-lying energy levels and argued that they emerge as a result of strong e-e interactions, as deduced from our computational approach.

In this work, we have investigated doubly-occupied quantum dots. Looking forward, this approach can be extended to configurations with three or four electrons and different potential profiles (for example, double or triple quantum dots) to get a more complete picture of the energy spectra of current qubit designs. The hybrid qubit, composed of three electrons in a double-dot potential, would be a natural next step. Such an analysis would allow us to study the role of excited multi-electron states in qubit operation. With some modifications, the approach presented here could also be used to explore the energy spectra of qubits with larger number of electrons.

Appendix A

Supplemental information for Chapter 2

A.1 Overview of the calculation strategy

This appendix provides an overview of the calculational methods. The information is summarized in Fig. A.1, which illustrates how the tight-binding and the configuration-interaction methods are integrated.

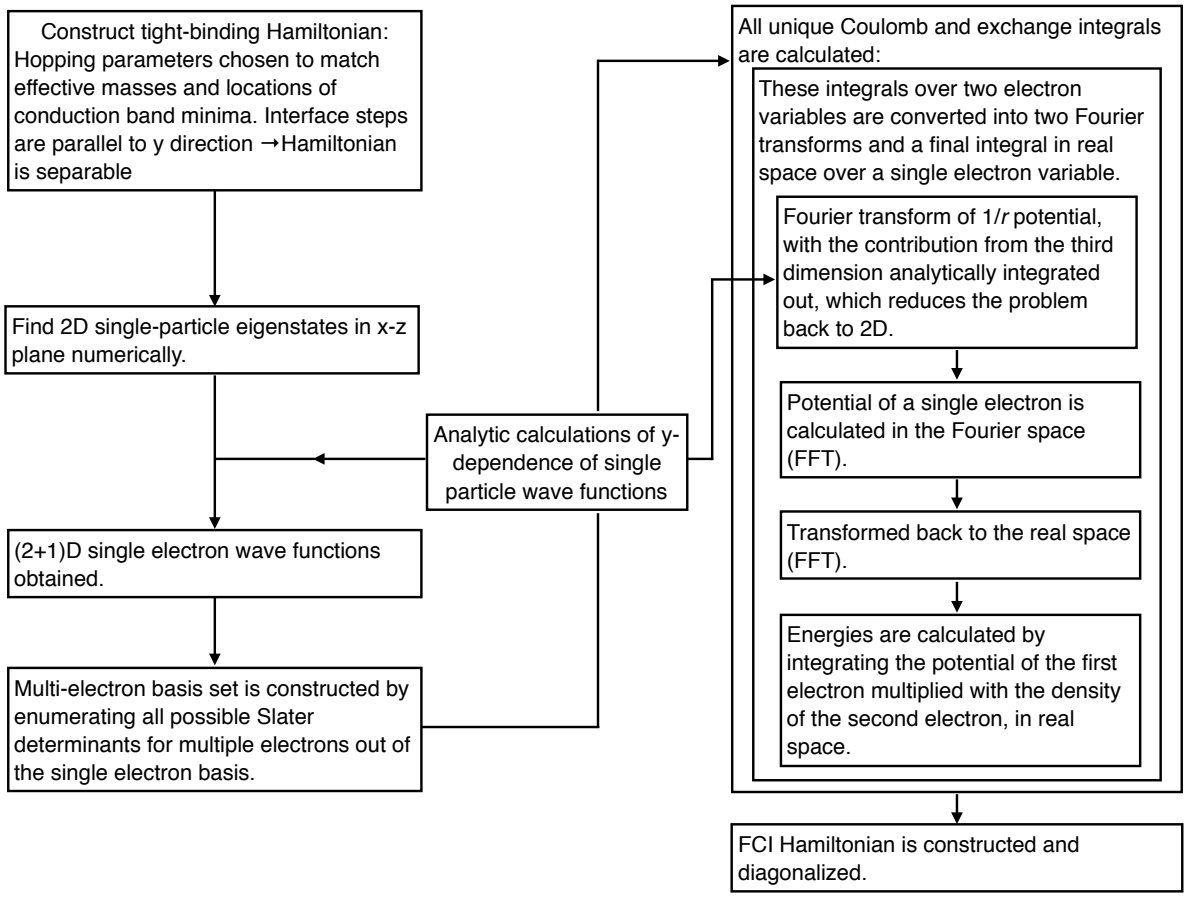

Figure A.1: A flowchart summary of the method used for our calculations, which combines tight-binding calculations that incorporate atomic-scale disorder with full configuration interaction calculations to account nonperturbatively for strong electron-electron interactions.

A.2 Details related to computing the Coulomb matrix elements

This appendix presents details related to the evaluation of Coulomb matrix elements of the form $\langle\psi_\alpha|\, H_{\rm int}\, |\psi_\beta\rangle$.

After the spin degrees are integrated out, the remaining integrals are of the form

$$(i\ j|k\ l) \equiv \int d\boldsymbol{r}_1 d\boldsymbol{r}_2 \phi_i^*(\boldsymbol{r}_1)\phi_j(\boldsymbol{r}_1) H_{\rm int} \phi_k^*(\boldsymbol{r}_2)\phi_l(\boldsymbol{r}_2). \tag{A.1}$$

Since the energy eigenstates are separable, $\phi(x,y,z) = \zeta(x,z)\eta(y)$, the integral becomes

$$\int dx_1 dz_1 dx_2 dz_2 \zeta_i^*(x_1,z_1)\zeta_j(x_1,z_1)\zeta_k^*(x_2,z_2)\zeta_l(x_2,z_2) \int dy_1 dy_2 \frac{\eta_i^*(y_1)\eta_j(y_1)\eta_k^*(y_2)\eta_l(y_2)}{\sqrt{(y_1-y_2)^2+\Delta r_\perp^2}}, \tag{A.2}$$

where $\Delta r_\perp^2 \equiv (x_1-x_2)^2 + (z_1-z_2)^2$.

For the harmonic confinement potentials assumed here, the wavefunctions $\eta(y)$ are harmonic oscillator eigenstates, given by

$$\eta_n(y) = \left(\frac{1}{\pi L^2}\right)^{1/4} \frac{1}{\sqrt{2^n n!}} H_n(y/L) e^{-y^2/2L^2}, \qquad\qquad L \equiv \sqrt{\hbar/m\omega}. \tag{A.3}$$

Hence, the y-integral takes the form

$$f_{ijkl}(\Delta r_\perp) = \sum_{n,m} c_{nm} \int dy_1 dy_2 \frac{y_1^n y_2^m e^{-(y_1^2+y_2^2)/L^2}}{\sqrt{(y_1-y_2)^2+\Delta r_\perp^2}}. \tag{A.4}$$

Now, we make the change of variables $s \equiv y_1 - y_2$ and $t \equiv y_1 + y_2$, such that

$$f_{ijkl}(\Delta r_\perp) = \sum_{n,m} \frac{c_{nm}}{2^{m+n+1}} \sum_{k,p=0}^{n,m} \binom{n}{k}\binom{m}{p}(-1)^p \int ds \frac{s^{n+p-k} e^{-s^2/2L^2}}{\sqrt{s^2+\Delta r_\perp^2}} \int dt\ t^{k+m-p} e^{-t^2/2L^2}. \tag{A.5}$$

These integrals have the following analytical forms:

$$\int ds \frac{s^q e^{-s^2/2L^2}}{\sqrt{s^2+\Delta r_\perp^2}} = \begin{cases} \sqrt{\pi} L^2 (q-1)!!\ U(1/2, \frac{2-q}{2}, \Delta r_\perp^2/2L^2), & \text{if } q = \text{even} \\ 0, & \text{otherwise} \end{cases} \tag{A.6a}$$

$$\int dt\ t^q e^{-t^2/2L^2} = \begin{cases} L^{q+1}\Gamma(\frac{q+1}{2}) 2^{(q+1)/2}, & \text{if } q = \text{even} \\ 0, & \text{otherwise,} \end{cases} \tag{A.6b}$$

where U is Tricomi's confluent hypergeometric function and Γ is the factorial function.

We define

$$\begin{aligned} &\rho^{(1)}(\boldsymbol{r}_1) \equiv \phi_i^*(\boldsymbol{r}_1)\phi_j(\boldsymbol{r}_1), \\ &\rho^{(2)}(\boldsymbol{r}_2) \equiv \phi_k^*(\boldsymbol{r}_2)\phi_l(\boldsymbol{r}_2), \\ &\text{and } V(\boldsymbol{r}_2) = \frac{e}{4\pi\epsilon_0\epsilon_r} \int d\boldsymbol{r}_1 \frac{\rho^{(1)}(\boldsymbol{r}_1)}{|\boldsymbol{r}_1 - \boldsymbol{r}_2|}. \end{aligned} \tag{A.7}$$

A general matrix element then has the form $I = \int dr_2 \rho^{(2)}(r_2) V(r_2)$, where the subscripts ijkl have been dropped for convenience. We integrate out the y terms and apply the forms

defined in Eq. (A.6):

$$\begin{aligned} V(x_2, z_2) &= \int dy_2 V(\boldsymbol{r}_2) \\ &= \frac{e}{4\pi\epsilon_0\epsilon_r} \int d\boldsymbol{r}_1 dy_2 \frac{\rho^{(1)}(\boldsymbol{r}_1)}{|\boldsymbol{r}_1 - \boldsymbol{r}_2|} \\ &= \frac{e}{4\pi\epsilon_0\epsilon_r} \int dx_1 dz_1 \rho^{(1)}(x_1, z_1) \int dy_1 dy_2 \frac{\rho^{(1)}(y_1)\rho^{(2)}(y_2)}{\sqrt{(y_1 - y_2)^2 + \Delta r_\perp^2}} \\ &= \int dx_1 dz_1 \rho^{(1)}(x_1, z_1) f(\Delta r_\perp). \end{aligned} \tag{A.8}$$

The problem is reduced to 2D by replacing the $1/r$ potential with the effective potential, f. Now, the Fourier integral representations of f and ρ are

$$\rho^{(1)}(x_1, z_1) = \int d\boldsymbol{q} e^{2\pi i \boldsymbol{q}\cdot\boldsymbol{r}_{1\perp}} \tilde{\rho}^{(1)}(q_x, q_z) \tag{A.9a}$$

$$f(\Delta r_\perp) = \int d\boldsymbol{k} e^{2\pi i \boldsymbol{k}\cdot(\boldsymbol{r}_{1\perp} - \boldsymbol{r}_{2\perp})} \tilde{f}(k_x, k_z) \tag{A.9b}$$

Using these forms and completing the spatial integrals, V can also be expressed as a Fourier transform:

$$\begin{aligned} V(x_2, z_2) &= \int dx_1 dz_1 \int d\boldsymbol{k} e^{2\pi i \boldsymbol{k}\cdot(\boldsymbol{r}_{1\perp} - \boldsymbol{r}_{2\perp})} \tilde{f}(k_x, k_z) \int d\boldsymbol{q} e^{2\pi i \boldsymbol{q}\cdot\boldsymbol{r}_{1\perp}} \tilde{\rho}^{(1)}(q_x, q_z) \\ &= \int dx_1 dz_1 e^{2\pi i(\boldsymbol{k}+\boldsymbol{q})\cdot\boldsymbol{r}_{1\perp}} \int d\boldsymbol{q} d\boldsymbol{k} \tilde{f}(k_x, k_z) \tilde{\rho}^{(1)}(q_x, q_z) e^{-2\pi i \boldsymbol{k}\cdot\boldsymbol{r}_{2\perp}} \\ &= \int d\boldsymbol{q} d\boldsymbol{k} \delta(q_x + k_x)\delta(q_z + k_z) \tilde{f}(k_x, k_z) \tilde{\rho}^{(1)}(q_x, q_z) e^{-2\pi i \boldsymbol{k}\cdot\boldsymbol{r}_{2\perp}} \\ &= \int d\boldsymbol{k} e^{2\pi i \boldsymbol{k}\cdot\boldsymbol{r}_{2\perp}} \tilde{f}(k_x, k_z) \tilde{\rho}^{(1)}(k_x, k_z) \end{aligned} \tag{A.10}$$

The final integration in Eq. (A.10) is performed using a MATLAB FFT routine. $\tilde{\rho}^{(1)}$ is also

obtained by performing a discrete FFT on $\rho^{(1)}$, which is obtained using the TB method described in the main text. The Fourier transform of f is performed analytically:

$$\tilde{f}(k_x, k_z) = \int_0^{D_c} dr\ r \int_0^{2\pi} d\theta e^{2\pi i k r cos\theta} f(r) = 2\pi \int_0^{D_c} J_0(|2\pi k r|) f(r) r dr. \tag{A.11}$$

Here, D_c is a cutoff distance that prevents the charges from interacting with their periodic images [103]. Since the resulting expression for f is a sum of confluent hypergeometric functions $U(a, b, z)$, one must solved integrals of the form

$$\int_0^{D_c} dr\ r\ J_0(|2\pi k r|)\ U(1/2, b, r^2/2L^2). \tag{A.12}$$

These integrals need to be calculated numerically for each value of k, which turns out to be computationally expensive. However, when D goes to infinity, there is an analytical solution, given by

$$\int_0^{\infty} dr\ r\ J_0(|2\pi k r|)\ U(1/2, 1, r^2/2L^2) = \frac{e^{2\pi^2 k^2 L^2} L\ \mathrm{erfc}(\sqrt{2}\pi k L)}{\sqrt{2}\pi k}, \tag{A.13a}$$

$$\int_0^{\infty} dr\ r\ J_0(|2\pi k r|)\ U(1/2, b, r^2/2L^2) = \frac{L^2}{\sqrt{\pi}} \Gamma(2-b)\ U(2-b, 3/2, 2\pi^2 k^2 L^2),\ b \leq 0 \tag{A.13b}$$

If the integral from D_c to infinity can be calculated efficiently, it can be subtracted from (A.13) to obtain the desired integral (A.12). For large z, the asymptotic form of U is given by

$$U(a, b, z) \sim z^{-a} \sum_{n=0}^{\infty} \frac{(a)_n (a-b+1)_n}{n!} (-z)^{-n}, \tag{A.14}$$

where $(a)_n$ is the Pochhammer symbol, defined as $\frac{\Gamma(a+n)}{\Gamma(a)}$ [164, Eq. 13.7.3]. For each term in the sum, the integral has the following analytical form:

$$\int_{D_c}^{\infty} dr\ r\ J_0(|2\pi kr|)\left(\frac{r^2}{2L^2}\right)^{-\frac{1}{2}-n} = 2^{n+1/2}L^{2n+1}\left(\frac{4^{-n}(2\pi k)^{2n-1}\Gamma(1/2-n)}{\Gamma(1/2+n)} + \frac{D_c^{1-2n}}{2n-1}{}_1F_2(1/2-n;1,3/2-n;-\pi^2 D_c^2 k^2\right), \tag{A.15}$$

where ${}_pF_q$ is the generalized hypergeometric function. We truncate the sum in Eq. A.14 at the $n = 5$ term; for the smallest value of the argument used in this work ($D_c^2/2L^2 = 38.87$) the resulting error is less than 0.2%.

The discrete lattice in the x-z plane has a maximum wave vector. Therefore, it is important to show that the k-space representations of the integrands fall off quickly enough to converge properly. In Fig. A.2, we show that the expression $\tilde{f}(k_x, k_z)\tilde{\rho}^{(1)}(k_x, k_z)$, in the integrand of Eq. (A.10), indeed falls off quickly, for the case of $\hbar\omega = 1.9$ meV in Fig. 2.3(b). We choose to demonstrate a strongly-confined case here, since functions that are more localized in the real space are less localized in k-space. Note that the actual k-space domain is significantly larger than shown in these plots, ensuring the maximum wavevectors set by the discrete lattice are large enough.

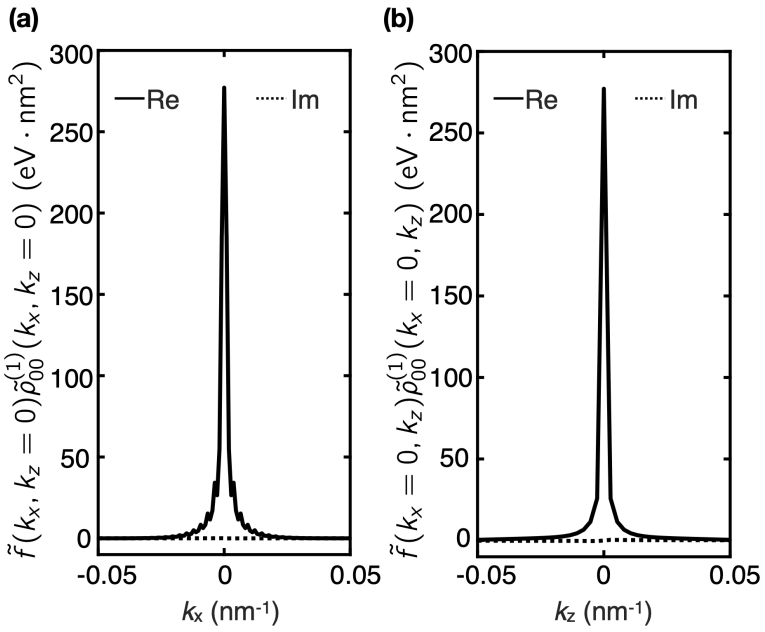

Figure A.2: k-space representation of V in Eq. (A.10). Here, ρ_{00} is the single-electron ground state density for the $\hbar\omega = 1.9$ meV data point in Fig. 2.3(b). Only the central portions of the full domains, with significant amplitudes, are shown. (a) max $|k_x| = 0.18$ nm^{-1}, $|k_z| = 0$, (b) max $|k_z| = 3.68$ nm^{-1}, $|k_x| = 0$.

A.3 Detailed discussion of why the valley singlet-triplet splitting $E_{\mathrm{ST}_{\mathrm{val}}}$ is close to the single-particle valley spitting E_{val} even when interactions are strong

Here, we more explicitly discuss why the one- and two-electron excitation energies E_{val} and $E_{\mathrm{ST}_{\mathrm{val}}}$ are nearly equal, regardless of the confinement strength, in the absence of VOC, as discussed in Sec. 2.3. As mentioned in the main text, this is due to two important observations: (i) the interaction integrals involving electrons with two different valleys are small due to the fast oscillating factors in the wavefunctions, (ii) valley states with the same orbital number have approximately the same envelopes. Therefore, integrals like $(a\ b|a'\ b)$, $(a'\ b|a'\ b)$, $(a\ b'|a'\ b)$ are small, and $(a\ b|c\ d) \approx (a\ b|c'\ d') \approx (a'\ b'|c\ d) \approx (a'\ b'|c'\ d')$. [See Eq. (A.1) for notation definitions.] We demonstrate these two effect numerically in Fig. A.3, where we show results of calculations of a large number of representative matrix elements.

To illustrate further the symmetries and cancellations of the interaction terms in determining the energy separation of S and $\mathrm{T}_{\mathrm{val}}$, we consider an example case motivated by the solutions shown in Fig. 2.3(b-c) and Table E.1. We write

$$\langle \boldsymbol{r}|\mathrm{S}\rangle = \alpha\phi_1\phi_1 + \frac{\beta}{2}\left[\phi_1\phi_4 + \phi_4\phi_1 + \phi_1\phi_6 + \phi_6\phi_1\right] \tag{A.16a}$$

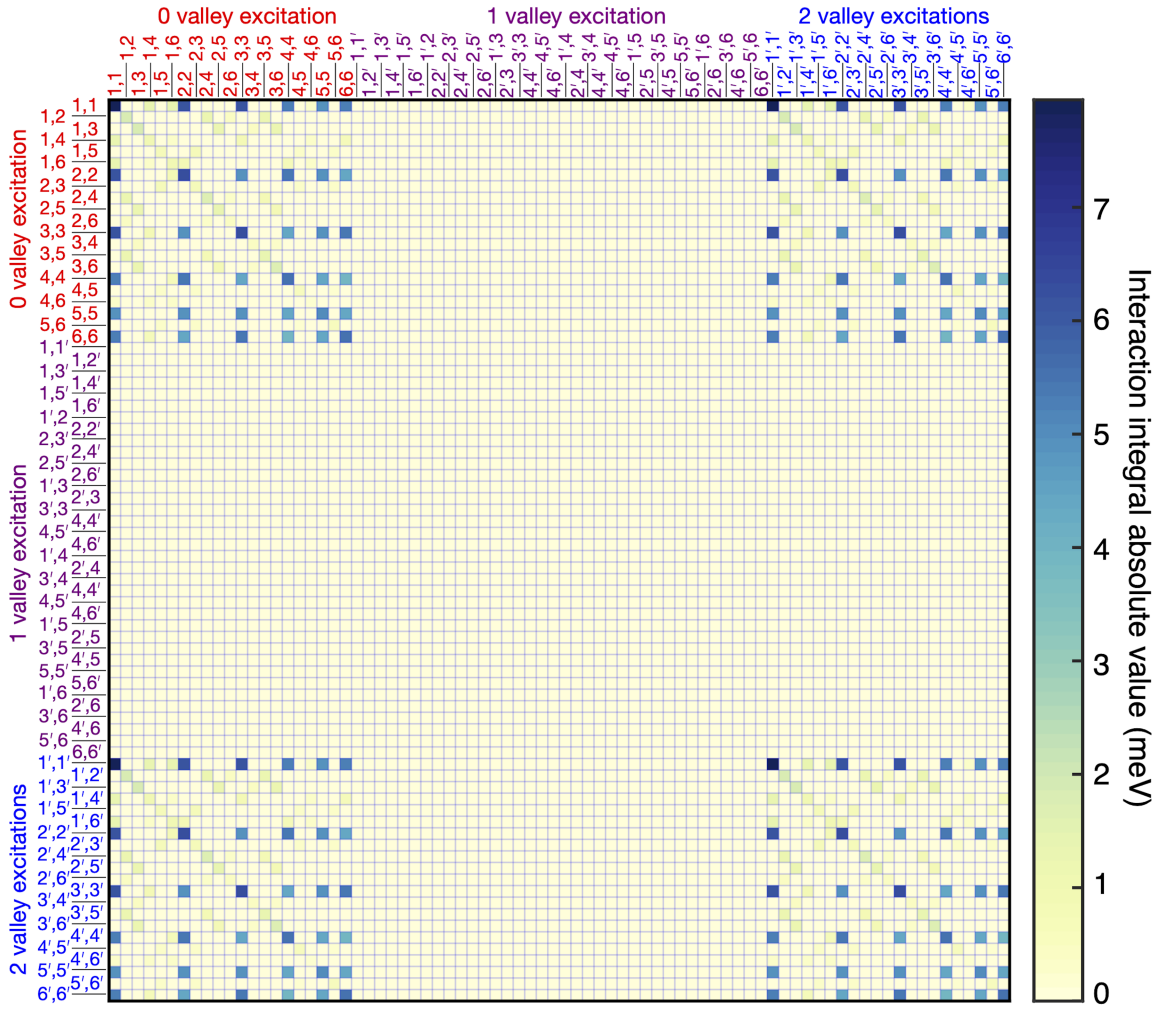

Figure A.3: Spatial interaction integrals involving states in the first three single-electron shells, corresponding to the case $\hbar\omega = 1.2$ meV in Fig. 2.3(b-c).

$$\langle \boldsymbol{r}|\mathrm{T_{val}}\rangle = \frac{\alpha}{\sqrt{2}}\left[\phi_1\phi_{1'} - \phi_{1'}\phi_1\right]$$
$$+ \frac{\beta}{2\sqrt{2}}[(\phi_1\phi_{4'} - \phi_{4'}\phi_1) - (\phi_{1'}\phi_4 - \phi_4\phi_{1'}) + (\phi_1\phi_{6'} - \phi_{6'}\phi_1) - (\phi_{1'}\phi_6 - \phi_6\phi_{1'})], \quad \text{(A.16b)}$$

where $\alpha, \beta > 0$ and ϕ_i are real. Note that we have only included components I and III from Table E.1, for simplicity. The energy difference due to the single-electron part of the Hamiltonian is equal to E_{val}. We now show that the interaction contributions cancel. Using the symmetries $(ij|kl) = (kl|ij) = (ji|kl)$ for real wavefunctions, we have:

$$\langle \mathrm{S}|\, H_{int}\, |\mathrm{S}\rangle = \alpha^2(1\ 1 \mid 1\ 1) + 2\alpha\beta[(1\ 1 \mid 1\ 4) + (1\ 1 \mid 1\ 6)]$$
$$+ \frac{\beta^2}{2}[(1\ 1 \mid 4\ 4) + (1\ 4 \mid 4\ 1) + 2(1\ 1 \mid 4\ 6) + 2(1\ 6 \mid 4\ 1) + (1\ 1 \mid 6\ 6) + (1\ 6 \mid 6\ 1)] \quad \text{(A.17)}$$

$$\langle \mathrm{T_{val}}|\, H_{int}\, |\mathrm{T_{val}}\rangle = \alpha^2[(1\ 1 \mid 1'\ 1') - (1\ 1' \mid 1'\ 1)] + \alpha\beta[(1\ 1 \mid 1'\ 4') - (1\ 4' \mid 1'\ 1) + (1\ 4 \mid 1'\ 1')$$
$$- (1\ 1' \mid 1'\ 4) + (1\ 1 \mid 1'\ 6') - (1\ 6' \mid 1'\ 1) + (1\ 6 \mid 1'\ 1') - (1\ 1' \mid 1'\ 6)] + \frac{\beta^2}{4}[(1\ 1 \mid 4'\ 4')$$
$$- (1\ 4' \mid 4'\ 1) + (1'\ 1' \mid 4\ 4) - (1'\ 4 \mid 4\ 1') + (1\ 1 \mid 6'\ 6') - (1\ 6' \mid 6'\ 1) + (1'\ 1' \mid 6\ 6)$$
$$- (1'\ 6 \mid 6\ 1') + 2(1\ 1 \mid 4'\ 6') - 2(1\ 6' \mid 4'\ 1) + 2(1'\ 1' \mid 4\ 6) - 2(1'\ 6 \mid 4\ 1') + 2(1\ 4 \mid 4'\ 1')$$
$$- 2(1\ 1' \mid 4'\ 4) + 2(1\ 6 \mid 4'\ 1') - 2(1\ 1' \mid 4'\ 6) + 2(1'\ 6' \mid 4\ 1) - 2(1'\ 1 \mid 4\ 6') + 2(1\ 6 \mid 6'\ 1')$$
$$- 2(1\ 1' \mid 6'\ 6)] \quad \text{(A.18)}$$

Further simplifying, based on Fig. A.3 we obtain

$$\begin{aligned}\langle \mathrm{T_{val}}|\, H_{int}\, |\mathrm{T_{val}}\rangle &= \alpha^2(1\ 1 \mid 1'\ 1') + \alpha\beta[(1\ 1 \mid 1'\ 4') + (1\ 4 \mid 1'\ 1') + (1\ 1 \mid 1'\ 6') + (1\ 6 \mid 1'\ 1')] \\ + \frac{\beta^2}{4}[&(1\ 1 \mid 4'\ 4') + (1'\ 1' \mid 4\ 4) + (1\ 1 \mid 6'\ 6') + (1'\ 1' \mid 6\ 6) + 2(1\ 1 \mid 4'\ 6') + 2(1'\ 1' \mid 4\ 6) + 2(1\ 4 \mid 4'\ 1') \\ &+ 2(1\ 6 \mid 4'\ 1') + 2(1'\ 6' \mid 4\ 1) + 2(1\ 6 \mid 6'\ 1')] \\ &= \alpha^2(1\ 1 \mid 1'\ 1') + 2\alpha\beta[(1\ 1 \mid 1'\ 4') + (1\ 1 \mid 1'\ 6')] + \frac{\beta^2}{2}[(1\ 1 \mid 4'\ 4') + (1\ 4 \mid 4'\ 1') \\ &+ 2(1\ 1 \mid 4'\ 6') + 2(1\ 6 \mid 4'\ 1') + (1\ 1 \mid 6'\ 6') + (1\ 6 \mid 6'\ 1')] \quad \text{(A.19)}\end{aligned}$$

Comparing Eqs. (A.17)and(A.19), we conclude that the interaction energies indeed cancel and, therefore, $E_{\mathrm{ST_{val}}} \approx E_{\mathrm{val}}$.

We now provide analytical estimates to back up these numerical observations. In particular, we compare $(1\ 1 \mid 1\ 1)$ and $(1\ 1' \mid 1\ 1')$ to show that the latter is much smaller than the former. Using the envelope function formalism [36], with Gaussian envelopes for simplicity, we have

$$\phi_1 = \frac{e^{-(x^2+y^2)/2L^2}}{(\pi L^2)^{1/2}} \frac{e^{-z^2/2l^2}}{(\pi l^2)^{1/4}} \sqrt{2} \sin k_0 z,\ \ \phi_{1'} = \frac{e^{-(x^2+y^2)/2L^2}}{(\pi L^2)^{1/2}} \frac{e^{-z^2/2l^2}}{(\pi l^2)^{1/4}} \sqrt{2} \cos k_0 z. \quad \text{(A.20)}$$

Therefore,

$$\begin{aligned}(1\ 1 \mid 1\ 1) = \frac{e^2}{4\pi\epsilon_0\epsilon_r} \int \frac{dz_1 dz_2}{\pi l^2} e^{-(z_1^2+z_2^2)/l^2} \sin^2 k_0 z_1 \sin^2 k_0 z_2 \\ \times \int \frac{dx_1 dy_1 dx_2 dy_2}{\pi^2 L^4} \frac{e^{-(x_1^2+y_1^2+x_2^2+y_2^2)/L^2}}{((x_1-x_2)^2+(y_1-y_2)^2+(z_1-z_2)^2)^{1/2}} \quad \text{(A.21)}\end{aligned}$$

The second integral can be calculated using the change of variables $s_x = x_1 + x_2$, $s_y = y_1 + y_2$, $t_x = x_1 - x_2$, and $t_y = y_1 - y_2$, giving

$$\frac{1}{4\pi^2 L^4} \int dt_x dt_y e^{-(t_x^2+t_y^2)/2L^2} \int ds_x ds_y \frac{e^{-(s_x^2+s_y^2)/2L^2}}{(s_x^2 + s_y^2 + (z_1 - z_2)^2)^{1/2}} = \frac{\sqrt{\pi}}{\sqrt{2}L} e^{(z_1-z_2)^2/2L^2} (1 - \mathrm{erf}(|z_1 - z_2|/\sqrt{2}L)) \quad \text{(A.22)}$$

Applying an additional change of variables, $s = z_1 + z_2$ and $t = z_1 - z_2$, we obtain

$$\frac{e^2}{4\pi\epsilon_0\epsilon_r} \frac{1}{8\sqrt{2\pi}l^2 L} \int ds\ dt\ e^{-s^2/2l^2} e^{-t^2(L^2-l^2)/2L^2l^2} \left(\cos(k_0 t) - \cos(k_0 s)\right)^2 (1 - \mathrm{erf}(|t|/\sqrt{2}L)). \quad \text{(A.23)}$$

The following integrals are used to evaluate Eq. (A.23):

$$\int du\ e^{-\kappa u^2} = \sqrt{\frac{\pi}{\kappa}},\ \kappa > 0 \quad \text{(A.24a)}$$

$$\int du\ e^{-\kappa u^2} \cos(k_0 u) = \sqrt{\frac{\pi}{\kappa}} e^{-k_0^2/4\kappa},\ \kappa > 0 \quad \text{(A.24b)}$$

$$\int du\ e^{-\kappa u^2} \cos^2(k_0 u) = \frac{(e^{-k_0^2/\kappa} + 1)\sqrt{\pi}}{2\sqrt{\kappa}},\ \kappa > 0 \quad \text{(A.24c)}$$

$$\int du\ e^{-\kappa u^2} \mathrm{erf}(\tau|\mathrm{u}|) = 2\arctan(\tau/\sqrt{\kappa})/\sqrt{\pi\kappa},\ \kappa > 0,\ \tau > 0 \quad \text{(A.24d)}$$

$$\int du\ e^{-\kappa u^2} \cos^2(k_0 u)\ \mathrm{erf}(\tau|\mathrm{u}|) = \int_0^\infty du\ e^{-\kappa u^2} \cos(2k_0 u)\ \mathrm{erf}(\tau \mathrm{u}) + \int_0^\infty du\ e^{-\kappa u^2}\ \mathrm{erf}(\tau \mathrm{u}),\ \kappa > 0,\ \tau > 0. \quad \text{(A.24e)}$$

Here, the terms with factors $e^{-k_0^2/4\kappa}$ and $e^{-k_0^2/\kappa}$ are negligible. To calculate the first term on the right-hand side of Eq. (A.24e), we use integration by parts:

$$\begin{aligned}
&\int_0^\infty du\ e^{-\kappa u^2} \cos(2k_0 u)\ \mathrm{erf}(\tau \mathrm{u}) \\
&= \frac{e^{-\kappa u^2}\ \mathrm{erf}(\tau u)\sin(2k_0 u)}{2k_0}\bigg|_0^\infty - \frac{1}{2k_0}\int_0^\infty du\ \sin(2k_0 u)\left(\frac{2\tau}{\sqrt{\pi}} e^{-(\kappa+\tau^2)u^2} - 2\kappa u\ \mathrm{erf}(\tau u\right) \\
&= 0 - \frac{\tau\ F(k_0/\sqrt{\kappa+\tau^2})}{k_0\sqrt{\pi(\kappa+\tau^2)}} + \frac{\kappa}{k_0}\int_0^\infty du\ \sin(2k_0 u) u\ \mathrm{erf}(\tau u), \quad \text{(A.25)}
\end{aligned}$$

where F is the Dawson function. We can also use integration by parts to evaluate the remaining integral in Eq. (A.25), which would yield terms proportional to the higher orders of $1/k_0$. These terms are also negligible. Combining everything, we obtain

$$(1\ 1 \mid 1\ 1) \approx \frac{e^2}{4\pi\epsilon_0\epsilon_r\sqrt{2\pi(L^2-l^2)}}\left(\pi + \frac{\sqrt{L^2-l^2}F(2k_0 l)}{\sqrt{2}k_0 L^2} - 2\arctan\left(\frac{l}{\sqrt{L^2-l^2}}\right)\right). \quad \text{(A.26)}$$

Similarly, $(1\ 1' \mid 1\ 1')$ can be calculated by replacing $(\cos(k_0 t) - \cos(k_0 s))^2$ term in Eq. (A.23) by $(\cos(2k_0 t) - \cos(2k_0 s))/2$. The only term that does not have an exponential suppression in this integral is a product of the integrals shown in Eqs. (A.24a) and(A.25),

Table A.1: Values of some interaction integrals.

l (nm)	L (nm)	$\hbar\omega_z$ (meV)	$\hbar\omega_{xy}$ (meV)	[Analytical: (1 1 | 1 1) (meV)]	Eqs. (A.26-A.27)] (1 1′ | 1 1′) (μeV)	[Numerical: (1 1 | 1 1) (meV)]	Appendix A.1] (1 1′ | 1 1′) (μeV)
2.69	30.00	11.50	0.45	5.0	0.1	5.0	0.1
2.69	25.00	11.50	0.64	5.9	0.1	5.9	0.1
2.69	18.28	11.50	1.2	7.9	0.2	7.9	0.2
2.00	10.00	20.80	4.0	14.1	0.7	14.1	0.7
1.00	3.00	83.19	44.56	43.9	15.6	43.9	15.9
0.60	1.60	231.08	156.66	80.7	91.8	80.9	97.3

yielding

$$(1\ 1' \mid 1\ 1') \approx \frac{e^2}{4\pi\epsilon_0\epsilon_r\sqrt{2\pi(L^2-l^2)}}\frac{\sqrt{L^2-l^2}F(2k_0l)}{\sqrt{2}k_0L^2}. \tag{A.27}$$

Some values of the integrals obtained using Eqs. (A.26) and (A.27), along with the values obtained by using the numerical method summarized in Appendix A.1, for the wavefunction forms in Eq. (A.20), are shown in Table A.1. We find that (1 1 | 1 1) is indeed much larger than (1 1′ | 1 1′), and there is good agreement between the analytical and numerical methods. We finally note that the values in the third row of Table A.1 best correspond to the values in Fig. A.3. Here, we chose the l value to yield a similar inverse participation ratio in z as in Fig. A.3, in which (1 1 | 1 1) = 7.9 meV and (1 1′ | 1 1′) = 0.2 μeV.

A.4 Additional details regarding Fig. 2.5

In Fig. A.4(a), we show the ground state electron densities, as a function of x, for the data in Fig. 2.5. Here, the blue lines denote the positions of the atomic steps at the interface. Figure A.4(b) shows the corresponding E_{ST} and E_{val} values, together with the interface profiles considered.

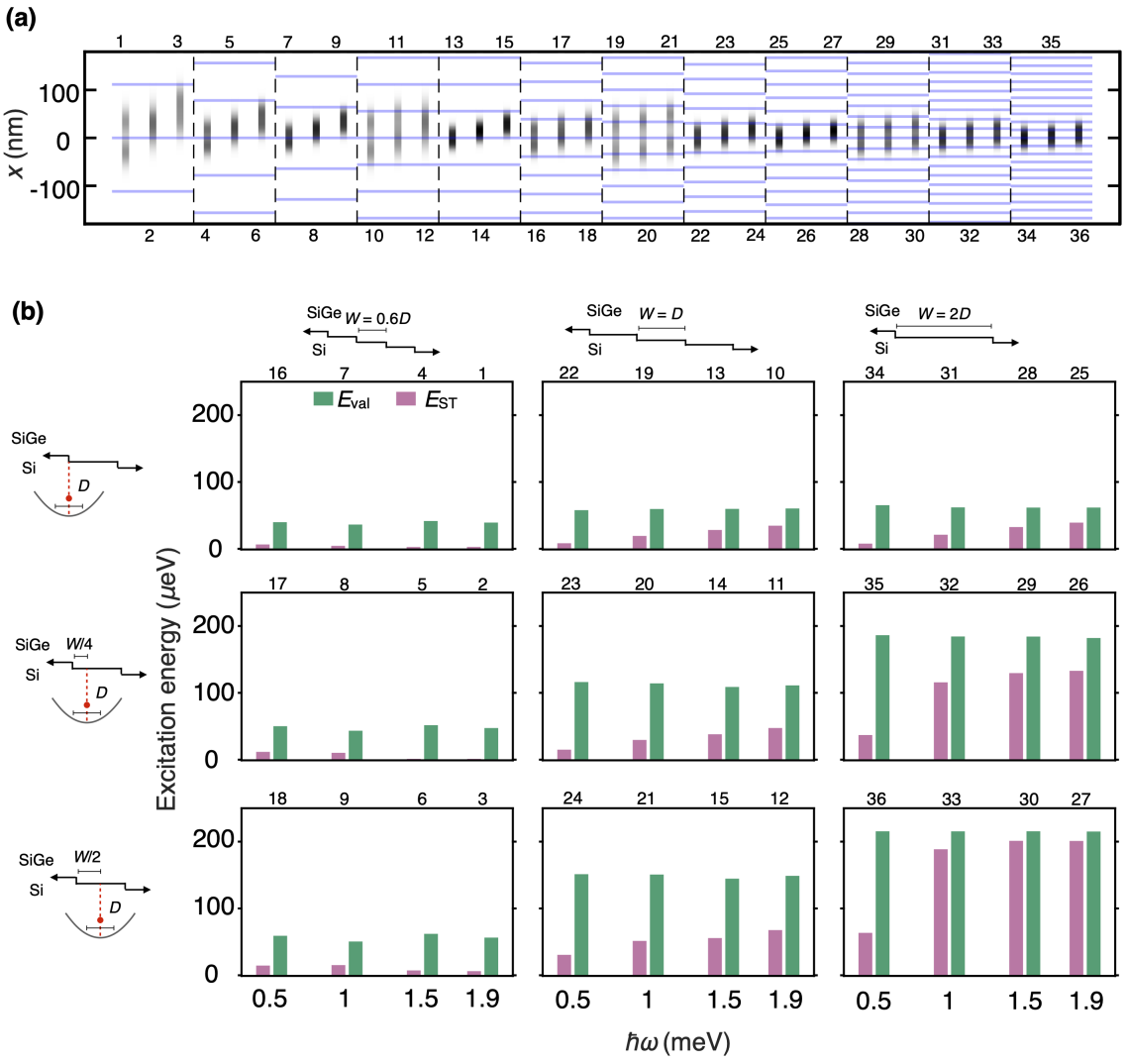

Figure A.4: Full set of solutions reported in Fig. 2.5. (a) One-dimensional electron densities of the ground states, corresponding to 36 cases in Fig. 2.5. Blue lines show the steps at the interface. (b) E_{ST} (pink) in comparison to E_{val} (cyan) in circular dots defined in 10 nm wide quantum wells, with an electric field of 1.5 MV/m and tilted interfaces. The columns show the horizontal distance between steps (the step widths, W), corresponding to $0.6D$, D and $2D$, where $D = 2\sqrt{\hbar/m_t\omega}$ is the dot diameter. The rows show distance to the nearest step, d, corresponding to 0, $0.25W$ and $0.5W$.

A.5 FCI convergence

This appendix reports the convergence properties of the FCI calculations. In Figs. A.5(a) and A.5(b), we plot the energy eigenvalues of the most-weakly-confined circular dots, as a function of the number of shells included in the single-electron basis set. Due to the two-fold multiplicity of the valleys, n shells correspond to $K = n(n+1)$ states, excluding spin. In the circular dot calculations we used 6 shells, as this number is observed to be sufficient for convergence in the most challenging cases. In Fig. A.5(c), we plot the energy eigenvalues of the most-weakly-confined elliptical dots as a function of the number single-electron states included basis, as there is no well-defined shell structure appropriate for all cases in Fig. 2.6. We used $K = 40$ in these calculations.

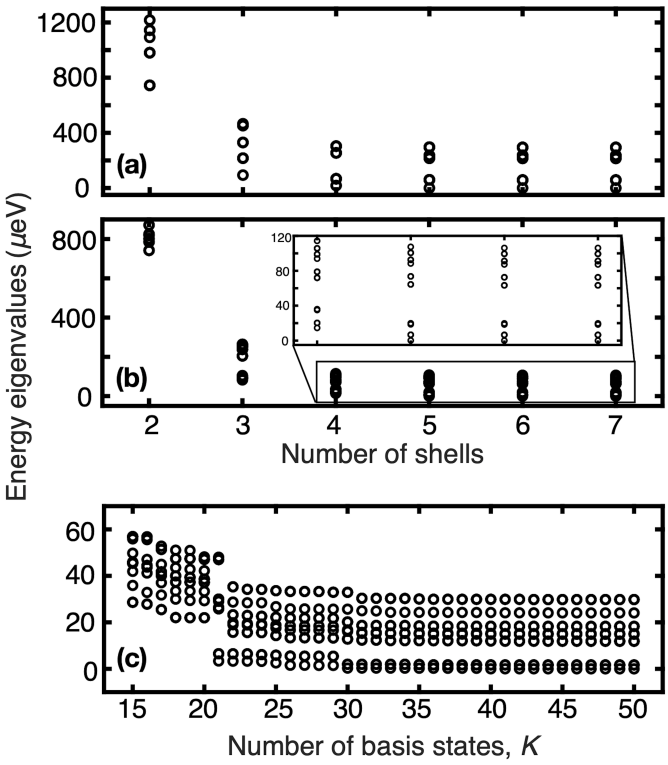

Figure A.5: Convergence properties of the FCI calculations. Data correspond to (a) the case with $\hbar\omega = 0.4$ meV, in Fig. 2.3(b), (b) the case with $\hbar\omega = 0.5$ meV, $W = 0.6D$, and $d = 0$ in Fig. A.4, and (c) the case with $\hbar\omega_y = 0.8\hbar\omega_x = 0.24$ meV in Fig. 2.6(b). Results for (a),(b) the lowest 20, or (c) the lowest 16 levels (including degeneracies), with respect to the ground state, calculated using up to (a),(b) 7 shells ($K = 56$), or (c) 50 single-electron basis states.

Appendix B

Supplemental information for Chapter 3

B.1 Singlet-triplet splitting for high valley-orbit coupling cases

The main text shows the results of calculations performed in the regime where the valley-orbit coupling induced by steps at the quantum well interface is small enough that the singlet-triplet splitting is near 100 μeV, large enough for quantum computing applications. The insets of Fig. E.4(a) show results obtained when the dot is maximally offset from the atomic steps at the quantum well interface. Here we examine the behavior when the valley-orbit coupling is larger, by characterizing the valley and orbital singlet-triplet energy splittings when the dot center is closer to the nearest interface step.

Fig. B.1(a-b) shows the singlet-triplet splittings as well as the single-particle valley splitting as a function of W/D for electrons in a dot centered on an interface step. The two values of $\hbar\omega$ shown are on the either side of the transition in Fig. E.4(a) in the main text. It is clear that changing the location of the dot center with respect to the interface step changes the behavior of the ST splitting qualitatively. When the dot is centered on an interface step, valley-orbit coupling suppresses single-particle valley splitting substantially, and moreover, e-e interaction effects suppress the valley ST splitting substantially from the single-particle valley splitting.

Fig. B.2 shows the singlet-triplet splittings as well as the valley splitting as a function of the distance to the nearest step for a fixed confinement at $\hbar\omega = 700$ μeV and step separation $W = 3.5D$ of the uniformly distributed interface steps. Here, it is possible to observe the effect of disorder-induced valley-orbit coupling gradually, as the dot gets closer to the nearest step. As the valley splitting is a property of the lowest single-electron orbital and the singlet-triplet splitting is a property of interacting two-electron states that involve higher orbitals, the effect of the step on the singlet-triplet splitting is observed at a larger distance from the step than on the valley splitting.

The results in this section demonstrate that a large and robust ST splitting requires, in general, that the dot center should not be near a step, both due to the suppression of the valley splitting and due to the further suppression of the singlet-triplet splitting from the valley splitting. We note that, however, the latter suppression does not necessarily monotonically increase as the dot gets closer to a step, as indicated in the inset of Fig.

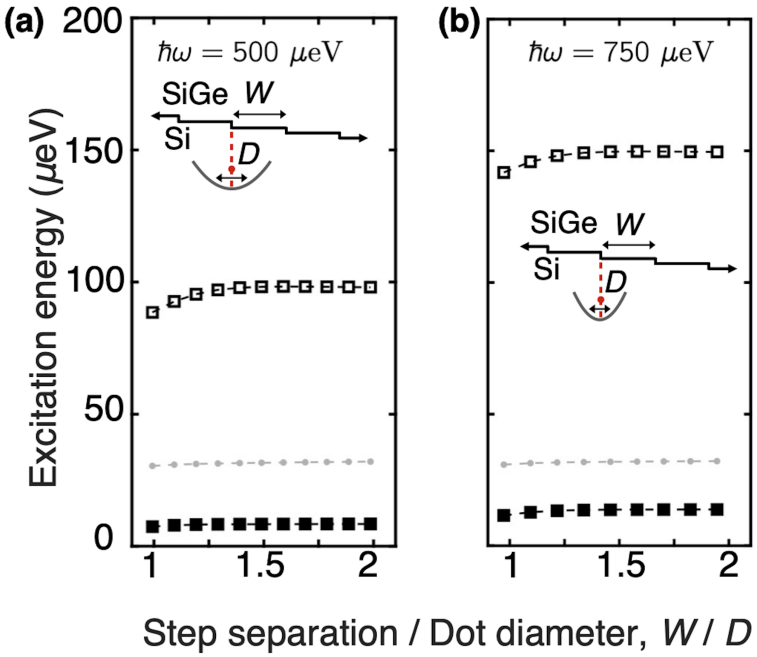

Figure B.1: Singlet-triplet splitting when the valley-orbit coupling is high because the dot center is directly over a step. In these plots, the step separation W is increased while the confinement energy is held fixed (therefore D), and the center of the confinement potential is directly over an interface step ($d = 0$). The valley singlet-triplet splitting is smaller than the orbital singlet-triplet splitting over the entire range shown, so the open squares show the orbital ST splitting, the solid squares show the valley singlet-triplet splitting, and the dashed line shows the single-particle valley excitation energy. The large valley-orbit coupling suppresses the single-particle valley excitation energy substantially below its value in the absence of a step of 100 μeV, and in addition, e-e interactions suppress the valley singlet-triplet splitting substantially below the single-particle valley splitting.

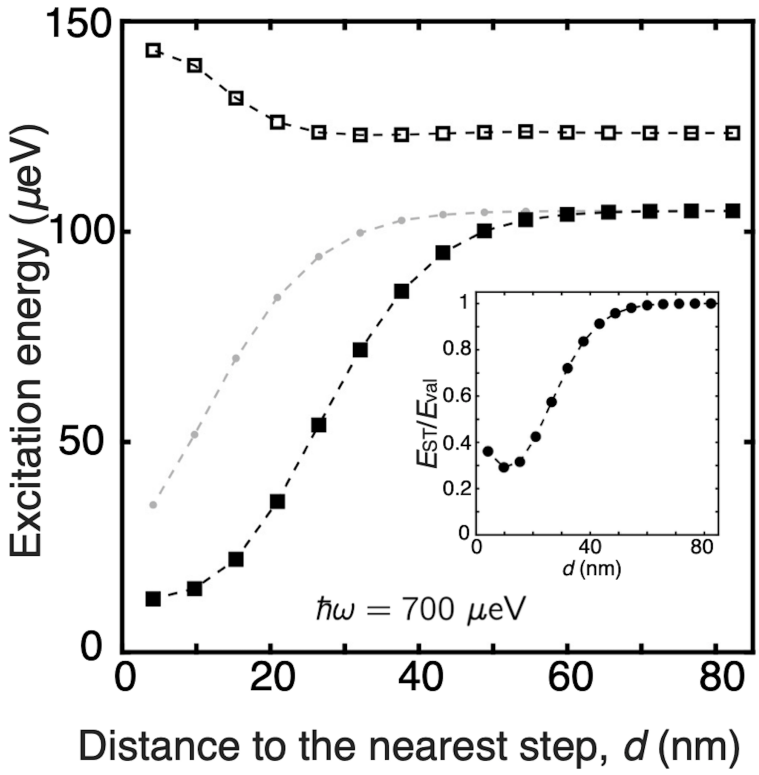

Figure B.2: Characterization of singlet-triplet splitting as the distance between the dot center and interface step is varied. In these plots, the ratio between the step separation and dot diameter W/D is held fixed, $W/D = 3.5$, and the confinement energy is held fixed, $\hbar\omega = 700$ μeV. The valley singlet-triplet splitting (solid squares) is smaller than the orbital singlet-triplet splitting (open squares) over the entire range shown. As the dot gets closer to the nearest step, the valley singlet-triplet splitting starts to drop before the valley splitting (gray dots). Inset shows the ratio of the valley ST splitting to the valley splitting.

B.2, which is also a result of interacting two-electron states involving higher orbitals, and therefore various valley-orbital energy splittings.

Appendix C

Supplemental information for Chapter 4

C.1 Pulsed-gate spectroscopy model

Consider a dot tunnel coupled to a reservoir, illustrated in Fig. C.1(a). The dot is pulsed in a two-step duty cycle between voltages V_L and V_U, as shown in Fig. C.1(b). The corresponding chemical potentials of the ground states of the dot, E_{Lg} and E_{Ug}, are related to V_L and V_U via a lever arm: $E_{\nu g} = \alpha V_\nu + E_0$, where $\nu = U, L$ and E_0 is the ground state (g) of the dot in the absence of a pulse. If the dot also has an excited state (x), then $\Delta E \equiv E_{Ux} - E_{Ug} = E_{Lx} - E_{Lg}$, and $E_{\nu x} = E_{\nu g} + \Delta E$. Tunneling can occur if there is a state in the reservoir that electrons can tunnel out of or into, as determined by the Fermi

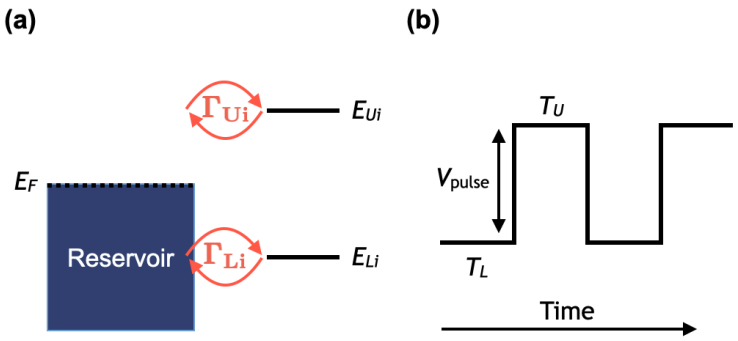

Figure C.1: Parameters definitions for pulse spectroscopy. (a) E_F is the Fermi energy of the reservoir. E_{Ui} is the chemical potential of the dot eigenstate state i at the top edge of the pulse. Here, i can refer to the ground state (g), the first excited state (x_1), etc. E_{bi} is the chemical potential of the dot eigenstate i at the bottom edge of the pulse. Γ_{Ui} and Γ_{Li} are the corresponding tunnel couplings. (b) The duty cycle for the pulse applied to gate P2. $T_L = T_U$ for valley-orbit measurements. The pulse frequency $f_{\text{pulse}} = 1/(T_L + T_U)$ is on the order of the tunnel rate into/out of the dot during the bottom part of the pulse cycle. The tunnel rate out of the dot during the top part of the pulse is much faster than the pulse frequency such that the dot is completely empty at the beginning of the bottom part of the pulse.

function:

$$f_{\nu i} = \left[e^{(E_{\nu i} - E_F)/k_B T} + 1\right]^{-1}, \tag{C.1}$$

where $i = g, x$.

The tunnel rates, $\Gamma_{\nu i}$, depend on the chemical potential $E_{\nu i}$, and can differ for the different dot eigenstates ($\nu = g, x$). As discussed in Ref. [144], $\Gamma_{\nu i}$ is a complicated exponential function. However, since there is not enough structure in the data to fully characterize the

features of $\Gamma_{\nu i}$, we can simply linearize this function about the Fermi level, obtaining

$$\Gamma_{\nu g} \simeq \Gamma_{0,\nu g} e^{(E_{\nu g} - E_F)/E_{0,\nu g}}, \tag{C.2}$$

$$\Gamma_{\nu x} \simeq \Gamma_{0,\nu x} e^{(E_{\nu g} + \Delta E - E_F)/E_{0,\nu x}}. \tag{C.3}$$

While there also exists a decay rate from the excited state to the ground state, Γ_{xg}, here we do not consider its effect since recent measurements [165] indicate the decay rate is much slower than our pulse frequency $f_{\text{pulse}} \simeq 1$ MHz.

For a single ground state in the quantum dot, the rate equation for its level filling n_g is derived using detailed balance:

$$\dot{n}_{\nu g} = \Gamma_{\nu g}(f_{\nu g} - n_g) \tag{C.4}$$

Before solving Eqn. C.4, we note that the steady state filling of the ground state, n_g, can be computed by setting $\dot{n}_g = 0$. The steady state filling is then simply the Fermi function, $n_g = f_g$. However, this is only valid in the limit that $\Gamma_{\nu g} \gg f_{\text{pulse}}$. The measurements shown in the main text tune the tunnel rates such that, $\Gamma \simeq f_{\text{pulse}}$, giving high sensitivity for pulsed gate spectroscopy measurements [148]. Thus, we must find the general solution to Eqn. C.4 for $t > t_0$:

$$n_{\nu g}(t) = f_{\nu g} - f_{\nu g}\left(1 - \frac{n_{\nu g}(t_0)}{f_{\nu g}}\right) e^{-\Gamma_{\nu g}(t - t_0)} \tag{C.5}$$

where $n_{\nu g}(t_0)$ is the occupation of the dot at $t = t_0$. Since αV_{pulse} is much larger than the

singlet-triplet splitting (E_{ST}) and valley splitting (E_{val}), $\Gamma_{Ug} \gg f_{\mathrm{pulse}}$ in the fit regime [166]. Thus, when fitting our data, it is assumed that the dot is completely empty at the beginning of the bottom part of the duty cycle. Then $n_{Lg}(t_0) = 0$ and Eqn. C.4 simplifies to

$$n_{Lg}(t) = f_{Lg}\left(1 - e^{-\Gamma_{Lg}(t-t_0)}\right) \tag{C.6}$$

The average electron occupation of the ground state of the dot during the entire pulse cycle is found by integrating from $t = t_0$ to $t = t_0 + T_L$ and dividing by $1/(T_U + T_L)$, where it has been assumed the average electron occupation of the dot during the top part of the duty cycle is 0 and $T_U = T_L$. Integrating Eqn. C.6, we obtain

$$\langle n_g|n_g\rangle = \frac{1}{2}f_{Lg} + \frac{1}{2T_L}\frac{f_{Lg}}{\Gamma_{Lg}}\left(e^{-\Gamma_{Lg}T_L} - 1\right) \tag{C.7}$$

where the first term on the right hand side of Eqn. C.7 represents the steady state occupation of the dot during the bottom part of the pulse, and the second term represents the perturbation due to energy dependent tunneling [144]. Finally, assuming that $\langle n_L|n_L\rangle = \langle n_{Lg}|n_{Lg}\rangle + \langle n_{Lx}|n_{Lx}\rangle$, the average electron occupation for the ground and excited states in the dot during the bottom part of the pulse is

$$\langle n|n\rangle = \frac{1}{2}\sum_{i=g,x}\left[f_{Li} + \frac{1}{T_L}\frac{f_{Li}}{\Gamma_{Li}}\left(e^{-\Gamma_{Li}T_L} - 1\right)\right] \tag{C.8}$$

This form can be simplified further into a convenient fitting form by expanding the exponential in Eqn. C.8. This is valid for our measurements since $\Gamma \sim f_{\mathrm{pulse}}$ and $T_L = 1/(2f_{\mathrm{pulse}})$,

making $\Gamma_{Li}T_L < 1$. Expanding to second order, we obtain the final fitting form for determining valley-orbit state splittings using pulsed-gate spectroscopy

$$\langle n|n\rangle = \sum_{i=g,x} \Gamma_i \frac{e^{(E_i - E_F)/E_{0i}}}{e^{(E_i - E_F)/k_B T_e} + 1} \tag{C.9}$$

where $E_i = \alpha V_i$ is the position of each peak in energy, and E_{0i} and Γ_i are fitting parameters for each peak.

C.2 Magnetospectroscopy model

Magnetospectroscopy was used in addition to pulsed-gate spectroscopy to supplement measurements of E_{ST}, providing better precision at low valley-orbit splittings and quantitative verification of pulsed-gate valley-orbit splitting measurements. In this section, a model is developed that can be used to extract E_{ST} from magnetospectroscopy data sets, where the plunger gate voltage is swept on one axis and the magnetic field is swept on the other. This 2-dimensional data set is then converted into a 1-dimensional data set by peak-fitting along the voltage axis, where the differential conductance is fit using the derivative of of Eqn. 2 in Ref. [150] with respect to gate voltage. The peak-fitted data set is then curve fit using Eqn. C.19, which we now derive.

Consider a quantum dot that is tuned electrostatically such that the one- and two-electron charge states are nearly degenerate. The system is found to be in one of six spin states that is dependent on the number of electrons in the quantum dot. For one electron, it is found

to be in the $|\uparrow\rangle$ or $|\downarrow\rangle$ spin-state. For two-electrons, it is found to be in one of the singlet ($|S_0\rangle$) or triplet ($|T_-\rangle, |T_0\rangle, |T_+\rangle$) spin-states. Including charge and spin degrees of freedom and excluding charging energy, the energy of each state is given by [167, 168]:

$$E_\downarrow = -\frac{1}{2}g\mu_B B - \alpha V_{\mathrm{P2}} \tag{C.10}$$

$$E_\uparrow = \frac{1}{2}g\mu_B B - \alpha V_{\mathrm{P2}} \tag{C.11}$$

$$E_{S_0} = -2\alpha V_{\mathrm{P2}} \tag{C.12}$$

$$E_{T_-} = -g\mu_B B - 2\alpha V_{\mathrm{P2}} + E_{\mathrm{ST}} \tag{C.13}$$

$$E_{T_0} = -2\alpha V_{\mathrm{P2}} + E_{\mathrm{ST}} \tag{C.14}$$

$$E_{T_+} = g\mu_B B - 2\alpha V_{\mathrm{P2}} + E_{\mathrm{ST}} \tag{C.15}$$

where $g = 1.99$ is the electron g-factor in silicon, μ_B is the Bohr magneton, α is the gate lever arm, and V_{P2} is the gate voltage.

Using standard lock-in detection techniques, detailed in Ref. [169], the derivative of the average electron occupation of the dot with respect to gate voltage is measured, shown in Fig. E.3(e) of the main text. A derivation for the average electron occupation of a system in thermal and diffusive contact with a large reservoir is detailed in Ref. [170]. The total electron

occupation $\langle n|n\rangle$ is determined by treating the system as a grand canonical ensemble:

$$\langle n|n\rangle = \frac{1}{\mathcal{Z}} \sum_i N_i e^{(N\mu - E_i)/k_B T_e} \tag{C.16}$$

$$\mathcal{Z} = \sum_i e^{(N_i\mu - E_i)/k_B T_e} \tag{C.17}$$

where $\mathcal{Z}$ is the grand partition function, μ is the chemical potential of the reservoir, T_e is the electron temperature and N_i is the number of electrons on the dot for each given state (two electrons for the $|S_0\rangle$ and $|T\rangle$ states, and one electron for $|\uparrow\rangle$ and $|\downarrow\rangle$ states).

A 4-state model (inclusion of states $|\downarrow\rangle, |\uparrow\rangle, |S_0\rangle, |T_-\rangle$) may be sufficient in the limit of low T_e and high E_{ST}; however, we find that in the experimentally relevant range ($T_e \simeq 100$ mk, $E_{\mathrm{ST}} = 25$–60 μeV), the 6-state model is requisite since significant occupation of higher lying states at $B = 0$ occurs. We do not attempt to quantitatively match the raw voltage V_{P2}, instead plotting δV_{P2}. This simplifies the final result (Eqn. C.16), allowing $\mu = 0$ as this quantity only provides an offset in V_{P2}. Additionally, this justifies excluding the charging energy from the states at the beginning of the derivation. The average electron occupation is then

$$\langle n|n\rangle = 1 + \frac{e^{\alpha\beta_e V_{\mathrm{P2}}}\left(1 + e^{\kappa B}\left(1 + e^{E_{\mathrm{ST}}\beta_e} + e^{\kappa B}\right)\right)}{e^{\alpha\beta_e V_{\mathrm{P2}}} + e^{(\alpha V_{\mathrm{P2}} + E_{\mathrm{ST}})\beta_e + \kappa B} + e^{E_{\mathrm{ST}}\beta_e + \frac{1}{2}\kappa B} + e^{\alpha\beta_e V_{\mathrm{P2}} + \kappa B} + e^{E_{\mathrm{ST}}\beta_e + \frac{3}{2}\kappa B} + e^{\alpha\beta_e V_{\mathrm{P2}} + 2\kappa B}} \tag{C.18}$$

where we have introduced $\beta_e = 1/k_B T_e$ and $\kappa = g\mu_B\beta_e$. The derivative of Eqn. C.18 with respect to gate voltage is plotted in Fig. E.3(f) of the main text.

When fitting for E_{ST}, the peak value position along the gate voltage axis (V_{P2}) is extracted as described above (ie: Fig. E.3(g) of the main text). The curve fit is obtained from C.18 by solving the equation $d^2 \langle n|n\rangle / dV_{\mathrm{P2}}^2 = 0$. The resulting curve fit as a function of magnetic field is

$$V_{P2}(B) = \frac{1}{\alpha\beta} \ln\left(\frac{e^{\frac{1}{2}\kappa B + \beta_e E_{\mathrm{ST}}} \left(e^{\kappa B} + 1\right)}{e^{\kappa B} + e^{2\kappa B} + e^{\kappa B + \beta_e E_{\mathrm{ST}}} + 1} \right), \tag{C.19}$$

C.3 COMSOL electrostatic simulations

The COMSOL Multiphysics simulations are full device simulations where the dimensions for each gate electrode are modeled out to 500 nm away from the center of the device. Using a realistic quasiclassical (Thomas-Fermi) electrostatic simulation [171, 172], the electron density is calculated as a function of gate voltages. The simulation is used to gain intuition and provide estimates for quantum dot shape and position as the electrostatic configuration is varied across the experimental range.

The presence of offset charge is incorporated into the simulation by first calculating the electron density with the measured device voltages with no offset charge. Offset charge is then added using a constant gate voltage offset to all gates until the electron density beneath the reservoirs plateaus. This is the theoretical analog to the experimental device

tuning procedure used, where reservoir voltages are increased until a plateau in transport is observed. Then, while fixing S3 to 370 mV plus the original offset, a new offset to all other gates is applied until the integrated charge in the quantum dot beneath P2 is roughly one electron. This procedure preserves the differential voltage between each gate as closely as possible.

The final step in simulating the experimental range of electrostatic tunings is adjusting V_{S3} and the gates neighboring the P2 quantum dot to closely approximate the gate voltage changes made in the experiment. The gate lever arms (α) are determined for each gate in the COMSOL simulation, and are found to be in close agreement (but not identical) to the experiment. Table C.1 shows the experimentally measured α for each gate neighboring the P2 quantum dot. To keep the P2 quantum dot electron occupation close to 1.0 throughout the different electrostatic regimes, COMSOL offset voltages were determined using the ratio of experimental to COMSOL gate lever arm values as $\Delta V_{\mathrm{sim}} = \alpha_{\mathrm{exp}}/\alpha_{\mathrm{sim}}\Delta V_{\mathrm{exp}}$. By applying offsets in this way, the differential gate voltage used in the experiment is preserved without significantly changing the electron occupation of the simulated dot.

The COMSOL simulated orbital splittings and change in position of the quantum dot qualitatively match the experimental results, giving insight into the physical behavior of the device across the electrostatic configurations. Both the simulation and measurements indicate $\hbar\omega_x < \hbar\omega_y$ at low S3 gate voltages, and $\hbar\omega_x > \hbar\omega_y$ at large S3 gate voltages. Between the S3 voltages of 330–370 mV, the dot is found to be roughly isotropic in the simulation. As noted in the main text, voltages of $V_{\mathrm{S3}} > 390$ mV did not produce physical

Table C.1: Measurements of α for gates S3, S2, P2, B2 and B3 at varying electrostatic configurations (denoted by the S3 gate voltage value). In addition to the changing S3 gate voltage, a compensating voltage to neighboring plunger and barrier gates was applied to maintain the electron occupation of the P2 dot. The change in α values clearly shows the dot moving away from S2 towards S3 as the S3 gate voltage changes from 260 mV to 420 mV. This exact behavior observed in the COMSOL simulations.

S3 (mV)	α_{S3}	α_{S2}	α_{P2}	α_{B2}	α_{B3}
260	0.231	0.263	0.209	0.063	0.098
330	0.226	0.213	0.207	0.064	0.089
370	0.230	0.179	0.198	0.061	0.079
420	0.277	0.134	0.189	0.064	0.075

results in the simulation due to electron accumulation directly beneath the S3 screening gate. This same phenomenon occurred at 430 mV in the experiment. The discrepancy is most likely due to a small difference is α_{S3} between the simulation and experiment since the α of each gate varies across the electrostatic tunings, as shown in Table C.1.

C.4 TB and FCI methods

Full configuration interaction (FCI) simulations aided by tight-binding (TB) calculations of the electronic wave functions are used to accurately model E_{val} and E_{ST}, as shown in Fig. E.4 of the main text. The TB model calculations results in wave functions with fast oscillations in the z-direction which breaks the valley degeneracy. Thus, effects on the valley splitting due to atomistic disorder, and the disorder-induced valley-orbit coupling are captured in the TB model. FCI methods allow for accurate calculation of two-electron energies through diagonalization of the interacting two-electron Hamiltonian in the basis of

3160 Slater determinants generated by using the TB solutions. Therefore, the combination of these two procedures capture the interplay among the valleys, interface disorder and e-e interactions.

The FCI calculations use a number of experimentally driven input parameters. This includes the measured E_{orb} for each point, a vertical electric field of 0.7 MV m^{-1}, a 9 nm thick quantum well and atomic steps at the quantum well interface separated by 35 nm. The confinement potential of the quantum dot is based derived from E_{orb}, which is used in the form of a harmonic potential for determining the electron wave function in the x-y plane of the quantum dot. Additionally, this influences the strength of e-e interactions. The procedure for simulating valley and singlet-triplet energies is detailed more thoroughly in Chapter 2.

For the calculation of quantum dot position with respect to the position of atomic steps at the quantum well interface, the following procedure is used: first, the singlet-triplet and valley splittings are simulated as the quantum dot position changes. The dot position is varied in steps of 1.76 nm such that a matrix of 20 values are simulated between two atomic steps separated by 35 nm. Next, the simulated values are compared to experimental values, and the point which simultaneously has the smallest total error between simulation and experiment for both singlet-triplet and valley splittings is chosen. Finally, the dot is only allowed to move in one direction, otherwise the results would be unphysical. This condition is enforced by noting that the simulations produce a reflectional symmetry halfway between the steps. Two low-error simulations are found on both sides of this symmetry point. Thus,

once the quantum dot has moved past the symmetry point, it cannot move backwards across it.

Appendix D

Supplemental information for Chapter 5

D.1 Additional information for Figure 1

The data in Fig. 5.1 presents two distinct dispersions that are individually addressable. To produce Fig. 5.1(h), we averaged three data sets taken consecutively, as shown in Fig. D.1(a). Additional data at low detuning is seen in Fig. D.1(b). The purple circles in Fig. 5.4(b) are produced by fitting the resulting data from Fig. D.1(a,b) for the frequency of oscillation. Similarly, to produce Fig. 5.1(j) we averaged the data shown in Fig. D.1(c). Additional data taken at high detuning is shown in Fig. D.1(d). Since the two plots in Fig. D.1(d) are at different time steps, these data are first fit for their oscillation frequencies and the two fits

are averaged together. The green triangles in Fig. 5.4(b) are produced by fitting the results from Fig. D.1(c,d).

The differences in size of the Rabi oscillations in Fig. 5.1(g,i) and the differences in shape between Fig. 5.1(g,i) and Fig. 5.1(h,j) for the two microwave frequencies are indicative of two distinct energy levels. In order to map the resulting dispersions from Fig. 5.1(h,j) relative to each other, Fig. 5.1(g,i) are repeated at the same detuning, achieved using the microwave drives of $f_{\mathrm{R}} = 8.33\,\mathrm{GHz}$ and $f_{\mathrm{R}} = 6.75\,\mathrm{GHz}$, as shown in Fig. D.1(e,f). Rabi frequencies extracted from Fig. D.1(e,f) are represented in Fig. 5.4(b) by including the $f_{\mathrm{R}} = 6.75\,\mathrm{GHz}$ magenta star at the same detuning as the $f_{\mathrm{R}} = 8.33\,\mathrm{GHz}$ orange star. Though we do not observe off resonant oscillations from one spectrum in measurements of the other, it does appear that the region of suppressed coherence in Fig. D.1(e) is the region of enhanced coherence in Fig. D.1(f) and visa versa.

The resonance in Fig. D.1(f) belongs to the same energy level as that in Fig. 5.1(i), as can be seen by comparing Ramsey spectroscopy taken at the two f_{R} locations, as shown in Fig. D.1(g,h). The general shape of the data in Fig. D.1(g,h) is consistent, and the only difference is a relative shift in δV_{P2} by 0.96 mV. To produce the points in Fig. 5.4(b), we shifted the data in Fig. D.1(d,h) by $\delta V_{\mathrm{P2}} = 0.96\,\mathrm{mV}$ so that they match the detuning in Fig. D.1(g),

as experimentally measured. The data in Fig. 5.4(b) is converted from gate voltage to detuning with a detuning alpha of $\alpha_{\varepsilon,P2} = 0.085 \pm 0.009$.

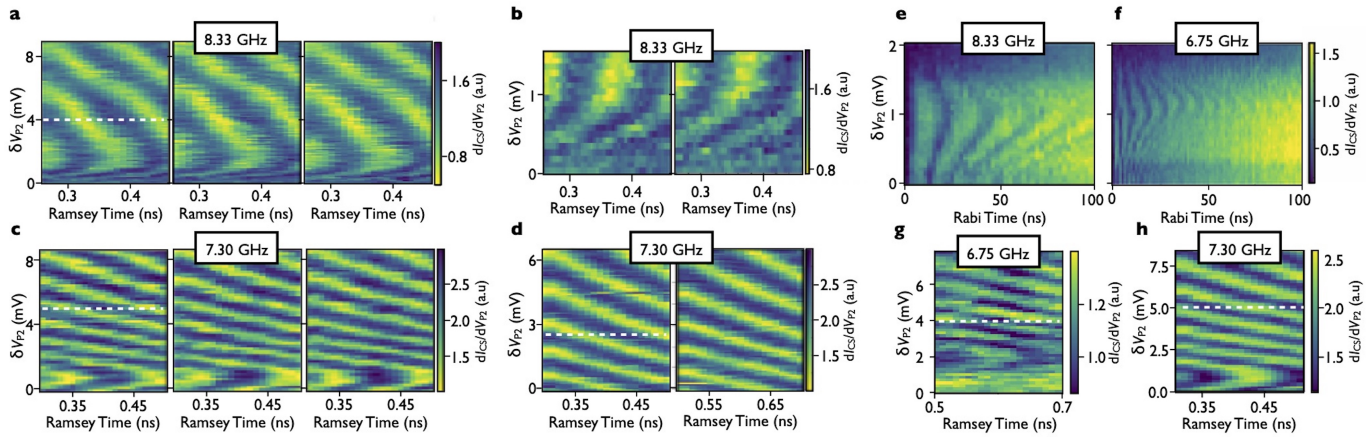

Figure D.1: Ramsey oscillation data averaging and alignment. (a) Ramsey oscillations with $f_{\mathrm{R}} = 8.33$ GHz taken consecutively. These data are averaged together to produce Fig. 5.1(h). (b) Ramsey oscillations with $f_{\mathrm{R}} = 8.33$ GHz taken consecutively. These data are averaged together, and the resulting oscillations, in addition to those from (a), are fit to produce the purple circles in Fig. 5.4(b). (c) Ramsey oscillations with $f_{\mathrm{R}} = 7.30$ GHz taken consecutively. These data are averaged together to produce Fig. 5.1(j). (d) Ramsey oscillations with $f_{\mathrm{R}} = 7.30$ GHz taken consecutively. The oscillations in these data are fit and the corresponding fits are averaged together. Those points, in addition to those resulting from fitting (c), produce the green triangles in Fig. 5.4(b). (e) Rabi oscillations for the same resonance as Fig. 5.1(g), with $f_{\mathrm{R}} = 8.33$ GHz. (f) Rabi oscillations for the same energy level as Fig. 5.1(i) but a different detuning, now with $f_{\mathrm{R}} = 6.75$ GHz. This data set is taken directly after (e), with the only change being the microwave drive. The centers of the two chevrons both correspond to $\delta V_{\mathrm{P2}} = 1.1$ mV. (g) Ramsey fringes corresponding to the resonance in (f) taken at $f_{\mathrm{R}} = 6.75$ GHz. (h) Ramsey fringes,taken at a different detuning, with the same $f_{\mathrm{R}} = 7.3$ GHz as Fig. 5.1(j). With the dispersion minima as reference, we use frequency data extracted from (h), and shift it accordingly so it reflects the detuning location in (g). This allows us to plot in Fig. 5.4(b) the coexistance of both dispersions. The white dashed lines in (a,c,d,g,h) denote the value of δV_{P2} for which the Ramsey detuning is zero.

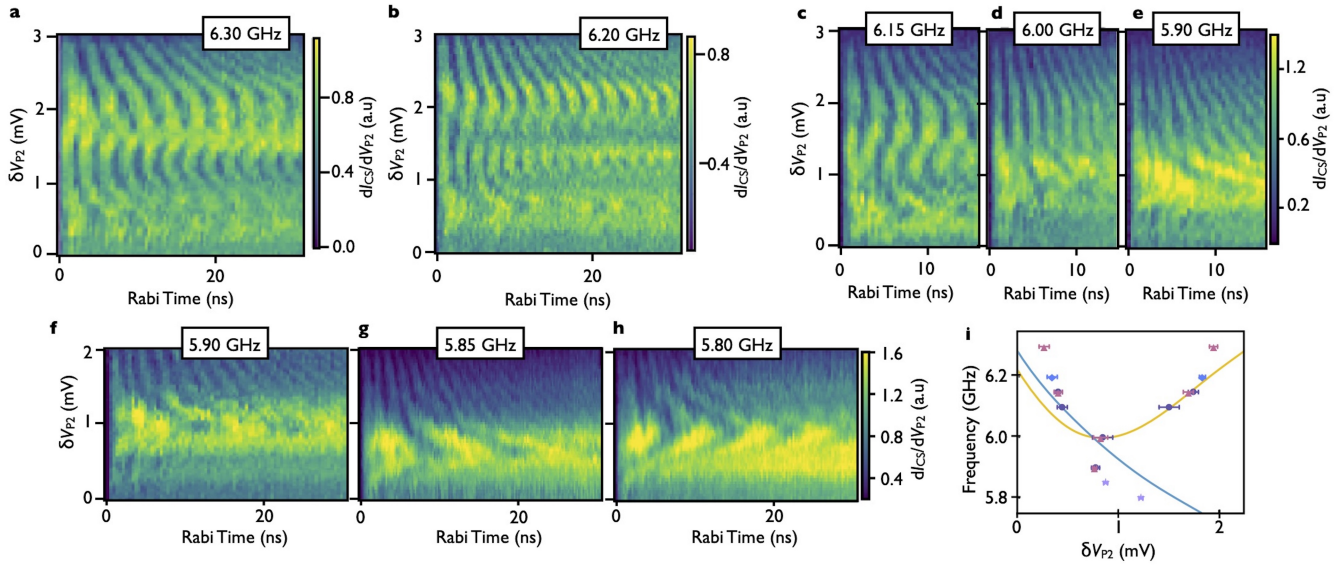

Figure D.2: Additional level crossing data corresponding to the dark blue diamonds in Fig 5.4(b). (a,b) Rabi oscillations at $f_R = 6.30$ GHz and $f_R = 6.20$ GHz . (c, d)Additional Rabi oscillations at $f_R = 6.15$ GHz and $f_R = 6.00$ GHz used to combine multiple sets of data with different V_{P2} offsets. (e,f) Rabi oscillations with $f_R = 5.90$ GHz, again used for combining multiple data sets. (g) Rabi oscillations with $f_R = 5.85$ GHz. (h) Rabi oscillations with $f_R = 5.80$ GHz. (i) All of the data from the navy and pink diamonds in Fig 5.4(b). Different markers correspond to data taken consecutively before device drift, as described in Table D.2. Blue and orange lines correspond to the interpolation functions $f(\varepsilon)$ and $g(\varepsilon)$, respectfully, which are described in section D.2.

D.2 Additional information on data and simulation for Figure 2

Table D.1: Sets of on-resonance oscillations discussed in Fig. 5.2 and Fig. D.2. Each set is separated by a line.

Set1		Set2	
f_R (GHz)	Figure	f_R (GHz)	Figure
6.30	Fig.D.2(a)	6.15	Fig.5.2(a)
6.15	Fig.D.2(c)	6.10	Fig.5.2(b)
6.00	Fig.D.2(d)	6.00	Fig.5.2(c
5.90	Fig.D.2(e)	5.90	Fig.D.2(f)

Set3		Set4	
f_R (GHz)	Figure	f_R (GHz)	Figure
5.85	Fig.D.2(g)	6.20	Fig.D.2(b)
5.80	Fig.D.2(h)	-	

Figures 5.2 and D.2 contain all the data used to extract the navy blue and pink diamonds in Fig. 5.4(b). Each diamond in Fig. 5.4(b) represents the center of a Rabi oscillation for a given drive frequency. As seen in Fig. 5.2, D.2, many of the data sets have two clear on-resonance oscillations. In these cases, both centers are plotted with the same frequency and different value of δV_{P2}. All of the extracted data from these two figures can be seen in Fig. D.2(i), where the different markers correspond to different sets of data taken consecutively (before the device shifted). These sets are enumerated in Table D.1. The uncertainty in Fig. D.2(i) is the uncertainty in the center of the oscillation, while the uncertainty in

these points in Fig. 5.4(b) includes uncertainty in their location relative to zero double-dot detuning.

The Rabi measurements shown in Fig. 5.2 indicate multi-level structure. We find that the best model that reproduces the main features of the experimental measurements in a simple way consists of four relevant states: two partially populated lower levels, separated by a small energy E_{01}, that make transitions to two excited states under detuning driving fields. The effective Hamiltonian of this four-level system is

$$H_0^{\text{toy}} = \begin{pmatrix} 0 & 0 & 0 & 0 \\ 0 & E_{01} & 0 & 0 \\ 0 & 0 & f(\varepsilon) & 0 \\ 0 & 0 & 0 & g(\varepsilon) + E_{01} \end{pmatrix}, \tag{D.1}$$

where $f(\varepsilon)$ and $g(\varepsilon)$ are interpolation functions based on the energy measurements, shown as blue and orange lines in Fig. D.2(i). We set $E_{01}/h = 3$ GHz, which is compatible with the small energy gap between the lowest two states observed in the experiment and large

Table D.2: Parameters R_{02} and R_{13} from Eq. D.2, in addition to the drive frequency f_{R} and ground state population ρ_{00}, which are all used for the simulations in Fig. 5.2(d-f).

	Fig.5.2(d)	Fig.5.2(e)	Fig.5.2(f)
f_{R} (GHz)	6.15	6.1	6.0
$R_{02} \times 10^3$	0.443	0.463	0.616
$R_{13} \times 10^3$	0.925	0.984	1.626
ρ_{00}	0.7	0.7	0.65

enough to avoid undesired interactions. The driving field is characterized by

$$H_1^{\mathrm{toy}} = \delta\varepsilon \cos(\omega t) \begin{pmatrix} 0 & 0 & R_{02} & 0 \\ 0 & 0 & 0 & R_{13} \\ R_{02} & 0 & 0 & 0 \\ 0 & R_{13} & 0 & 0 \end{pmatrix} \tag{D.2}$$

where R_{02} and R_{13} are fitting parameters. The only other fitting parameter is the ground state population

ρ_{00}, assuming $\rho_{11} = 1 - \rho_{00}$. The fitting parameters used for each case are shown in Table D.2.

We find that an even simpler model, such as a three-level system with a singly-populated ground state and two interacting excited states, might also be an explanation. However, the simulations with this simpler model added more unobserved interference phenomena. We note that the simple four-level model is rather limited since the values of the Rabi parameters R_{02} and R_{13} should depend on detuning. Moreover, the energy level landscape

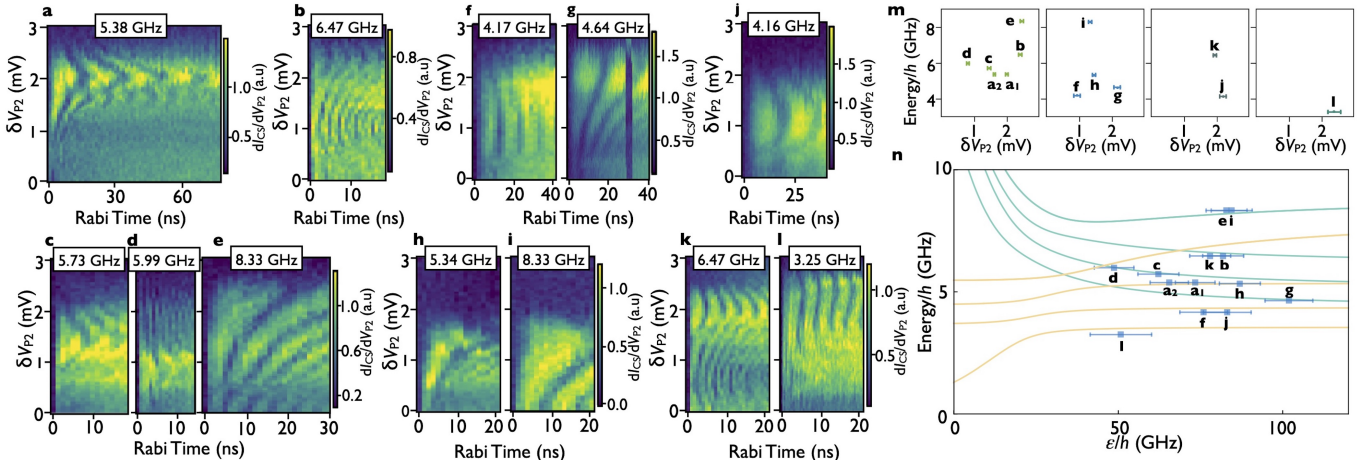

Figure D.3: Rabi oscillations associated with the blue squares in Fig 5.4(b), with frequencies (a) $f_R = 5.38$ GHz, (b) $f_R = 6.47$ GHz, (c) $f_R = 5.73$ GHz, (d) $f_R = 5.99$ GHz, (e) $f_R = 8.33$ GHz, (f) $f_R = 4.17$ GHz, (g) $f_R = 4.64$ GHz, (h) $f_R = 5.34$ GHz, (i) $f_R = 8.33$ GHz, (j) $f_R = 4.16$ GHz, (k) $f_R = 6.47$ GHz, (l) δV_{P2}= 3.25 GHz. (m) (a-l) were taken in four sets, where within each set there is no device shifting and corresponding adjustment. The sets are (a-e), (f-i), (j,k), and (l). The points in (m) represent the location in relative P_2 of the center of the Rabi oscillation for a given driving frequency. (n) These four sets are then placed onto the model by simultaneously matching (e,i), and (b,k), as well as looking at the distance of (e,l) from the approximate polarization line.

.

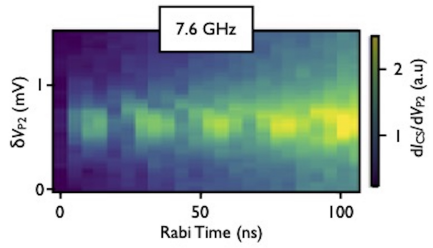

Figure D.4: Rabi oscillations associated $f_{\mathrm{R}} = 7.60\,\mathrm{GHz}$, shown as a light purple star in Fig. 5.4(b).

is more complicated than a four-level system. Nevertheless, this simple model captures the main features in the measurements.

Finally, to simulate the presence of noise in Fig. 3, we perform a Gaussian convolution with $\sigma_\varepsilon = 7.1\mu\mathrm{eV}$. This number is extracted by averaging the $\sigma_\varepsilon = \frac{\sqrt{2}\hbar}{|\frac{dE}{d\varepsilon}|T_2^*}$ computed with T_2^* and $\frac{dE}{d\varepsilon}$ from the 7.30 GHz and 8.33 GHz resonances shown in Fig. 5.2.

D.3 Additional data for Figure 4

Figure D.3, D.4 contains the measured Rabi oscillations corresponding to the plots in Fig 5.4(b). The data in Fig. D.3 is grouped in four sets, (a-e), (f-i), (j,k), and (l), as shown in (m). Each set represents a portion of data that is taken without any drift of the DQD device, and without changing any pulse-shape parameters besides microwave frequency. Each extracted point is obtained by looking at line-cuts in time through the data and estimating the center point of the oscillation in gate voltage. Note that all the data in these figures span 3 mV on the gate which dictates the quantum dot detuning, P_2. The drastic changes in size, shape, and frequency of these oscillations in the same relative window of detuning supports

the interpretation that these oscillations correspond to different energy level transitions. The data from (m) is mapped to the detuning axis in (n) by trying to simultaneously have both (e,i) and (b,k) be as close as possible. The location of (e,l) relative to the polarization line, which should be at the zero detuning point for the DQD, is approximated using their resonant locations within the latched readout region, stability diagrams and the pulse height.

The data in Fig. D.4 appears as a purple star in Fig. 4(b).

D.4 Simulation details for Figure 3

The simulation results shown in Fig. 5.3 are performed by combining a full configuration interaction (FCI) approach with the empirical tight-binding (TB) theory of Boykin et al. [62, 88]. In the TB model, the nearest-neighbor and the next nearest neighbor hopping parameters $t_1 = 0.6829$ eV and $t_2 = 0.6119$ eV are chosen such that the location of the resulting band minima coincide with the location of bulk silicon's conduction band minima and the effective mass, determined by the curvature of the conduction band at its minima, is equal to the lateral effective mass of bulk silicon. With an additional hopping parameter t_3, chosen such that the transversal effective mass of bulk Si is obtained, the model becomes two-dimensional in the x-z plane. We are thus able to study the effects of different interface profiles by simply assigning on-site terms E_{Si} and E_{SiGe} to grid points in different patterns. Resulting wave functions have fast oscillations in z that are responsible for the breaking of valley degeneracy, and disorder at the interface causes valley and orbital degrees of freedom to

couple. In the calculations, we treat the third dimension y analytically with the assumption that the confinement potential is parabolic.

While TB provides an accurate description of single electron wave functions by capturing the valley physics of silicon and allowing modeling of the quantum well interface disorder, FCI allows us to calculate two electron energies by including the effects of electron-electron interactions. After adding the spin degree of freedom, we generate all possible two-electron Slater determinants based on the 45 lowest energy TB eigenstates, which constitute the basis for the FCI calculation. We calculate the full Hamiltonian, including the electron-electron interaction term (with dielectric constant 11.4 [91]), in this basis and diagonalize it to obtain the two-electron energy eigenvalues and eigenstates. For the simulation in Fig. 5.3, we used a tilted quantum well interface with a tilting angle of $\sim 0.2°$, quantum well width of 9.1 nm and an electric field of 0.6 MV/m perpendicular to the interface. With these parameters, valley splittings range from 2.4 to 4.8 GHz (10 to 20 μeV) in the considered $\hbar\omega_x$ domain, and in particular is 3.81 GHz (14 μeV) for the $\omega_x/2\pi = 59.2$ GHz used in Fig. 5.3(a). We pick the location of the center of the dot with respect to the uniform steps at the interface to obtain the best agreement with the experimental data.

D.5 Electron-electron interactions

As described in the main text, the Wigner parameter $R_{\mathrm{W}} = E_{\mathrm{ee}} \,/\, E_{\mathrm{orb}}$ is used to classify Wigner molecules. Here we take $E_{\mathrm{orb}} = \hbar\omega_x$ and calculate the Coulomb energy of two point charges separated by the characteristic length scale of the quantum dot, which is a typical

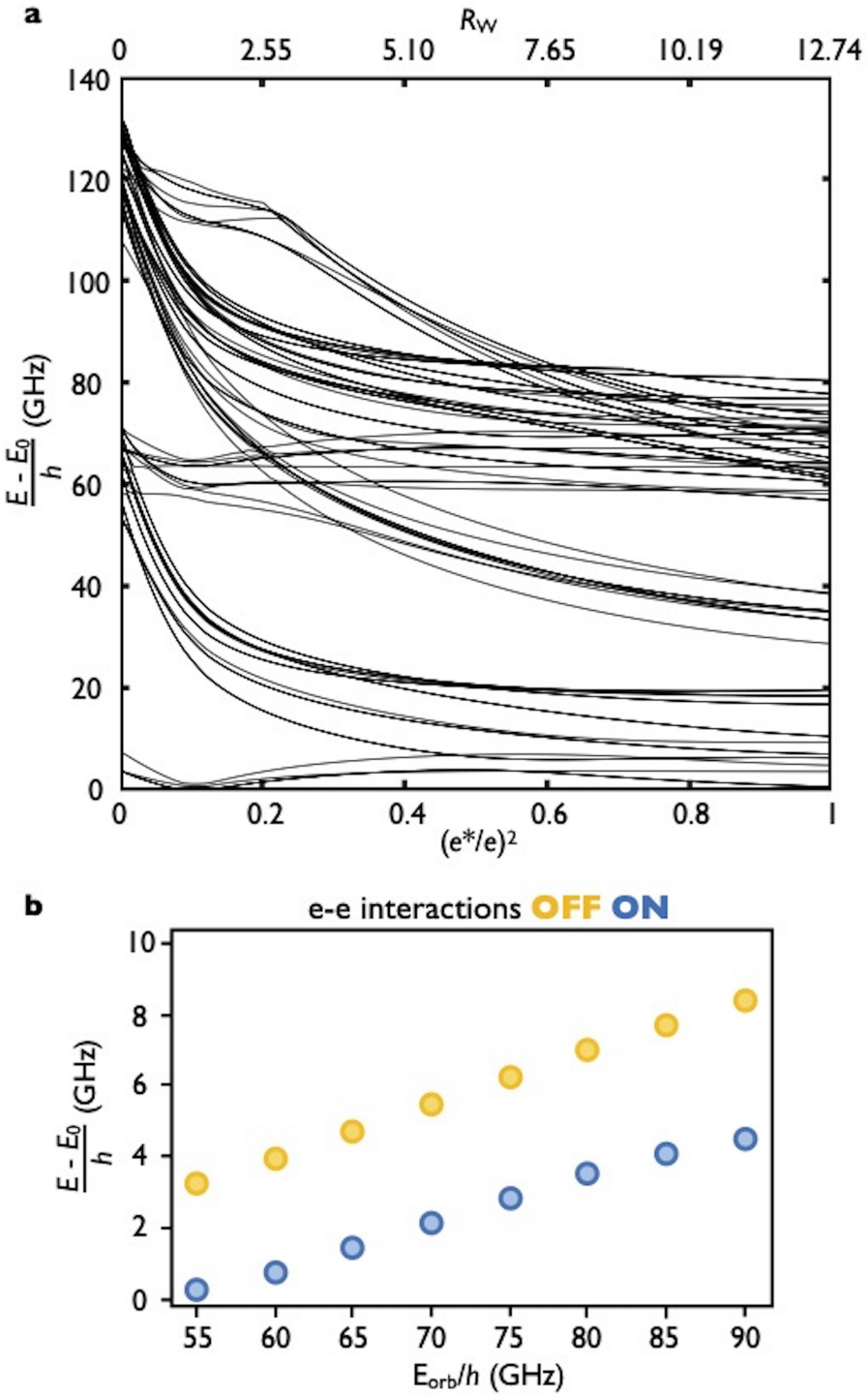

Figure D.5: Additional FCI data (a) Two-electron energy level separation from the ground state at $E_{\text{orb}}/h = 59.2$ GHz plotted as a function of the relative interaction strength $(e^*/e)^2$ (bottom) and Wigner parameter R_{W} (top), showing suppression of excitation energies due to electron-electron interactions. (b) Two-electron energy levels with electron-electron interactions turned off (on) are plotted in yellow (blue) as a function of orbital confinement.

measure of the electronic repulsion in the system. This results in $E_{\text{ee}} = \frac{e^2\sqrt{m_t\omega_x/\hbar}}{4\pi\epsilon}$, where m_t is the effective mass. Using the m_t and relative permittivity in Si, with $E_{\text{orb}}/h = 59.2$ GHz consistent with the FCI calculations presented in Fig. 5.3, we obtain $R_{\text{W}} = 12.74$.

To closely observe the effects of electron-electron interactions on the energy spectrum, we gradually introduce them in our simulations by using an artificial electron charge e* that ranges from 0 to real electron charge e. Two-electron energy level splittings from the ground state are plotted in Fig. D.5 as a function of both $(e^*/e)^2$ and R_{W}. In the absence of electron-electron interactions, the two-electron energy spectrum is dictated by smaller (5-15 GHz) valley splittings and larger (60 GHz) orbital splittings. With increasing interaction strength, two-electron wave functions are formed with contributions from many excited valley and orbital states, as the electrons are increasingly driven away from each other. This hybridization results in densely packed energy levels in the strong interaction regime, which is seen in Fig. D.5.

Table D.3: Parameters for Eq. D.3 chosen to best fit the data and percent change in each parameter that degrades the fit.

Energy			Tunnel Coupling		
E_n	E/h (GHz)	δE (%)	Δ_n	Δ/h (GHz)	$\delta\Delta$ (%)
-	-	-	Δ_0	6	10
E_1	0.75	20	Δ_1	1.5	30
E_2	4.3	10	Δ_2	1.5	30
E_3	5.1	8	Δ_3	1.5	30
E_4	6.1	5	Δ_4	1.5	30
E_5	9	4	Δ_5	10.5	10

D.6 Choice of Hamiltonian Parameters for Figure 4

The lines in Fig. 5.4(a) are the eigenvalues of

$$H = \begin{pmatrix} \varepsilon/2 & \Delta_0 & \Delta_1 & \dots & \Delta_5 \\ \Delta_0 & -\varepsilon/2 & 0 & \dots & 0 \\ \Delta_1 & 0 & -\varepsilon/2 + E_1 & \dots & 0 \\ \Delta_2 & 0 & 0 & \ddots & 0 \\ \Delta_3 & 0 & 0 & \dots & 0 \\ \Delta_4 & 0 & 0 & \dots & 0 \\ \Delta_5 & 0 & 0 & \dots & -\varepsilon/2 + E_5 \end{pmatrix}, \tag{D.3}$$

which describes a system of five excited states in the right quantum dot coupled to the left quantum dot. The values for energies E_n and tunnel couplings Δ_n are listed in Table D.3. Though we have a large quantity of data, including two detuned-Ramsey measurements of different levels (Fig. 5.1(h,j)), Rabi measurements of eight different levels(Fig. 5.1(g,i), Fig. D.3), and Rabi measurements of two merging levels(Fig. 5.2(a-c), Fig. D.2), the five-level model from Fig. 5.4(b) based on Eq. D.3 is still under-constrained. It has 11 independent parameters: five energies, E_1 – E_5, and six tunnel couplings, Δ_0 – Δ_5.

The detuned Ramsey data from Fig. 5.1(h) (purple circles in Fig. 5.4(b)) provides an approximate value for E_5 and Δ_5, which respectively govern the high-detuning asymptote and low-detuning shape of E_{05}. Similarly, the set of detuned Ramsey data from Fig. 5.1(j) (green triangles in Fig. 5.4(b)) places strong constraints on E_{15}. Since $E_{05} - E_{15} = E_{01}$, these two Ramsey sets of data together constrain the high-detuning asymptote and low-detuning shape of E_{01}, thereby dictating the values of E_1 and Δ_0. With this constraint on E_{01}, the relation $E_{0n} - E_{1n} = E_{01}$ narrows the values of the other energies E_2-E_4. Each energy E_n has at least two Rabi measurements (one for E_{0n} and one for E_{1n}) to define its value. Table D.3 shows the percent change in each energy E_n which degrades the fit.

The individual tunnel couplings $\Delta_1 - \Delta_4$ are not as firmly constrained as the energy values. However, as all the eigenvalues are interdependent, the individual tunnel couplings as well as the sum of the tunnel couplings are constrained to be within a certain range. For example, having any or all of Δ_n too large will push both E_{01} downward and E_{05} upward, both of which are well constrained, as discussed above. Table D.3 shows the percent change

Table D.4: Expected ground (ρ_0) and excited state ($\rho_{1,3}$) populations based on the pulse sequence used.

	Pulse 1	Pulse 2	Pulse 3	Pulse 4
ε_h (μeV)	680	646	612	816
t_g (ns)	6	6	6	9
ρ_0	0.841	0.873	0.872	0.864
ρ_1	0.082	0.083	0.082	0.076
ρ_3	0.054	0.023	0.026	0.038

in each tunnel coupling Δ_0 and Δ_5, as well as the percent change for all the tunnel couplings Δ_1-Δ_4 which are set equal, that degrades the fit.

D.7 Estimations of excited-state populations

In the experiment, the qubit is initialized at very negative detuning values. In this region, the ground state is well-separated from the first-excited state, ensuring proper initialization. To manipulate the qubit, the detuning is pulsed from this region to positive detuning. Due to the large number of low-lying excited states, some excited states may be populated during this process. To estimate the excited-state populations, we simulate the initialization pulse to the positive detuned regime.

To describe the qubit, we consider the effective model given by Eq. D.3. This model, while an approximation, provides intuition on the interactions with the excited states. In the experiment, the initial detuning value ranges from -400 to $-300\,\mu$eV (-97 to $-73\,$GHz). Since the experimental pulses go from the negative far-detuned regime to the positive detuned regime, the exact initial detuning position is not relevant; hence, we choose $\varepsilon_0 = -350\mu$eV.

The simulated pulse is simply $\varepsilon(t) = \varepsilon_0 + \varepsilon_h/t_g \cdot t$, where ε_h is the pulse height and t_g the duration of the pulse.

We consider the four different experimental pulses in Table D.4, which are representative of the pulses used in this work. The three states with the highest initialization population are also shown in the table. The results show that the ground state is the most populated, and that there is non-negligible population in the first excited state, consistent with the experimental results reported in the main text. The third excited state, which has the next highest initialization population, is less populated and not observed in the experiments.

D.8 Pulses and pulse corrections

Pulses are generated using a two-channel Textronix AWG 70002A and changing the relative skew between the two channels. We perform lock-in measurements at the frequency with which we modulate on and off the application of microwave pulses. Each pulse consists of a short manipulation phase followed by a longer measurement phase of typical duration 1.2 μs. The typical modulation frequency is around 10kHz. The reported Ramsey fringes are the amplitude of the lock-in signal

The pulse sequences we use consist of quasi-dc changes in detuning combined with ac microwave bursts. Because of the frequency dependent attenuation down the dilution refrigerator, we apply pulse corrections to make our dc pulses more similar to the intended shape. We use S21 measurements of the high frequency lines to determine the frequency dependent attenuation expected. We then take a FFT for a step function, and weight the spectrum

according to our S21 measurements. An inverse FFT is taken to obtain the corrected pulse segment, which becomes the building block for our new pulse sequence. We apply the corrected building block for every change in dc level to our intended dc pulse sequence. This pulse sequence visually looks like an overcorrection of the pulse in order to counteract the measured finite rise-time. We finally add in any ac components to our pulses. After these pulse corrections, there is still an observable drift in the top of the pulse as a function of time for short times (Ramsey measurements). To place points on Fig. 5.4(b) it is important to know the detuning. Thus, we perform additional post-processing to the Ramsey data by shifting line scans with the function $A(1 + be^{-t/\tau})$ in order to align the dispersion minima of consecutive Ramsey oscillations. This allows us to accurately plot detuned Ramsey data for small times, such as the purple circles and green triangles in Fig. 5.4(b). Here, A is the detuning pulse amplitude, $b = 0.2$, and $\tau = 1.8\,\text{ns}$.

Appendix E

Measurement-free implementations of small-scale surface codes for quantum dot qubits

This appendix is adapted from the article Phys. Rev. A 97, 012318, "Measurement-free implementations of small-scale surface codes for quantum dot qubits".

E.1 Introduction

Protecting quantum information against noise is one of the most important challenges for building a quantum computer [173]. Quantum error correction (QEC) addresses this issue by making use of redundancy [13]. Among many QEC approaches, surface codes are considered to be particularly promising, with threshold error rates up to 1% [174, 175, 12].

However, the practicality of a QEC procedure also depends on the physical implementation of the qubits. Surface codes, as well as other standard QEC approaches, rely heavily on syndrome measurements, and the threshold calculations in the literature commonly assume that qubit measurements can be done within a gate time with failure probability equal to the gate failure probability. This assumption does not hold for several qubit implementations, including quantum dot qubits, for which readout times are several orders of magnitude longer than the gate times [20, 176, 177, 81]. Therefore, conventional implementation of surface codes on these qubits seems challenging. On the other hand, DiVincenzo and Aliferis [178] have shown that in a truly large scale quantum computer, error correction can be performed using slow measurements, because the measurements can take place concurrently within the many levels of concatenation required to achieve fault tolerance. While of great interest for future applications, this result does not address the challenges faced by intermediate-scale implementations of 10-100 qubits, which realistically comprise only 1-2 levels of concatenation.

To overcome problems associated with measurement, it has been noted that the conventional widget used in syndrome measurements (a measurement followed by classical feedback), may be replaced by an alternative widget (a unitary gate operation followed by qubit re-initialization) [179, 180, 181, 182, 183, 184]. An example of such a measurement-free circuit is shown in Fig. E.1. For many years it was thought that the error thresholds achievable using this strategy would be prohibitively low. However, Paz-Silva *et al.* demonstrated that measurement-free error correction for the Bacon-Shor code could have thresholds only about

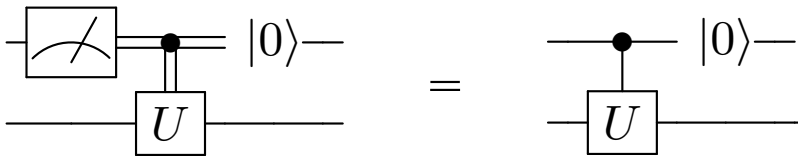

Figure E.1: Equivalence of unitary controlled operations with measurement and re-initializations. A unitary operation determined by the result of a measurement of an ancilla followed by re-initialization of the ancilla (left circuit) is equivalent to a unitary controlled operation followed by the re-initialization of the control qubit (right circuit). Double lines in the left circuit represent a single classical bit. In both circuits, $|0\rangle$ indicates a rapid re-initialization of the qubit to its 0 state. For quantum dots, this involves tunneling to and from a reservoir.

an order of magnitude worse than conventional schemes [185]. More recently, Crow *et al.* improved these results by using redundant syndrome extractions and reported thresholds for three qubit bit-flip (BF), Bacon-Shor, and Steane codes that are comparable to measurement-based values [186]. However, measurement-free surface code implementations have not yet been thoroughly investigated. Indeed, it has been argued that in this case, measurement-free implementations would significantly reduce the advantage of surface codes because the nontrivial classical matching problem used in this procedure relies on the results of error syndrome measurements to determine the recovery operations [187].

Here, we show that this is not the case, for low-distance surface codes where the matching process can be simplified significantly [185]. We investigate the performance of measurement-free QEC by simulating quantum circuits, obtaining threshold values for BF and surface codes of 2.0×10^{-2} and 1.3×10^{-4}, respectively. These measurement-free thresholds can be compared to thresholds of 2×10^{-2} and 8.0×10^{-4} for the corresponding measurement-based procedures [188, 189].

This appendix is organized as follows: In Sec. E.2 we give an overview of QEC with surface codes and define necessary terms to make our discussion self-contained. In Sec. E.3 we explain in detail the changes we make to the conventional surface code implementations to replace measurements with unitary operations and re-initializations. We first discuss the assumptions we make for quantum dot implementations in Sec. E.3.1, then demonstrate our method for a surface code restricted to one dimension, which is equivalent to the BF code in Sec. E.3.2, and generalize it to a full surface code in Sec. E.3.3. In Sec. E.4 we discuss the details of the error model and the simulation method that we use. We summarize our results in Sec. E.5 and discuss them in Sec. E.6.

E.2 Stabilizer Codes

The codes we consider in this appendix belong to an important class of QEC codes known as *stabilizer codes* [179]. The logical space of a stabilizer code is determined by a group of *stabilizer operators* that leave this space unchanged under their action. Conventionally, stabilizers are repeatedly measured to ensure that the system remains in a simultaneous eigenstate of all of them. Over time, changes in the measurement outcomes indicate that errors have occured in the form of X, Y or Z qubit operators and that anti-commute with certain stabilizers. These operators are defined in terms of Pauli operators as $X = \sigma_x$, $Y = -i\sigma_y$ and $Z = \sigma_z$.

To take an example, we first consider the logical space of the three-qubit BF code, which is spanned by $|000\rangle$ and $|111\rangle$ multiqubit states. These states are stabilized by two

independent operators, Z_1Z_2 and Z_2Z_3. Here, the subscripts refer to physical qubits. As shown in Table E.1, each single bit-flip error X_1, X_2 or X_3 results in a different measurement outcome, or *error syndrome*. Our measurement-free circuit that replaces the conditional operations with a combination of unitary operations and re-initializations [179] is shown in Fig. E.2.

In a second example, we consider surface codes, which also utilize stabilizers. Surface code logical qubits can be arbitrarily large; here we focus on the specific 17-qubit surface code [189] shown in Fig. E.3, which we refer to as surface-17 code. This is a distance-three logical qubit with nine data qubits and eight ancilla qubits that correspond to the eight independent stabilizers. These stabilizers, and logical X and Z operators are listed in Table E.2. Eigenstates of the logical Z operator are defined as the logical $|0\rangle$ and $|1\rangle$ states. We note that the measurement-free implementations of surface-17 will employ more than 17 qubits but the code will still be referred to as surface-17 as the structure of data qubits and independent stabilizers do not change. In particular, the measurement-free implementation of surface-17 that employs 25 qubits should not be confused with surface-25, which

Table E.1: Stabilizers and syndrome values for the three-qubit bit-flip (BF) code. The two independent stabilizers are given in the first column. Each of the three possible bit-flip errors (X_1,X_2 or X_3) corresponds to different syndrome, uniquely identifying the error.

Stabilizer	Error syndrome			
	I	X_1	X_2	X_3
Z_1Z_2	0	1	1	0
Z_2Z_3	0	0	1	1

refers to a different distance-three surface code that employs 13 data qubits and 12 ancillas corresponding to 12 independent stabilizers.

In a general surface code, error syndromes cannot be uniquely matched with actual errors in the system; for a given set of error syndromes, physical error must be determined probabilistically. In a measurement-based surface code, this is done by storing a full history of stabilizer measurement outcomes from each error correction cycle, and using a classical minimum weight perfect matching (MWPM) algorithm [190] to match these syndromes with the most probable (i.e., the minimum weight) errors [12]. It is important to note that it is not necessary to correct errors immediately after they are detected. This is because the recovery operations belong to a Pauli group which is closed under the action of the Clifford group elements that contain all the gates needed for error correction [191, 178].

Here, motivated by our interest in implementing error correction in experimental systems with moderate numbers of qubits, we investigate the performance of small surface codes that are implemented in a measurement-free fashion. As pointed out in Ref. [189], syndrome–error matching for a small scale, distance-three, surface code is substantially simpler than for larger codes when only a short history of syndromes is used; in this case, MWPM can be reduced to the application of few simple rules which we summarize below.

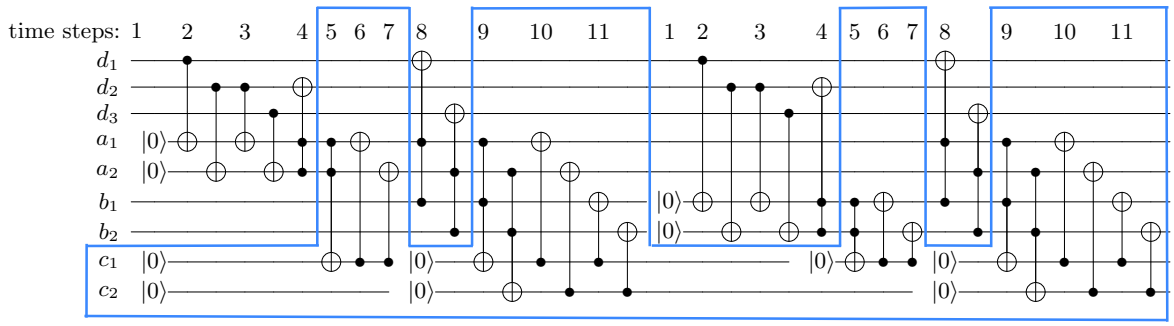

Figure E.2: The error-extraction and correction circuit for the bit-flip (BF) code, a one-dimensional surface code that only corrects bit-flip errors. Here, d_1, d_2 and d_3 are data qubits and the rest are ancillas. The error information is extracted to ancilla pairs $\{a_1,a_2\}$ and $\{b_1,b_2\}$ in alternate time cycles, as shown in the figure. (A given cycle corresponds to time steps 1-11, where a particular step may be comprised of 1-2 gates that can be implemented simultaneously.) This two-cycle sequence ensures that single-data-qubit errors are always signaled by exactly two syndromes. A data error on d_2 flips both ancilla qubits that interact with d_2 in that cycle. A data error on d_1 or d_3 flips the pair $\{a_1,b_1\}$ or $\{a_2,b_2\}$, respectively. Using these ancilla pairs as the controls and the relevant data qubits as the targets of the Toffoli gates, all single bit-flip errors are corrected. Whenever a Toffoli gate corrects an error, the control qubits must return to state $|0\rangle$ so that the matching is perfect, i.e. any syndrome is associated with at most one error. To do that, for each error-correcting Toffoli gate we employ another one targeting either c_1 or c_2 ancilla qubits and use these ancillas as the control qubits for two CNOT gates whose targets are the two control qubits of the error-correcting Toffoli gate. The portion of the circuit responsible for perfect matching is enclosed in the blue box in the figure. Excluding this subcircuit simplifies the QEC procedure considerably without significantly affecting its ability to correct single errors, as explained in the Appendix.

Table E.2: Stabilizers and logical operators for the bit-flip (BF) and surface-17 codes. Standard operators for the BF code [179] and the surface-17 code of Ref. [189] are also given for completeness of presentation.

BF code		Surface-17	
Z stabilizers		X stabilizers	Z stabilizers
Z_1Z_2		X_2X_3	Z_1Z_4
Z_2Z_3		X_7X_8	Z_6Z_9
		$X_1X_2X_4X_5$	$Z_2Z_3Z_5Z_6$
		$X_5X_6X_8X_9$	$Z_4Z_5Z_7Z_8$
Logical X	Logical Z	Logical X	Logical Z
$X_1X_2X_3$	$Z_1Z_2Z_3$	$X_3X_5X_7$	$Z_1Z_5Z_9$

E.3 Measurement-free error correction

E.3.1 Assumptions for quantum dot implementations

We have argued that the measurement-free QEC scheme is appropriate for quantum dot qubits due to the fact that measurements are relatively slow, and therefore expensive, while qubit re-initialization is relatively fast, and therefore cheap. We make use of this fact by using re-initialization repeatedly, and by assuming that the speed of re-initialization is similar to a unitary gate operation.

In this work, we also make several other assumptions appropriate for quantum dot qubits. First, to make up for the fact that measurement is expensive, we will assume that adding additional ancilla qubits to our circuits is relatively cheap. This is motivated by the fact that quantum dots are considered to be a scalable qubit technology. Second, we note that long-range couplings between quantum dots are possible, in principle. For example, strong

coupling between a double quantum dot and a microwave resonator has recently been demonstrated [192], suggesting that long-range couplings between qubits could be achieved in the near future. Hence, we assume that two- and three-qubit gates can be implemented natively in our circuits (i.e., in a single time step), even when the qubits are not in close proximity. For example, three-qubit Toffoli and controlled-controlled-Z (CCZ) gates play an important role in our scheme because, as will be explained later, correction of a data qubit error depends on the state of two ancilla qubits. For simplicity here, we further assume that Toffoli and CCZ gates can be implemented with the same error rate as other gates.

E.3.2 Bit-flip (BF) code

The three-qubit BF code can be seen as an isolated line of three data and two ancilla qubits in a surface code. Therefore, the strategies developed in this setting can be easily generalized to more complicated cases, such as the surface-17 code. In this work, we only apply our error correction methods to logical identity gate operation, not to the logical X and Z gate operations described in Table E.2.

Below, we describe an error-correction strategy that is fault tolerant against single-qubit BF errors, including errors on both the data qubits and the ancillas. The method requires verifying information redundancy in space, as well as over time as our aim is to implement the conventional surface code error-correction strategy without measurements [12]. The latter involves storing and comparing syndrome information over consecutive cycles. The BF and

surface codes considered here both require two time cycles to complete their correction sequences.

The full error-detection and correction circuit for two consecutive cycles of the BF code is shown in Fig. E.2. Here, the logical qubit is comprised of three data qubits (d_1-d_3) and eight ancillas. As discussed in Sec. E.2, there are two independent stabilizers and the syndrome information corresponding to each of these stabilizers is extracted to two ancilla qubits (a_1, a_2). Since we consider two consecutive time cycles, a separate pair of ancillas (b_1, b_2) is required to store the second set of stabilizer information. Note that in the beginning of the first cycle of the figure, b_1 and b_2 carry information from the previous time cycle, which is not shown here. This scheme is different than measurement-based strategies, for which the result of the syndrome measurement is simply stored in a classical memory. In each cycle, the four syndromes are compared. If a match occurs, it signifies an error, which is then corrected by applying Toffoli gates (e.g., at time steps 4 and 8 in the figure). An important point is that each error syndrome occurs in only one matched pair, which is why such a matching is called "perfect". To ensure that the matching signaled by our circuit is "perfect," any syndrome information used to correct an error should be removed from the system before the beginning of the next time cycle. This is done with the help of two additional ancillas (c_1 and c_2). For each error-correcting Toffoli gate T (e.g., at time step 4) there is another Toffoli gate T$'$ (time step 5) that employs the same control qubits but has a c ancilla as its target. If an error is corrected by T, the c ancilla which is initially in state $|0\rangle$, is flipped by T$'$, indicating that an error has been corrected. Two additional CNOT gates (time steps 6 and

7) and a subsequent re-initialization of c_1 and c_2 use this information to remove syndrome information from the system, preventing further matching.

The key to the fault tolerance of the above scheme is that no single bit-flip error in either the data or ancilla qubits can cause a logical error. Using Toffoli gates for error correction requires having signals from two ancilla qubits. Therefore, for errors to propagate from ancilla qubits to data qubits at least two ancilla qubits must be flipped. Although there are cases where a single error can propagate into the two ancilla qubits, they are reset before being used in a Toffoli gate that can affect the data qubits. For example, an error occuring on qubit c_1 after time step 5 of the first cycle propagates into the qubits a_1 and a_2 but these qubits are reset in time step 1 (assuming cyclic repetition) before they can affect d_2 in time step 4.

As indicated by the blue box in Fig. E.2, a large portion of the full circuit is comprised of the gates that ensure perfect matching. Although perfect matching is necessary to correct certain error sequences, the additional gate operations it imposes can also introduce additional errors into the system that suppress the error threshold. It is therefore interesting to study an alternative QEC circuit with the perfect-matching components removed. We will discuss the effects of these two approaches (i.e., longer circuit with perfect matching vs. shorter circuit with imperfect matching) on the performance of the surface code error correction in Sec. E.5 and explain them in more detail in the Appendix.

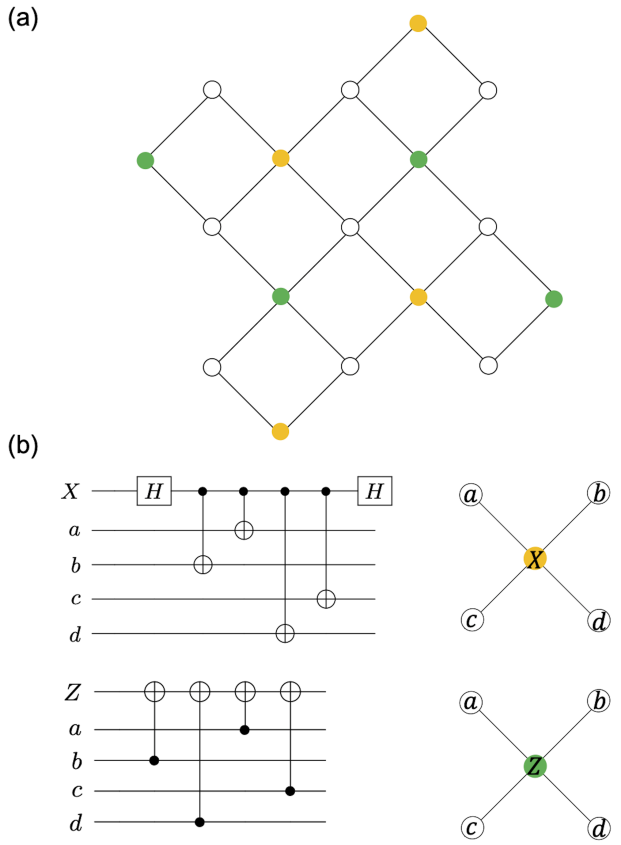

Figure E.3: (a) Architecture of a 17-qubit, distance-three surface code, introduced in Ref. [189]. Data qubits are denoted by the hollow circles whereas the X and Z syndrome qubits are denoted by orange (light) and green (dark) solid circles, respectively. (b) Standard syndrome-extraction circuits for X and Z syndromes, for the qubit orientations shown on the right. The circuits for the exterior ancillas that have only two neighboring data qubits involve fewer gates, with the same relative ordering.

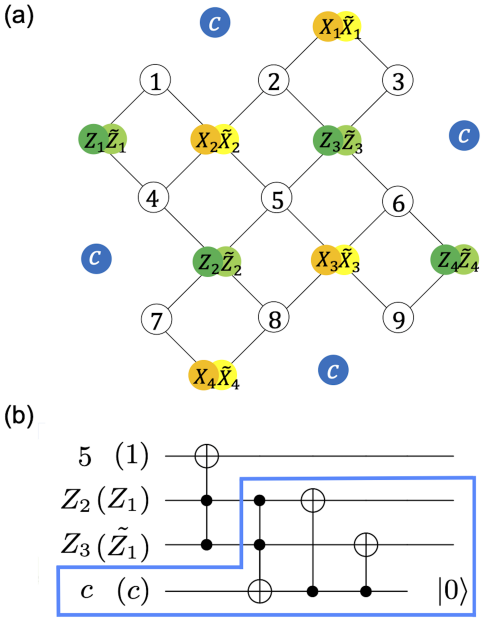

Figure E.4: (a) 29-qubit system for implementing measurement-free error correction of a distance-three surface code for nine data qubits. The data qubits are denoted as open circles labeled 1 to 9. These qubits and their error extraction syndromes, $X_1, ..., X_4, Z_1, ..., Z_4$ are present in the measurement-based architecture shown in Fig. E.3(a); twelve additional ancilla qubits (four c qubits and $\tilde{X}_1, ..., \tilde{X}_4, \tilde{Z}_1, ..., \tilde{Z}_4$) are present in the measurement-free architecture. Syndrome information is extracted into two sets of eight ancilla qubits, $S_1 = \{X_1, ..., X_4, Z_1, ..., Z_4\}$ and $S_2 = \{\tilde{X}_1, ..., \tilde{X}_4, \tilde{Z}_1, ..., \tilde{Z}_4\}$, in alternate time cycles. Four ancilla qubits, denoted as blue filled circles labeled c, are used to remove used syndrome information from the system. The positions of the qubits in the figure do not necessarily represent the actual physical geometry, particularly since we have assumed long-distance couplings. (b) A portion of the circuit used to implement measurement-free X-error correction. Here, the syndrome has already been extracted and stored on the Z ancilla qubits. Two different cases are illustrated in the figure. Case 1: if there is an X error on qubit-5, a Toffoli gate controlled by two Z syndrome qubits from S_1 corrects this error. All data qubits that have two neighboring ancilla qubits, of the same type (i.e., XX or ZZ), in the 17-qubit architecture are corrected in this way as well. Case 2 (in parentheses): if there is an X error on qubit 1, the error-correcting Toffoli gate is controlled by one Z syndrome qubit from S_1 and one from S_2, corresponding to the syndromes extracted in two consecutive cycles. Other data qubits with only one neighboring ancilla qubit, of a given type, in the 17-qubit architecture are corrected in this way as well. The remaining gates remove the used syndrome information from the ancilla qubits with the help of the c qubits. The Z error correction circuit is analogous, using X syndrome qubits instead of Z syndrome qubits and CCZ gates instead of Toffoli gates. As in Fig. E.2, the portion of the circuit in the box is responsible for perfect matching.

E.3.3 Distance-three surface code

Here we generalize the strategy used for the BF code to the distance-three surface code of Refs. [189, 193]. A more thorough description of the surface code is presented in [12]. For our purposes, it is sufficient to note that isolated errors in the code (e.g., bit flips or phase flips) may be tolerated if they do not affect the topology of the encoded qubit. However, a line of errors extending across the two-dimensional array does change the topology, and represents a logical error. Figure E.3(a) shows the architecture of the surface-17 code appropriate for measurement-based error correction. Here, the 9 data qubits indicated as open circles. Conventional syndrome extraction is performed on each proximal set of data qubits, as discussed in Ref. [189], and the resulting syndrome values are stored in the 8 ancilla qubits indicated as colored circles in Fig. E.3(b). Two types of syndrome protocols (X and Z) are now required, since the two-dimensional code corrects both bit-flip and phase-flip errors. The specific circuits needed for syndrome extraction involve CNOT and Hadamard gates, as shown in Fig. E.3(b). To enable fault-tolerant, measurement-free error correction, we modify the 17-qubit architecture along the same lines as was done for the BF code. Specifically, we add eight new ancillas that store the syndrome information from the preceding error correction cycle. In Fig. E.4(a), the syndromes obtained in different time cycles are indicated as pairs of filled circles with different labels. Errors are then detected and corrected according to the following rules:

- If a X(Z) type data error occurs and the erroneous data qubit has two neighboring

Z(X)-syndrome qubits in the original architecture in Fig. E.3(a), implementation of a Toffoli (CCZ) gate controlled by those ancillas corrects the error.

- If a X(Z) type data error occurs and the erroneous data qubit has only one neighboring Z(X)-syndrome qubit in the original architecture in Fig. E.3(a), then error correction is performed only after the same syndrome is extracted again in the next time cycle. The correction is performed by applying a Toffoli (CCZ) gate controlled by two ancillas storing the syndrome information corresponding to the same stabilizer in two consecutive cycles.

It is crucial to take into account the history of the syndromes for achieving fault-tolerance. To see this, consider an X error that occurs on qubit 5 in Fig. E.4(a). Ideally, this causes the two neighboring Z syndrome qubits to get flipped by two CNOT gates in the syndrome extraction circuit [Fig. E.3(b)]. However, if the error occurs between the application of these two CNOT gates, only one of the neighboring Z syndrome qubits will be flipped, falsely indicating an error on qubit 3. If the error-correction is done based on only this information (i.e., without comparing information from subsequent time cycles), an X gate will be applied to qubit 3 to"correct" a non-existing error, which adds a second error to the system. Now, the errors on qubits 3 and 5 cause qubit-7 to flip on a subsequent time cycle, resulting in a logical error. Obviously, such a scheme is not fault-tolerant as a single physical error can result in a logical error. On the other hand, in our circuit no error-correction is performed based on a single syndrome, as evident by the fact that all error-correcting gates (Toffoli or CCZ) involve three qubits. Using the circuit of Fig. E.4(b), the error considered above

would be ignored in the cycle in which it occurs, and it would get corrected in the following cycle, when both of the two neighboring Z syndrome qubits are flipped.

Once an error is corrected the syndrome information must be removed from the affected ancillas, as was done for the BF code. To do this we introduce four more ancillas, in contrast to the two ancillas needed for the BF code, to allow parallel operations to reduce the circuit depth. In total, this implementation employs 29 qubits. Figure E.4(b) shows the portion of the circuit that corrects X errors on one of the data qubits (1 or 5) based on the extracted syndrome in Z_1, Z_2, Z_3, and $\tilde{Z}_3$. To implement perfect matching, the syndrome information is then removed with the help of ancilla qubit c and the gates in the blue box. Using this scheme, a single error on syndrome qubits cannot affect the data qubits, which is important for achieving fault-tolerance. Fault-tolerance of the detection portion of the circuit is discussed in [189]. For the correction portion of the circuit, the discussion in the previous section also applies to this case, as the correction method is the same.

As noted in Sec. E.3B, the extra gates required by the perfect-matching procedure may suppress the resulting error threshold. By removing the gates in the blue box of Fig. E.4(b), the number of qubits required for implementing the surface code is reduced from 29 to 25. In Sec. E.5 and the Appendix, we perform simulations to investigate both the full and reduced surface-code circuits.

E.4 Simulations of algorithm performance

We have checked the performance of the error-correcting algorithms by performing numerical simulations. These simulations use the algorithm developed by Aaronson and Gottesman, which evolves stabilizers rather than the full state [194]. Toffoli and CCZ gates are not in the Clifford group and cannot generally be simulated with this method. However, in our simulations the control qubits of these gates are always in either $|0\rangle$ or $|1\rangle$ states. Hence, they can be"measured" and the gates can be performed in a classical manner, as in [186].

Our error model is composed of four different types of errors:

- Memory errors: after each ideal application of a single-qubit gate (including the identity), perform a π rotation about the X, Y or Z axis, with each occurring with probability $p/3$.
- Two-qubit gate errors: after each ideal application of a two-qubit gate, perform one of the 15 non-trivial tensor products of X, Y, Z and I, each occurring with probability $p/15$.
- Three-qubit gate errors: after each ideal application of a three-qubit gate, perform one of the 63 non-trivial tensor products of X, Y, Z and I, each occurring with probability $p/63$.
- Initialization errors: after an ideal initialization to $|0\rangle$, perform an X rotation with probability p.

We emphasize that all error processes are assumed to occur with equal probability, for the sake of simplicity. Our method for determining the logical error rate is based on estimating

the time-to-failure for the error-correction scheme, similar to Refs. [195, 189]. We initialize our system to the logical $|0\rangle$ state and then continue running the simulation with errors occurring at the physical error rate p, until the system arrives at the logical $|1\rangle$. To make our simulation more efficient, we make the following observation: especially for small values of p, the simulation involves many cycles in which no error occurs and the the state of the system remains the same. Instead of simulating the full error-correction circuit for each of these error-free cycles, we sample how many of them occur consecutively. To do that, we define P as the probability that no error occurs in a given cycle. Hence,

$$P = (1-p)^N,$$

where p is the physical error rate and N is the number of error sites in a cycle. Hence the probability of having no errors in $m-1$ consecutive cycles followed by at least one error in the m^{th} cycle is

$$P^{m-1}(1-P).$$

From this, the cumulative probability that the last, and only the last, cycle contains error(s) among all cycles up to and including m^{th} cycle, where m goes from 1 to n, is calculated as

$$\sum_{m=1}^{n} P^{m-1}(1-P) = 1 - P^n,$$

and the number of error-free cycles n is sampled as

$$n = \frac{\ln(1-r)}{\ln P},$$

where r is a uniformly distributed random number in $[0, 1]$. Each time a number n is sampled at least one error is required to be added to the system. We first determine exactly how many errors should be added using the conditional probability of having k errors given that there is at least one error

$$q(k) = \frac{\binom{N}{k} p^k (1-p)^{N-k}}{1-(1-p)^N}.$$

Then we choose k error sites randomly and apply errors to them. At the end of each cycle we check whether a logical error has occurred, or and whether the system has returned to its initial error-free state. If there is a logical error the simulation stops. Alternatively, if the state is error-free, another number n is sampled and the process described above is repeated.

We have checked the reliability of this method by checking that the results agree with those obtained by simulating the full evolution (including error-free cycles) of the BF error-correction circuit in Fig. E.2, which is computationally less demanding than the surface-17 error correction in Fig. E.4.

E.5 Results

The numerical results for the logical-error rate $p_{\log}$ as a function of the physical-error rate p for the BF and surface-17 codes are shown in Fig. E.5(a). The error threshold $p_{\text{th}}^{(\text{X})}$ is

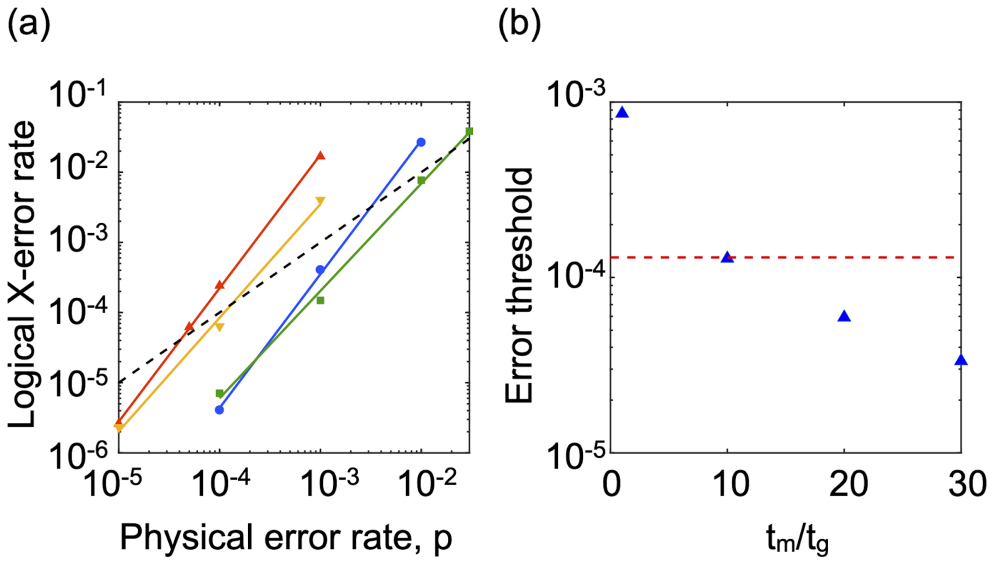

Figure E.5: (a) Numerical results for the logical X error rates $p_{\log}$ for the 1D BF code (blue and green lines), and the 2D surface-17 code, (red and orange lines) with measurement-free QEC and without error correction (black dashed line) as a function of the physical error rate p. The error threshold value is estimated as the value where the physical error rate is equal to the logical error rate. For the BF code, $p_{\text{th,1D}} \approx 3.2 \times 10^{-3}$, and for the 2D surface-17 code, $p_{\text{th,2D}} \approx 4.2 \times 10^{-5}$. The simplified circuits for the BF and surface-17 codes, not including perfect matching (green and orange lines) produce higher thresholds of $p_{\text{th,1D}} \approx 2.0 \times 10^{-2}$. and $p_{\text{th,2D}} \approx 1.3 \times 10^{-4}$. (b) Measurement-based-threshold values, which were simulated here by using the circuit and look-up-table decoder in Ref. [189], for surface-17 code at different measurement time/gate time (t_m/t_g) ratios (blue triangles) in comparison to the measurement-free threshold (red dashed line). Increasing measurement time reduces the error threshold as during the measurement of the ancilla qubits, the data qubits sit idle without protection against errors. When the measurement time vs. gate time ratio is around 10, measurement-free method produces a better threshold than the measurement-based method.

defined as the point where these curves cross the dashed line $p = p_{\log}$ shown in Fig. E.5(a) [1]. Based on these simulations, we estimate threshold values for the BF and surface-17 codes to be 3.2×10^{-3} and 4.2×10^{-5}, respectively. If we remove the portions of the circuit used to implement perfect matching (i.e., the blue boxes in Fig. E.4 and in Fig. E.2) the thresholds for the BF and surface-17 codes improve to 2.0×10^{-2} and 1.3×10^{-4}, respectively, which we attribute to the reduced number of error sites in the simpler scheme, and the fact the simplifications in the circuit do not affect its ability to correct single errors, as discussed in the Appendix. We note that the threshold values reported here correspond to logical X errors, which captures only two out of the three possible logical errors (X,Y and Z) that may occur. In Table E.3, we compare these values to measurement-based results for the same quantity, obtained elsewhere in the literature.

It is important to note that direct comparisons between different QEC schemes, such as those presented in Table E.3, can be complicated by the use of different simulation parameters, such as the logical coding schemes, the error models and the allowed gates. For instance, the measurement-based and measurement-free thresholds for the BF code are the same, however, the error model used in Ref. [188] is slightly different model than the one used in this study.

Table E.3: Comparison of measurement-free thresholds with measurement-based thresholds. The measurement-free BF and surface-17 codes studied here yield thresholds about an order of magnitude lower than their measurement-based counterparts, which we obtain from the literature. We note that the measurement-based threshold for surface-17 code, reported in Ref. [189], was obtained using a look-up-table decoder that is based on a short history of syndromes. It is expected that the threshold obtained with a more sophisticated decoder would be higher [196].

Code	Measurement-based threshold, $p_{\text{th}}^{(X)}$	Measurement-free threshold, $p_{\text{th}}^{(X)}$
Bit-flip	2.0×10^{-2} [188]	2×10^{-2}
Surface-17	8.0×10^{-4} [189]	1.3×10^{-4}

E.6 Discussion

We have described a method of implementing low-distance surface codes on physical systems where measurement times are long but initialization times are short, such as semiconducting quantum dot qubits. In this method, we replace syndrome measurements by a combination of fast re-initialization and unitary gates. We also assume that Toffoli (controlled-controlled-not) and CCZ (controlled-controlled-Z) gates can be implemented efficiently and that fast initialization into the $|0\rangle$ state is available. The method relies on the idea of storing and comparing syndrome information from two consecutive error-correction cycles. We have specifically considered an 11-qubit architecture for a bit-flip (BF) code, and 29 and 25-qubit architectures for a distance-three surface code that employ this method. We have calculated

[1]Note that different definitions for the error threshold exist in the literature. For instance, Crow *et al.* [186] define *threshold* as we do here, whereas in Ref. [189] the term *pseudothreshold* is used, reserving the term *threshold* for the asymptotic threshold as the distance of the code goes to infinity.

the error thresholds for all three of these schemes. A summary of our results along with the corresponding measurement-based thresholds for comparison is given in Table E.3. We note that the, measurement-based threshold for the surface-17 code in this table was calculated using a simplified decoder optimized for limited-memory implementations [189]. It may be possible to obtain a slightly better threshold for the measurement-based case by using a more advanced decoder. Indeed, this was found to be true for the surface-25 code [196].

The method we suggest relies on the fact that the matching process can be simplified for the surface-17 code due to its relatively small size. Although this code is large enough to demonstrate correction of arbitrary errors, it is not large enough to fault-tolerantly implement a universal set of logical gates. To use the measurement-free approach to implement error correction in systems with large numbers of qubits, a creative solution will need to be developed that obviates the need to implement a large-scale classical matching algorithm during the error correction process. However, we believe that even in the absence of such a solution, the method we suggest could be useful for testing the assumptions made for quantum error correction in medium-size experimental systems, before scaling up to the larger systems needed for large-scale quantum computation.

Our results demonstrate that the error threshold for measurement-free error correction for the surface code is less than an order of magnitude lower than for measurement-based schemes. While achieving this threshold will be challenging in the laboratory, the results obtained here clearly become significant in the limit of long measurement times. To demonstrate this, in Fig. E.5(b) we show that when the measurement-time is about 10 times the

gate time, our method begins producing a higher threshold than the measurement-based method. Since the fastest quantum dot spin readout to date is about 100 ns [197], while qubit re-initialization can be as fast as 1 ns [198], measurement-free error correction schemes are clearly of current interest.

The simulations for this work were performed using the University of Wisconsin Center for High Throughput Computing. The authors thank Dan Bradley for his technical support, and M. A. Eriksson, M. Saffman and Yuan-Chi Yang for helpful discussions. The authors acknowledge support from the Vannevar Bush Faculty Fellowship program sponsored by the Basic Research Office of the Assistant Secretary of Defense for Research and Engineering and funded by the Office of Naval Research through grant N00014-15-1-0029.

E.7 Appendix: A comparison of results with and without perfect matching

In this section, we discuss the procedure for removing used syndrome information, which is done to avoid associating a syndrome with multiple error patterns. Although this step is crucial for achieving perfect matching in larger surface codes, in the main text we showed that excluding it actually improves our error threshold. In Fig. E.6, where the three (black) open circles represent data qubits and the four (red) circles below them represent ancilla qubits, we show examples related to the BF code to illustrate that this procedure is only helpful for certain special cases where multiple errors occur, but are not well-separated in

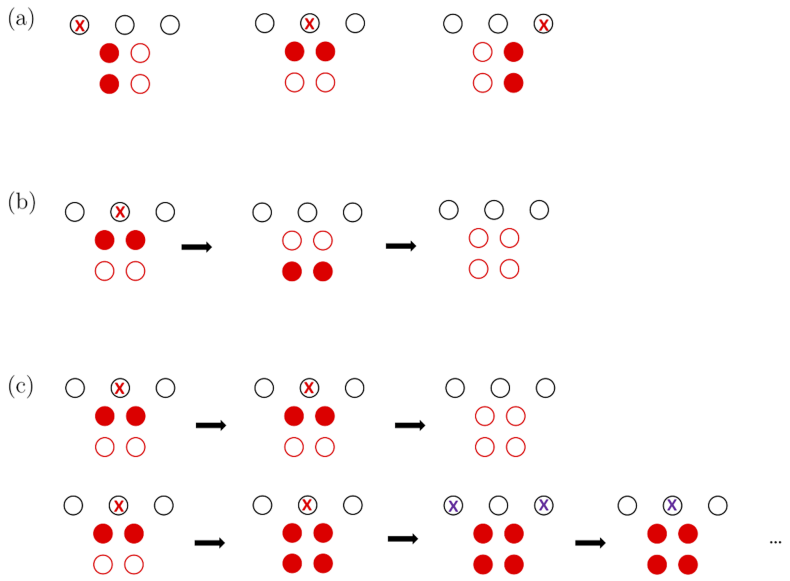

Figure E.6: Examples showing the effect of removing used syndrome information removal in the BF code. The three (black) open circles in the top row represent data qubits. The four (red) circles below the data qubits represent the ancillas, where the middle row corresponds to the first time cycle, while the bottom row corresponds to the second time cycle. Flipped ancillas indicating a syndrome signal are filled and errors on data qubits are denoted with an X. (a) Here we show three different syndrome patterns that trigger different Toffoli gates to correct corresponding data errors. (b) In the case of a single data error, not removing used syndrome information is not harmful. For example, if there is an X error in the middle data qubit there will be two signals in the top row of ancillas, triggering a Toffoli gate that corrects the error. Even if these signals are not removed from the system, they will not trigger other Toffoli gates in the next cycle, and in the following cycle they will disappear completely. (c) We consider a case where errors appear in the middle data qubit in two consecutive time cycles. The first row shows that if the used information is removed both of these errors get corrected. In the second row, however, the information is not removed. This results in signals occurring in all the ancillas in the second cycle, which causes the Toffoli gates to correct errors in all three data qubits. One of these bit flips corrects the actual error, while the other two introduce new errors (shown in purple) resulting in signals in all ancillas in subsequent time cycles. The system then oscillates between having one and two errors indefinitely, making it vulnerable to errors that may occur in the future.

time. Eliminating the perfect-matching steps leaves the system unprotected against certain rare, multiple-error patterns but on the other hand decreases the number of error sites. Figure E.6(a) shows how we visualize the errors and error signals in this figure, when the circuit in Fig. E.2 is implemented. Let the data qubits marked by a red X represent bit-flip errors and let the red filled ancilla qubits represent the error signals that control the error-correcting Toffoli gates. Here, the top row of the ancillas corresponds to results from the first time cycle, while the bottom row corresponds to results of the second time cycle. The three panels indicate that to correct the errors on the right-most and left-most data qubits, two error-correction cycles are needed whereas to correct an error on the middle data qubits only one is needed. In Fig. E.6(b), we consider a situation where removal of the used syndrome information does not benefit us. Specifically, we show three consecutive error-correction cycles, beginning with a single error on the middle data qubit. This error can be corrected in the first cycle as there are already two signals. Although there are still signals in the second cycle, this does not affect data qubits as these signals do not trigger any Toffoli gates. So, this particular error can be corrected without introducing extra errors into the system even when the used syndrome information is not removed. It can easily be seen that this is also the case for the other two possible single data errors. In Fig. E.6(c), we demonstrate an error pattern for which the removal of the used syndrome information is beneficial. In this case, errors occur on the middle data qubit in two consecutive cycles. in the first row, we consider the case where we remove the used syndrome information. Here, the first and second time cycles do not interfere with each other and both of the errors

get corrected. In the second row, we consider the same errors in the case where we do not remove the used syndrome information. Here, the signals in the second cycle trigger all three Toffoli gates. While one of these gates corrects the actual error, the other two introduce new errors (indicated by purple X's) into the data qubits, causing both of the fresh ancillas to signal on a subsequent time cycle. It is easy to see that, in the absence of subsequent errors that would disturb the cycle, the system will now remain in a cycle where the four ancillas repeatedly signal errors and the data qubits oscillate between having one and two errors, failing to return to the error-free state.

Bibliography

[1] R. P. Feynman, "Simulating physics with computers," *International Journal of Theoretical Physics*, vol. 21, no. 6, pp. 467–488, Jun 1982. [Online]. Available: https://doi.org/10.1007/BF02650179

[2] P. Shor, "Polynomial-time algorithms for prime factorization and discrete logarithms on a quantum computer," *SIAM J. Comput.*, vol. 26, no. 5, pp. 1484–1509, Jan 1997.

[3] M. Kjaergaard, M. E. Schwartz, J. Braumller, P. Krantz, J. I.-J. Wang, S. Gustavsson, and W. D. Oliver, "Superconducting qubits: Current state of play," *Annual Review of Condensed Matter Physics*, vol. 11, no. 1, pp. 369–395, 2020. [Online]. Available: https://doi.org/10.1146/annurev-conmatphys-031119-050605

[4] S. Slussarenko and G. J. Pryde, "Photonic quantum information processing: A concise review," *Applied Physics Reviews*, vol. 6, no. 4, p. 041303, 2019. [Online]. Available: https://doi.org/10.1063/1.5115814

[5] C. D. Bruzewicz, J. Chiaverini, R. McConnell, and J. M. Sage, "Trapped-ion quantum computing: Progress and challenges," *Applied Physics Reviews*, vol. 6, no. 2, p. 021314, 2019. [Online]. Available: https://doi.org/10.1063/1.5088164

[6] X. Zhang, H.-O. Li, G. Cao, M. Xiao, G.-C. Guo, and G.-P. Guo, "Semiconductor quantum computation," *National Science Review*, vol. 6, pp. 32–54, dec 2018.

[7] A. Peruzzo, J. McClean, P. Shadbolt, M.-H. Yung, X.-Q. Zhou, P. J. Love, A. Aspuru-Guzik, and J. L. O'Brien, "A variational eigenvalue solver on a photonic quantum processor," *Nature Communications*, vol. 5, no. 1, p. 4213, Jul 2014. [Online]. Available: https://doi.org/10.1038/ncomms5213

[8] E. Farhi, J. Goldstone, and S. Gutmann, "A Quantum Approximate Optimization Algorithm," *arXiv e-prints*, p. arXiv:1411.4028, Nov. 2014.

[9] F. Arute, K. Arya, R. Babbush, D. Bacon, J. C. Bardin, R. Barends, R. Biswas, S. Boixo, F. G. S. L. Brandao, D. A. Buell, B. Burkett, Y. Chen, Z. Chen, B. Chiaro, R. Collins, W. Courtney, A. Dunsworth, E. Farhi, B. Foxen, A. Fowler, C. Gidney, M. Giustina, R. Graff, K. Guerin, S. Habegger, M. P. Harrigan, M. J. Hartmann, A. Ho, M. Hoffmann, T. Huang, T. S. Humble, S. V. Isakov, E. Jeffrey, Z. Jiang,

D. Kafri, K. Kechedzhi, J. Kelly, P. V. Klimov, S. Knysh, A. Korotkov, F. Kostritsa, D. Landhuis, M. Lindmark, E. Lucero, D. Lyakh, S. Mandrà, J. R. McClean, M. McEwen, A. Megrant, X. Mi, K. Michielsen, M. Mohseni, J. Mutus, O. Naaman, M. Neeley, C. Neill, M. Y. Niu, E. Ostby, A. Petukhov, J. C. Platt, C. Quintana, E. G. Rieffel, P. Roushan, N. C. Rubin, D. Sank, K. J. Satzinger, V. Smelyanskiy, K. J. Sung, M. D. Trevithick, A. Vainsencher, B. Villalonga, T. White, Z. J. Yao, P. Yeh, A. Zalcman, H. Neven, and J. M. Martinis, "Quantum supremacy using a programmable superconducting processor," *Nature*, vol. 574, no. 7779, pp. 505–510, Oct 2019. [Online]. Available: https://doi.org/10.1038/s41586-019-1666-5

[10] H.-S. Zhong, H. Wang, Y.-H. Deng, M.-C. Chen, L.-C. Peng, Y.-H. Luo, J. Qin, D. Wu, X. Ding, Y. Hu, P. Hu, X.-Y. Yang, W.-J. Zhang, H. Li, Y. Li, X. Jiang, L. Gan, G. Yang, L. You, Z. Wang, L. Li, N.-L. Liu, C.-Y. Lu, and J.-W. Pan, "Quantum computational advantage using photons," *Science*, vol. 370, no. 6523, pp. 1460–1463, 2020. [Online]. Available: https://science.sciencemag.org/content/370/6523/1460

[11] J. Preskill, "Quantum computing in the nisq era and beyond," *arXiv e-prints*, p. arXiv:1801.00862, Jan. 2018.

[12] A. G. Fowler, M. Mariantoni, J. M. Martinis, and A. N. Cleland, "Surface codes: Towards practical large-scale quantum computation," *Phys. Rev. A*, vol. 86, p. 032324, Sep 2012.

[13] P. W. Shor, "Scheme for reducing decoherence in quantum computer memory," *Phys. Rev. A*, vol. 52, pp. R2493–R2496, Oct 1995. [Online]. Available: https://link.aps.org/doi/10.1103/PhysRevA.52.R2493

[14] A. M. Steane, "Error correcting codes in quantum theory," *Phys. Rev. Lett.*, vol. 77, pp. 793–797, Jul 1996. [Online]. Available: https://link.aps.org/doi/10.1103/PhysRevLett.77.793

[15] T. D. Ladd, F. Jelezko, R. Laflamme, Y. Nakamura, C. Monroe, and J. L. O'Brien, "Quantum computers," *Nature*, vol. 464, no. 7285, pp. 45–53, Mar 2010. [Online]. Available: https://doi.org/10.1038/nature08812

[16] T. Ihn, *Semiconductor Nanostructures: Quantum States and Electronic Transport*. Oxford: Oxford University Press, 2009. [Online]. Available: https://cds.cern.ch/record/1320335

[17] H. Kiyama, A. Korsch, N. Nagai, Y. Kanai, K. Matsumoto, K. Hirakawa, and A. Oiwa, "Single-electron charge sensing in self-assembled quantum dots," *Scientific Reports*, vol. 8, no. 1, p. 13188, Sep 2018. [Online]. Available: https://doi.org/10.1038/s41598-018-31268-x

[18] D. Loss and D. P. DiVincenzo, "Quantum computation with quantum dots," *Phys. Rev. A*, vol. 57, no. 1, pp. 120–126, 1998.

[19] J. Levy, "Universal quantum computation with spin-1/2 pairs and Heisenberg exchange," *Phys. Rev. Lett.*, vol. 89, no. 14, p. 147902, Jan 2002.

[20] J. R. Petta, A. C. Johnson, J. M. Taylor, E. A. Laird, A. Yacoby, M. D. Lukin, C. M. Marcus, M. P. Hanson, and A. C. Gossard, "Coherent manipulation of coupled electron spins in semiconductor quantum dots," *Science*, vol. 309, pp. 2180–2184, 2005.

[21] D. P. DiVincenzo, D. Bacon, J. Kempe, G. Burkard, and K. B. Whaley, "Universal quantum computation with the exchange interaction," *Nature*, vol. 408, no. 6810, p. 339, Nov 2000.

[22] E. A. Laird, J. M. Taylor, D. P. DiVincenzo, C. M. Marcus, M. P. Hanson, and A. C. Gossard, "Coherent spin manipulation in an exchange-only qubit," *Phys. Rev. B*, vol. 82, no. 7, p. 075403, 2010.

[23] T. Hayashi, T. Fujisawa, H. D. Cheong, Y. H. Jeong, and Y. Hirayama, "Coherent manipulation of electronic states in a double quantum dot," *Phys. Rev. Lett.*, vol. 91, p. 226804, 2003.

[24] J. Gorman, D. G. Hasko, and D. A. Williams, "Charge-qubit operation of an isolated double quantum dot," *Phys. Rev. Lett.*, vol. 95, no. 9, Aug 2005.

[25] Z. Shi, C. B. Simmons, D. R. Ward, J. R. Prance, T. S. Koh, J. K. Gamble, X. Wu, D. E. Savage, M. G. Lagally, M. Friesen, S. N. Coppersmith, and M. A. Eriksson, "Coherent quantum oscillations and echo measurements of a Si charge qubit," *Phys. Rev. B*, vol. 88, no. 7, p. 075416, 2013.

[26] D. Kim, D. R. Ward, C. B. Simmons, J. K. Gamble, R. Blume-Kohout, E. Nielsen, D. E. Savage, M. G. Lagally, M. Friesen, S. N. Coppersmith, and M. A. Eriksson, "Microwave-driven coherent operations of a semiconductor quantum dot charge qubit," *Nat. Nanotechnol.*, vol. 10, pp. 243–247, 2015.

[27] Z. Shi, C. B. Simmons, J. R. Prance, J. K. Gamble, T. S. Koh, Y.-P. Shim, X. Hu, D. E. Savage, M. G. Lagally, M. A. Eriksson, M. Friesen, and S. N. Coppersmith, "Fast hybrid silicon double-quantum-dot qubit," *Phys. Rev. Lett.*, vol. 108, p. 140503, 2012.

[28] T. S. Koh, J. K. Gamble, M. Friesen, M. A. Eriksson, and S. N. Coppersmith, "Pulse-gated quantum dot hybrid qubit," *Phys. Rev. Lett.*, vol. 109, p. 250503, 2012.

[29] D. Kim, Z. Shi, C. B. Simmons, D. R. Ward, J. R. Prance, T. S. Koh, J. K. Gamble, D. E. Savage, M. G. Lagally, M. Friesen, S. N. Coppersmith, and M. A. Eriksson, "Quantum control and process tomography of a semiconductor quantum dot hybrid qubit," *Nature*, vol. 511, pp. 70–74, 2014.

[30] U. Meirav, M. A. Kastner, and S. J. Wind, "Single-electron charging and periodic conductance resonances in gaas nanostructures," *Phys. Rev. Lett.*, vol. 65, no. 6, pp. 771–774, Aug 1990.

[31] F. A. Zwanenburg, A. S. Dzurak, A. Morello, M. Y. Simmons, L. C. L. Hollenberg, G. Klimeck, S. Rogge, S. N. Coppersmith, and M. A. Eriksson, "Silicon quantum electronics," *Rev. Mod. Phys.*, vol. 85, p. 961, 2013.

[32] C. Yannouleas and U. Landman, "Spontaneous symmetry breaking in single and molecular quantum dots," *Phys. Rev. Lett.*, vol. 82, no. 26, p. 5325, June 1999.

[33] B. Reusch, W. Häusler, and H. Grabert, "Wigner molecules in quantum dots," *Phys. Rev. B*, vol. 63, p. 113313, 2001.

[34] R. Egger, W. Häusler, C. H. Mak, and H. Grabert, "Crossover from fermi liquid to wigner molecule behavior in quantum dots," *Phys. Rev. Lett.*, vol. 82, pp. 3320–3323, Apr 1999. [Online]. Available: https://link.aps.org/doi/10.1103/PhysRevLett.82.3320

[35] C. Ellenberger, T. Ihn, C. Yannouleas, U. Landman, K. Ensslin, D. Driscoll, and A. C. Gossard, "Excitation spectrum of two correlated electrons in a lateral quantum dot with negligible zeeman splitting," *Phys. Rev. Lett.*, vol. 96, p. 126806, 2006.

[36] M. Friesen, S. Chutia, C. Tahan, and S. N. Coppersmith, "Valley splitting theory of SiGe/Si/SiGe quantum wells," *Phys. Rev. B*, vol. 75, p. 115318, 2007.

[37] M. Friesen and S. N. Coppersmith, "Theory of valley-orbit coupling in a Si/SiGe quantum dot," *Phys. Rev. B*, vol. 81, no. 11, p. 115324, 2010.

[38] M. G. Borselli, K. Eng, E. T. Croke, B. M. Maune, B. Huang, R. S. Ross, A. A. Kiselev, P. W. Deelman, I. Alvarado-Rodriguez, A. E. Schmitz, M. Sokolich, K. S. Holabird, T. M. Hazard, M. F. Gyure, and A. T. Hunter, "Pauli spin blockade in undoped Si/SiGe two-electron double quantum dots," *Appl. Phys. Lett.*, vol. 99, p. 063109, 2011.

[39] M. Veldhorst, C. H. Yang, J. C. C. Hwang, W. Huang, J. P. Dehollain, J. T. Muhonen, S. Simmons, A. Laucht, F. E. Hudson, K. M. Itoh, A. Morello, and A. S. Dzurak, "A two-qubit logic gate in silicon," *Nature*, vol. 526, p. 410, 2015.

[40] T. F. Watson, S. G. J. Philips, E. Kawakami, D. R. Ward, P. Scarlino, M. Veldhorst, D. E. Savage, M. G. Lagally, M. Friesen, S. N. Coppersmith, M. A. Eriksson, and L. M. K. Vandersypen, "A programmable two-qubit quantum processor in silicon," *Nature*, vol. 555, p. 633, 2018.

[41] R. W. Andrews, C. Jones, M. D. Reed, A. M. Jones, S. D. Ha, M. P. Jura, J. Kerckhoff, M. Levendorf, S. Meenehan, S. T. Merkel, A. Smith, B. Sun, A. J. Weinstein, M. T. Rakher, T. D. Ladd, and M. G. Borselli, "Quantifying error and leakage in an encoded Si/SiGe triple-dot qubit," *Nature Nanotechnology*, vol. 14, no. 8, pp. 747–750, Jul. 2019.

[42] P. Harvey-Collard, N. T. Jacobson, C. Bureau-Oxton, R. M. Jock, V. Srinivasa, A. M. Mounce, D. R. Ward, J. M. Anderson, R. P. Manginell, J. R. Wendt, T. Pluym, M. P. Lilly, D. R. Luhman, M. Pioro-Ladrière, and M. S. Carroll, "Spin-orbit interactions for singlet-triplet qubits in silicon," *Phys. Rev. Lett.*, vol. 122, p. 217702, May 2019.

[43] F. Borjans, X. G. Croot, X. Mi, M. J. Gullans, and J. R. Petta, "Resonant microwave-mediated interactions between distant electron spins," *Nature*, vol. 577, no. 7789, pp. 195–198, Jan 2020.

[44] S. J. Angus, A. J. Ferguson, A. S. Dzurak, and R. G. Clark, "Gate-defined quantum dots in intrinsic silicon," *Nano Lett.*, vol. 7, pp. 2051–2055, Jan 2007.

[45] D. M. Zajac, T. M. Hazard, X. Mi, K. Wang, and J. R. Petta, "A reconfigurable gate architecture for Si/SiGe quantum dots," *Appl. Phys. Lett.*, vol. 106, p. 223507, 2015.

[46] D. M. Zajac, T. M. Hazard, X. Mi, E. Nielsen, and J. R. Petta, "Scalable gate architecture for a one-dimensional array of semiconductor spin qubits," *Phys. Rev. Appl.*, vol. 6, p. 054013, 2016.

[47] X. Mi, M. Benito, S. Putz, D. M. Zajac, J. M. Taylor, G. Burkard, and J. R. Petta, "A coherent spin–photon interface in silicon," *Nature*, vol. 555, p. 599, 2018.

[48] D. M. Zajac, A. J. Sigillito, M. Russ, F. Borjans, J. M. Taylor, G. Burkard, and J. R. Petta, "Resonantly driven CNOT gate for electron spins," *Science*, vol. 359, p. 439, 2018.

[49] S. F. Neyens, E. MacQuarrie, J. Dodson, J. Corrigan, N. Holman, B. Thorgrimsson, M. Palma, T. McJunkin, L. Edge, M. Friesen, S. Coppersmith, and M. Eriksson, "Measurements of capacitive coupling within a quadruple-quantum-dot array," *Phys. Rev. Applied*, vol. 12, p. 064049, Dec 2019.

[50] T. Kodera, K. Ono, S. Amaha, Y. Arakawa, and S. Tarucha, "Pauli-spin blockade in a vertical double quantum dot holding two to five electrons," *Journal of Physics: Conference Series*, vol. 150, no. 2, p. 022043, feb 2009. [Online]. Available: https://doi.org/10.1088%2F1742-6596%2F150%2F2%2F022043

[51] B.-B. Chen, B.-C. Wang, G. Cao, H.-O. Li, M. Xiao, G.-C. Guo, H.-W. Jiang, X. Hu, and G.-P. Guo, "Spin blockade and coherent dynamics of high-spin states in a three-electron double quantum dot," *Phys. Rev. B*, vol. 95, p. 035408, Jan 2017. [Online]. Available: https://link.aps.org/doi/10.1103/PhysRevB.95.035408

[52] P. Harvey-Collard, N. T. Jacobson, M. Rudolph, J. Dominguez, G. A. Ten Eyck, J. R. Wendt, T. Pluym, J. K. Gamble, M. P. Lilly, M. Pioro-Ladrière, and M. S. Carroll, "Coherent coupling between a quantum dot and a donor in silicon," *Nature Commun.*, vol. 8, no. 1, p. 1029, 2017.

[53] R. C. C. Leon, C. H. Yang, J. C. C. Hwang, J. C. Lemyre, T. Tanttu, W. Huang, K. W. Chan, K. Y. Tan, F. E. Hudson, K. M. Itoh, A. Morello, A. Laucht, M. Pioro-Ladrière, A. Saraiva, and A. S. Dzurak, "Coherent spin control of s-, p-, d- and f-electrons in a silicon quantum dot," *Nature Communications*, vol. 11, no. 1, p. 797, Feb 2020. [Online]. Available: https://doi.org/10.1038/s41467-019-14053-w

[54] C. H. Yang, R. C. C. Leon, J. C. C. Hwang, A. Saraiva, T. Tanttu, W. Huang, J. Camirand Lemyre, K. W. Chan, K. Y. Tan, F. E. Hudson, K. M. Itoh, A. Morello, M. Pioro-Ladrière, A. Laucht, and A. S. Dzurak, "Operation of a silicon quantum processor unit cell above one kelvin," *Nature*, vol. 580, no. 7803, pp. 350–354, Apr 2020. [Online]. Available: https://doi.org/10.1038/s41586-020-2171-6

[55] L. Petit, H. G. J. Eenink, M. Russ, W. I. L. Lawrie, N. W. Hendrickx, S. G. J. Philips, J. S. Clarke, L. M. K. Vandersypen, and M. Veldhorst, "Universal quantum logic in hot silicon qubits," *Nature*, vol. 580, pp. 355–359, 2020.

[56] G. W. Bryant, "Electronic structure of ultrasmall quantum-well boxes," *Phys. Rev. Lett.*, vol. 59, no. 10, p. 1140, Sept 1987.

[57] A. V. Filinov, M. Bonitz, and Y. E. Lozovik, "Wigner crystallization in mesoscopic 2d electron systems," *Phys. Rev. Lett.*, vol. 86, pp. 3851–3854, Apr 2001. [Online]. Available: https://link.aps.org/doi/10.1103/PhysRevLett.86.3851

[58] E. Wigner, "On the interaction of electrons in metals," *Phys. Rev.*, vol. 46, pp. 1002–1011, Dec 1934. [Online]. Available: https://link.aps.org/doi/10.1103/PhysRev.46.1002

[59] B. Tanatar and D. M. Ceperley, "Ground state of the two-dimensional electron gas," *Phys. Rev. B*, vol. 39, pp. 5005–5016, Mar 1989. [Online]. Available: https://link.aps.org/doi/10.1103/PhysRevB.39.5005

[60] A. Singha, V. Pellegrini, A. Pinczuk, L. N. Pfeiffer, K. W. West, and M. Rontani, "Correlated electrons in optically tunable quantum dots: Building an electron dimer molecule," *Phys. Rev. Lett.*, vol. 104, no. 24, p. 246802, June 2010.

[61] S. Pecker, F. Kuemmeth, A. Secchi, M. Rontani, D. C. Ralph, P. L. McEuen, and S. Ilani, "Observation and spectroscopy of a two-electron wigner molecule in an ultraclean carbon nanotube," *Nature Physics*, vol. 9, no. 9, pp. 576–581, Sep 2013. [Online]. Available: https://doi.org/10.1038/nphys2692

[62] T. B. Boykin, G. Klimeck, M. A. Eriksson, M. Friesen, S. N. Coppersmith, P. von Allmen, F. Oyafuso, and S. Lee, "Valley splitting in strained silicon quantum wells," *Appl. Phys. Lett.*, vol. 84, pp. 115–117, 2004.

[63] S. Goswami, K. A. Slinker, M. Friesen, L. M. McGuire, J. L. Truitt, C. Tahan, L. J. Klein, J. O. Chu, P. M. Mooney, D. W. van der Weide, R. Joynt, S. N. Coppersmith, and M. A. Eriksson, "Controllable valley splitting in silicon quantum devices," *Nat. Phys.*, vol. 3, pp. 41–45, 2007.

[64] S. Chutia, S. N. Coppersmith, and M. Friesen, "Multiscale theory of valley splitting in the conduction band of a quantum well," *Phys Rev B*, vol. 77, no. 19, p. 193311, 2008.

[65] M. Friesen, M. A. Eriksson, and S. N. Coppersmith, "Magnetic field dependence of valley splitting in realistic Si/SiGe quantum wells," *Appl. Phys. Lett.*, vol. 89, p. 202106, 2006.

[66] N. Kharche, M. Prada, T. B. Boykin, and G. Klimeck, "Valley splitting in strained silicon quantum wells modeled with 2 ° miscuts, step disorder, and alloy disorder," *Appl. Phys. Lett.*, vol. 90, no. 9, p. 092109, Jan 2007.

[67] D. Culcer, X. Hu, and S. Das Sarma, "Interface roughness, valley-orbit coupling, and valley manipulation in quantum dots," *Phys. Rev. B*, vol. 82, p. 205315, 2010.

[68] J. K. Gamble, M. A. Eriksson, S. N. Coppersmith, and M. Friesen, "Disorder-induced valley-orbit hybrid states in Si quantum dots," *Phys. Rev. B*, vol. 88, p. 035310, 2013.

[69] P. Boross, G. Széchenyi, D. Culcer, and A. Pályi, "Control of valley dynamics in silicon quantum dots in the presence of an interface step," *Physical Review B*, vol. 94, no. 3, p. 035438, 2016.

[70] B. Tariq and X. Hu, "Effects of interface steps on the valley-orbit coupling in a si/sige quantum dot," *Phys. Rev. B*, vol. 100, p. 125309, Sep 2019.

[71] A. Hosseinkhani and G. Burkard, "Electromagnetic control of valley splitting in ideal and disordered si quantum dots," *Phys. Rev. Research*, vol. 2, p. 043180, Nov 2020.

[72] Y. Hada and M. Eto, "Electronic states in silicon quantum dots: Multivalley artificial atoms," *Phys. Rev. B*, vol. 68, p. 155322, Oct 2003. [Online]. Available: https://link.aps.org/doi/10.1103/PhysRevB.68.155322

[73] L. Jiang, C. H. Yang, Z. Pan, A. Rossi, A. S. Dzurak, and D. Culcer, "Coulomb interaction and valley-orbit coupling in si quantum dots," *Phys. Rev. B*, vol. 88, p. 085311, Aug 2013. [Online]. Available: https://link.aps.org/doi/10.1103/PhysRevB.88.085311

[74] D. Miserev and O. P. Sushkov, "Prediction of the spin triplet two-electron quantum dots in si: Towards controlled quantum simulations of magnetic systems," *Phys. Rev. B*, vol. 100, p. 205129, Nov 2019. [Online]. Available: https://link.aps.org/doi/10.1103/PhysRevB.100.205129

[75] L. Wang, K. Shen, B. Y. Sun, and M. W. Wu, "Singlet-triplet relaxation in multivalley silicon single quantum dots," *Phys. Rev. B*, vol. 81, p. 235326, Jun 2010. [Online]. Available: https://link.aps.org/doi/10.1103/PhysRevB.81.235326

[76] Z. Liu, L. Wang, and K. Shen, "Energy spectra of three electrons in si/sige single and vertically coupled double quantum dots," *Phys. Rev. B*, vol. 85, p. 045311, Jan 2012. [Online]. Available: https://link.aps.org/doi/10.1103/PhysRevB.85.045311

[77] N. Shaji, C. B. Simmons, M. Thalakulam, L. J. Klein, H. Qin, H. Luo, D. E. Savage, M. G. Lagally, A. J. Rimberg, R. Joynt, M. Friesen, R. H. Blick, S. N. Coppersmith, and M. A. Eriksson, "Spin blockade and lifetime-enhanced transport in a few-electron Si/SiGe double quantum dot," *Nat. Phys.*, vol. 4, no. 7, pp. 540–544, 2008.

[78] E. Ferraro, M. De Michielis, G. Mazzeo, M. Fanciulli, and E. Prati, "Effective hamiltonian for the hybrid double quantum dot qubit," *Quantum Information Processing*, vol. 13, no. 5, pp. 1155–1173, 2014.

[79] D. Kim, D. R. Ward, C. B. Simmons, D. E. Savage, M. G. Lagally, M. Friesen, S. N. Coppersmith, and M. A. Eriksson, "High-fidelity resonant gating of a silicon-based quantum dot hybrid qubit," *npj Quantum Inf.*, vol. 1, p. 15004, 2015.

[80] G. Cao, H.-O. Li, G.-D. Yu, B.-C. Wang, B.-B. Chen, X.-X. Song, M. Xiao, G.-C. Guo, H.-W. Jiang, X. Hu, and G.-P. Guo, "Tunable hybrid qubit in a GaAs double quantum dot," *Phys. Rev. Lett.*, vol. 116, no. 8, p. 086801, 2016.

[81] B. Thorgrimsson, D. Kim, Y.-C. Yang, L. W. Smith, C. B. Simmons, D. R. Ward, R. H. Foote, J. Corrigan, D. E. Savage, M. G. Lagally, M. Friesen, S. N. Coppersmith, and M. A. Eriksson, "Extending the coherence of a quantum dot hybrid qubit," *npj Quantum Inf.*, vol. 3, p. 32, 2017.

[82] J. Corrigan, J. P. Dodson, H. Ekmel Ercan, J. C. Abadillo-Uriel, B. Thorgrimsson, T. J. Knapp, N. Holman, T. McJunkin, S. F. Neyens, E. R. MacQuarrie, R. H. Foote, L. F. Edge, M. Friesen, S. N. Coppersmith, and M. A. Eriksson, "Coherent control and spectroscopy of a semiconductor quantum dot Wigner molecule," *arXiv e-prints*, p. arXiv:2009.13572, Sep. 2020.

[83] W. Jang, M.-K. Cho, H. Jang, J. Kim, J. Park, H. Jung, V. Umansky, and D. Kim, "Single-shot readout of a driven hybrid qubit in a GaAs double quantum dot," *arXiv e-prints*, p. arXiv:2101.11864, Jan. 2021.

[84] L. Gaudreau, G. Granger, A. Kam, G. C. Aers, S. A. Studenikin, P. Zawadzki, M. Pioro-Ladrière, Z. R. Wasilewski, and A. S. Sachrajda, "Coherent control of three-spin states in a triple quantum dot," *Nat. Phys.*, vol. 8, pp. 54–58, 2011.

[85] B. M. Maune, M. G. Borselli, B. Huang, T. D. Ladd, P. W. Deelman, K. S. Holabird, A. A. Kiselev, I. Alvarado-Rodriguez, R. S. Ross, A. E. Schmitz, M. Sokolich, C. A. Watson, M. F. Gyure, and A. T. Hunter, "Coherent singlet-triplet oscillations in a silicon-based double quantum dot," *Nature*, vol. 481, no. 7381, pp. 344–347, 2012.

[86] J. Medford, J. Beil, J. M. Taylor, E. I. Rashba, H. Lu, A. C. Gossard, and C. M. Marcus, "Quantum-dot-based resonant exchange qubit," *Phys. Rev. Lett.*, vol. 111, p. 050501, Jul 2013.

[87] R. Li, L. Petit, D. P. Franke, J. P. Dehollain, J. Helsen, M. Steudtner, N. K. Thomas, Z. R. Yoscovits, K. J. Singh, S. Wehner, L. M. K. Vandersypen, J. S. Clarke, and M. Veldhorst, "A crossbar network for silicon quantum dot qubits," *Science Advances*, vol. 4, p. 7, 2018.

[88] T. B. Boykin, G. Klimeck, M. Friesen, S. N. Coppersmith, P. vonAllmen, F. Oyafuso, and S. Lee, "Valley splitting in low-density quantum-confined heterostructures studied using tight-binding models," *Phys. Rev. B*, vol. 70, p. 165325, Jan 2004.

[89] J. C. Abadillo-Uriel, B. Thorgrimsson, D. Kim, L. W. Smith, C. B. Simmons, D. R. Ward, R. H. Foote, J. Corrigan, D. E. Savage, M. G. Lagally, M. J. Calderón, S. N. Coppersmith, M. A. Eriksson, and M. Friesen, "Signatures of atomic-scale structure in the energy dispersion and coherence of a si quantum-dot qubit," *Phys. Rev. B*, vol. 98, p. 165438, Oct 2018. [Online]. Available: https://link.aps.org/doi/10.1103/PhysRevB.98.165438

[90] J. P. Dodson, H. Ekmel Ercan, J. Corrigan, M. Losert, N. Holman, T. McJunkin, L. F. Edge, M. Friesen, S. N. Coppersmith, and M. A. Eriksson, "How valley-orbit states in silicon quantum dots probe quantum well interfaces," *arXiv e-prints*, p. arXiv:2103.14702, Mar. 2021.

[91] R. A. Faulkner, "Higher donor excited states for prolate-spheroid conduction bands: A reevaluation of silicon and germanium," *Phys. Rev.*, vol. 184, pp. 713–721, Aug 1969. [Online]. Available: https://link.aps.org/doi/10.1103/PhysRev.184.713

[92] A. Szabó and N. Ostlund, *Modern Quantum Chemistry: Introduction to Advanced Electronic Structure Theory*. Macmillan, 1982. [Online]. Available: https://books.google.com/books?id=1ky8QgAACAAJ

[93] X. Hu and S. Das Sarma, "Hilbert-space structure of a solid-state quantum computer: Two-electron states of a double-quantum-dot artificial molecule," *Phys. Rev. A*, vol. 61, p. 062301, May 2000.

[94] S. M. Reimann and M. Manninen, "Electronic structure of quantum dots," *Rev. Mod. Phys.*, vol. 74, pp. 1283–1342, Nov 2002. [Online]. Available: https://link.aps.org/doi/10.1103/RevModPhys.74.1283

[95] M. Friesen, P. Rugheimer, D. E. Savage, M. G. Lagally, D. W. van der Weide, R. Joynt, and M. A. Eriksson, "Practical design and simulation of silicon-based quantum-dot qubits," *Phys. Rev. B*, vol. 67, p. 121301, 2003.

[96] M. Korkusinski, I. P. Gimenez, P. Hawrylak, L. Gaudreau, S. A. Studenikin, and A. S. Sachrajda, "Topological hunds rules and the electronic properties of a triple lateral quantum dot molecule," *Phys. Rev. B*, vol. 75, p. 115301, Mar 2007. [Online]. Available: https://link.aps.org/doi/10.1103/PhysRevB.75.115301

[97] E. Nielsen, R. W. Young, R. P. Muller, and M. S. Carroll, "Implications of simultaneous requirements for low-noise exchange gates in double quantum dots," *Phys. Rev. B*, vol. 82, p. 075319, Aug 2010. [Online]. Available: https://link.aps.org/doi/10.1103/PhysRevB.82.075319

[98] E. Barnes, J. P. Kestner, N. T. T. Nguyen, and S. Das Sarma, "Screening of charged impurities with multielectron singlet-triplet spin qubits in quantum dots," *Phys. Rev. B*, vol. 84, p. 235309, Dec 2011. [Online]. Available: https://link.aps.org/doi/10.1103/PhysRevB.84.235309

[99] E. Nielsen, R. Rahman, and R. P. Muller, "A many-electron tight binding method for the analysis of quantum dot systems," *Journal of Applied Physics*, vol. 112, no. 11, p. 114304, 2012. [Online]. Available: https://doi.org/10.1063/1.4759256

[100] M. A. Bakker, S. Mehl, T. Hiltunen, A. Harju, and D. P. DiVincenzo, "Validity of the single-particle description and charge noise resilience for multielectron quantum dots," *Phys. Rev. B*, vol. 91, p. 155425, Apr 2015. [Online]. Available: https://link.aps.org/doi/10.1103/PhysRevB.91.155425

[101] A. Pan, T. E. Keating, M. F. Gyure, E. J. Pritchett, S. Quinn, R. S. Ross, T. D. Ladd, and J. Kerckhoff, "Resonant exchange operation in triple-quantum-dot qubits for spin–photon transduction," *Quantum Science and Technology*, vol. 5, no. 3, p. 034005, may 2020. [Online]. Available: https://doi.org/10.1088/2058-9565/ab86c9

[102] B. Buonacorsi, M. Korkusinski, B. Khromets, and J. Baugh, "Optimizing lateral quantum dot geometries for reduced exchange noise," *arXiv e-prints*, p. arXiv:2012.10512, Dec. 2020.

[103] L. Füsti-Molnar and P. Pulay, "Accurate molecular integrals and energies using combined plane wave and gaussian basis sets in molecular electronic structure theory," *The Journal of Chemical Physics*, vol. 116, no. 18, pp. 7795–7805, 2002. [Online]. Available: https://doi.org/10.1063/1.1467901

[104] E. H. Chen, K. Raach, A. Pan, A. A. Kiselev, E. Acuna, J. Z. Blumoff, T. Brecht, M. Choi, W. Ha, D. Hulbert, M. P. Jura, T. Keating, R. Noah, B. Sun, B. J. Thomas, M. Borselli, C. A. C. Jackson, M. T. Rakher, and R. S. Ross, "Detuning axis

pulsed spectroscopy of valley-orbital states in si/sige quantum dots," *arXiv e-prints*, p. arXiv:2010.04818, Oct. 2020.

[105] C. H. Yang, W. H. Lim, N. S. Lai, A. Rossi, A. Morello, and A. S. Dzurak, "Orbital and valley state spectra of a few-electron silicon quantum dot," *Phys. Rev. B*, vol. 86, p. 115319, Sep 2012.

[106] K. Takeda, T. Obata, Y. Fukuoka, W. M. Akhtar, J. Kamioka, T. Kodera, S. Oda, and S. Tarucha, "Characterization and suppression of low-frequency noise in si/sige quantum point contacts and quantum dots," *Applied Physics Letters*, vol. 102, p. 123113, 2013.

[107] J. P. Dodson, N. Holman, B. Thorgrimsson, S. F. Neyens, E. F. MacQuarrie, T. McJunkin, R. H. Foote, L. F. Edge, S. N. Coppersmith, and M. A. Eriksson, "Fabrication process and failure analysis for robust quantum dots in silicon," *Nanotechnology*, vol. 31, p. 505001, 2020.

[108] M. Veldhorst, J. C. C. Hwang, C. H. Yang, A. W. Leenstra, B. de Ronde, J. P. Dehollain, J. T. Muhonen, F. E. Hudson, K. M. Itoh, A. Morello, and A. S. Dzurak, "An addressable quantum dot qubit with fault-tolerant control-fidelity," *Nat. Nanotechnol.*, vol. 9, no. 12, pp. 981–985, 2014.

[109] R. M. Jock, N. T. Jacobson, P. Harvey-Collard, A. M. Mounce, V. Srinivasa, D. R. Ward, J. Anderson, R. Manginell, J. R. Wendt, M. Rudolph, T. Pluym, J. K. Gamble, A. D. Baczewski, W. M. Witzel, and M. S. Carroll, "A silicon metal-oxide-semiconductor electron spin-orbit qubit," *Nature Communications*, vol. 9, no. 1, May 2018.

[110] S. Bosco, B. Hetényi, and D. Loss, "Hole spin qubits in Si finfets with fully tunable spin-orbit coupling and sweet spots for charge noise," *PRX Quantum*, vol. 2, p. 010348, Mar 2021. [Online]. Available: https://link.aps.org/doi/10.1103/PRXQuantum.2.010348

[111] L. C. Camenzind, S. Geyer, A. Fuhrer, R. J. Warburton, D. M. Zumbühl, and A. V. Kuhlmann, "A spin qubit in a fin field-effect transistor," *arXiv e-prints*, p. arXiv:2103.07369, Mar. 2021.

[112] X. Hu and S. Das Sarma, "Charge-fluctuation-induced dephasing of exchange-coupled spin qubits," *Phys. Rev. Lett.*, vol. 96, p. 100501, Mar 2006.

[113] O. E. Dial, M. D. Shulman, S. P. Harvey, H. Bluhm, V. Umansky, and A. Yacoby, "Charge noise spectroscopy using coherent exchange oscillations in a singlet-triplet qubit," *Phys. Rev. Lett.*, vol. 110, p. 146804, 2013.

[114] E. J. Connors, J. Nelson, H. Qiao, L. F. Edge, and J. M. Nichol, "Low-frequency charge noise in si/sige quantum dots," *Physical Review B*, vol. 100, no. 16, p. 165305, 2019.

[115] M. G. Borselli, K. Eng, R. S. Ross, T. M. Hazard, K. S. Holabird, B. Huang, A. A. Kiselev, P. W. Deelman, L. D. Warren, I. Milosavljevic, A. E. Schmitz, M. Sokolich, M. F. Gyure, and A. T. Hunter, "Undoped accumulation-mode si/sige quantum dots," *Nanotechnology*, vol. 26, p. 375202, 2015.

[116] L. Kranz, S. K. Gorman, B. Thorgrimsson, Y. He, D. Keith, J. G. Keizer, and M. Y. Simmons, "Exploiting a single-crystal environment to minimize the charge noise on qubits in silicon," *Advanced Materials*, vol. 32, no. 40, p. 2003361, 2020. [Online]. Available: https://onlinelibrary.wiley.com/doi/abs/10.1002/adma.202003361

[117] K. Khodjasteh and D. A. Lidar, "Fault-tolerant quantum dynamical decoupling," *Physical Review Letters*, vol. 95, no. 18, p. 180501, 2005.

[118] X. Wang, L. S. Bishop, E. Barnes, J. P. Kestner, and S. D. Sarma, "Robust quantum gates for singlet-triplet spin qubits using composite pulses," *Phys. Rev. A*, vol. 89, p. 022310, Feb 2014. [Online]. Available: https://link.aps.org/doi/10.1103/PhysRevA.89.022310

[119] Y.-C. Yang, S. N. Coppersmith, and M. Friesen, "Achieving high-fidelity single-qubit gates in a strongly driven charge qubit with 1/f charge noise," *npj Quantum Information*, vol. 5, no. 1, p. 12, dec 2019.

[120] J. M. Taylor, V. Srinivasa, and J. Medford, "Electrically protected resonant exchange qubits in triple quantum dots," *Phys. Rev. Lett.*, vol. 111, no. 5, p. 050502, 2013.

[121] J. Fei, J.-T. Hung, T. S. Koh, Y.-P. Shim, S. N. Coppersmith, X. Hu, and M. Friesen, "Characterizing gate operations near the sweet spot of an exchange-only qubit," *Physical Review B*, vol. 91, no. 20, p. 205434, 2015.

[122] M. Reed, B. Maune, R. Andrews, M. Borselli, K. Eng, M. Jura, A. Kiselev, T. Ladd, S. Merkel, I. Milosavljevic *et al.*, "Reduced sensitivity to charge noise in semiconductor spin qubits via symmetric operation," *Phys. Rev. Lett.*, vol. 116, no. 11, p. 110402, 2016.

[123] F. Martins, F. K. Malinowski, P. D. Nissen, E. Barnes, S. Fallahi, G. C. Gardner, M. J. Manfra, C. M. Marcus, and F. Kuemmeth, "Noise suppression using symmetric exchange gates in spin qubits," *Phys. Rev. Lett.*, vol. 116, no. 11, p. 116801, 2016.

[124] Y.-P. Shim and C. Tahan, "Charge-noise-insensitive gate operations for always-on, exchange-only qubits," *Phys. Rev. B*, vol. 93, no. 12, p. 121410, 2016.

[125] G. Zhang, Y. Liu, J. J. Raftery, and A. A. Houck, "Suppression of photon shot noise dephasing in a tunable coupling superconducting qubit," *npj Quantum Information*, vol. 3, no. 1, p. 1, Jan 2017. [Online]. Available: https://doi.org/10.1038/s41534-016-0002-2

[126] J. C. Abadillo-Uriel, M. A. Eriksson, S. N. Coppersmith, and M. Friesen, "Enhancing the dipolar coupling of a s-t0 qubit with a transverse sweet spot," *Nature Communications*, vol. 10, no. 1, p. 5641, Dec 2019. [Online]. Available: https://doi.org/10.1038/s41467-019-13548-w

[127] A. P. Higginbotham, F. Kuemmeth, M. P. Hanson, A. C. Gossard, and C. M. Marcus, "Coherent operations and screening in multielectron spin qubits," *Physical Review Letters*, vol. 112, no. 2, p. 026801, 2014.

[128] S. Mehl and D. P. DiVincenzo, "Noise-protected gate for six-electron double-dot qubit," *Phys. Rev. B*, vol. 88, p. 161408, Oct 2013. [Online]. Available: https://link.aps.org/doi/10.1103/PhysRevB.88.161408

[129] M. G. Borselli, R. S. Ross, A. A. Kiselev, E. T. Croke, K. S. Holabird, P. W. Deelman, L. D. Warren, I. Alvarado-Rodriguez, I. Milosavljevic, F. C. Ku, W. S. Wong, A. E. Schmitz, M. Sokolich, M. F. Gyure, and A. T. Hunter, "Measurement of valley splitting in high-symmetry si/sige quantum dots," *Appl. Phys. Lett.*, vol. 98, no. 12, p. 123118, Jan 2011.

[130] X. Mi, C. G. Péterfalvi, G. Burkard, and J. R. Petta, "High-resolution valley spectroscopy of si quantum dots," *Phys. Rev. Lett.*, vol. 119, p. 176803, Oct 2017.

[131] J. S. Schoenfield, B. M. Freeman, and H. Jiang, "Coherent manipulation of valley states at multiple charge configurations of a silicon quantum dot device," *Nature Commun.*, vol. 8, no. 1, p. 64, 2017.

[132] K. Takeda, J. Yoneda, T. Otsuka, T. Nakajima, M. R. Delbecq, G. Allison, Y. Hoshi, N. Usami, K. M. Itoh, S. Oda, T. Kodera, and S. Tarucha, "Optimized electrical control of a si/sige spin qubit in the presence of an induced frequency shift," *npj Quantum Information*, vol. 4, no. 1, p. 54, Oct 2018. [Online]. Available: https://doi.org/10.1038/s41534-018-0105-z

[133] J. D. Jackson, *Classical electrodynamics*, 3rd ed. New York, NY: Wiley, 1999. [Online]. Available: http://cdsweb.cern.ch/record/490457

[134] T. Takashima and R. Ishibashi, "Electric fields in dielectric multi-layers calculated by digital computer," *IEEE Transactions on Electrical Insulation*, vol. EI-13, pp. 37–44, 1978.

[135] X. Wu, D. R. Ward, J. R. Prance, D. Kim, J. K. Gamble, R. T. Mohr, Z. Shi, D. E. Savage, M. G. Lagally, M. Friesen, S. N. Coppersmith, and M. A. Eriksson, "Two-axis control of singlet-triplet qubit with an integrated micromagnet," *PNAS*, vol. 111, p. 11938, 2014.

[136] X. Mi, S. Kohler, and J. R. Petta, "Landau-zener interferometry of valley-orbit states in Si/SiGe double quantum dots," *Phys. Rev. B*, vol. 98, p. 161404, Oct 2018.

[137] K. D. Petersson, J. R. Petta, H. Lu, and A. C. Gossard, "Quantum coherence in a one-electron semiconductor charge qubit," *Phys. Rev. Lett.*, vol. 105, p. 246804, 2010.

[138] L. M. K. Vandersypen, H. Bluhm, J. S. Clarke, A. S. Dzurak, R. Ishihara, A. Morello, D. J. Reilly, L. R. Schreiber, and M. Veldhorst, "Interfacing spin qubits in quantum dots and donors–hot, dense, and coherent," *npj Quantum Inf.*, vol. 3, p. 34, 2017.

[139] M. Veldhorst, H. Eenink, C.-H. Yang, and A. S. Dzurak, "Silicon cmos architecture for a spin-based quantum computer," *Nature Communications*, vol. 8, no. 1, pp. 1–8, 2017.

[140] A. Mills, D. Zajac, M. Gullans, F. Schupp, T. Hazard, and J. Petta, "Shuttling a single charge across a one-dimensional array of silicon quantum dots," *Nature Communications*, vol. 10, no. 1, pp. 1–6, 2019.

[141] N. Holman, J. Dodson, L. Edge, S. Coppersmith, M. Friesen, R. McDermott, and M. Eriksson, "Microwave engineering for semiconductor quantum dots in a cqed architecture," *Appl. Phys. Lett.*, vol. 117, p. 083502, 2020.

[142] K. Takeda, A. Noiri, T. Nakajima, J. Yoneda, T. Kobayashi, and S. Tarucha, "Quantum tomography of an entangled three-spin state in silicon," 2020.

[143] T. Ando, A. B. Fowler, and F. Stern, "Electronic properties of two-dimensional systems," *Rev. Mod. Phys.*, vol. 54, no. 2, pp. 437–672, Jan 1982.

[144] C. B. Simmons, T. S. Koh, N. Shaji, M. Thalakulam, L. J. Klein, H. Qin, H. Luo, D. E. Savage, M. G. Lagally, A. J. Rimberg, R. Joynt, R. Blick, M. Friesen, S. N. Coppersmith, and M. A. Eriksson, "Pauli spin blockade and lifetime-enhanced transport in a Si/SiGe double quantum dot," *Phys. Rev. B*, vol. 82, p. 245312, 2010.

[145] Z. Shi, C. B. Simmons, J. Prance, J. K. Gamble, M. Friesen, D. E. Savage, M. G. Lagally, S. N. Coppersmith, and M. A. Eriksson, "Tunable singlet-triplet splitting in a few-electron Si/SiGe quantum dot," *Appl. Phys. Lett.*, vol. 99, p. 233108, 2011.

[146] A. Jones, E. Pritchett, E. Chen, T. Keating, R. Andrews, J. Blumoff, L. De Lorenzo, K. Eng, S. Ha, A. Kiselev, S. Meenehan, S. Merkel, J. Wright, L. Edge, R. RS, R. MT, B. MG, and A. Hunter, "Spin-blockade spectroscopy of si/si-ge quantum dots," *Physical Review Applied*, vol. 12, no. 1, p. 014026, 2019, arXiv:1809.08320.

[147] A. Hollmann, T. Struck, V. Langrock, A. Schmidbauer, F. Schauer, T. Leonhardt, K. Sawano, H. Riemann, N. V. Abrosimov, D. Bougeard, and L. R. Schreiber, "Large, tunable valley splitting and single-spin relaxation mechanisms in a $\mathrm{Si/si}_x\mathrm{ge}_{1-x}$ quantum dot," *Phys. Rev. Applied*, vol. 13, p. 034068, Mar 2020.

[148] J. M. Elzerman, R. Hanson, L. H. Willems van Beveren, L. M. K. Vandersypen, and L. P. Kouwenhoven, "Excited-state spectroscopy on a nearly closed quantum dot via charge detection," *Appl. Phys. Lett.*, vol. 84, pp. 4617–4619, 2004.

[149] J. K. Gamble, P. Harvey-Collard, N. T. Jacobson, A. D. Baczewski, E. Nielsen, L. Maurer, I. Montaño, M. Rudolph, M. Carroll, C. Yang, A. Rossi, A. Dzurak, and R. P. Muller, "Valley splitting of single-electron si mos quantum dots," *Appl. Phys. Lett.*, vol. 109, no. 25, p. 253101, 2016.

[150] L. DiCarlo, H. J. Lynch, A. C. Johnson, L. I. Childress, K. Crockett, and C. M. Marcus, "Differential charge sensing and charge delocalization in a tunable double quantum dot," *Phys. Rev. Lett.*, vol. 92, no. 22, p. 226801, 2004.

[151] W. H. Lim, F. A. Zwanenburg, H. Huebl, M. Möttönen, K. W. Chan, A. Morello, and A. S. Dzurak, "Observation of the single-electron regime in a highly tunable silicon quantum dot," *Appl. Phys. Lett.*, vol. 95, no. 24, p. 242102, Jan 2009.

[152] W. H. Lim, C. H. Yang, F. A. Zwanenburg, and A. S. Dzurak, "Spin filling of valley–orbit states in a silicon quantum dot," *Nanotechnology*, vol. 22, no. 33, p. 335704, jul 2011.

[153] K. Ono, D. G. Austing, Y. Tokura, and S. Tarucha, "Current rectification by pauli exclusion in a weakly coupled double quantum dot system," *Science*, vol. 297, p. 1313.

[154] M. D. Shulman, O. E. Dial, S. P. Harvey, H. Bluhm, V. Umansky, and A. Yacoby, "Demonstration of entanglement of electrostatically coupled singlet-triplet qubits," *Science*, vol. 336, pp. 202–205, 2012.

[155] S. M. Reimann, M. Koskinen, and M. Manninen, "Formation of wigner molecules in small quantum dots," *Phys. Rev. B*, vol. 62, p. 8108, 2000.

[156] M. Rontani, C. Cavazzoni, D. Bellucci, and G. Goldoni, "Full configuration interaction approach to the few-electron problem in artificial atoms," *The Journal of Chemical Physics*, vol. 124, no. 12, p. 124102, 2006.

[157] A. Ghosal, A. D. Güçlü, C. J. Umrigar, D. Ullmo, and H. U. Baranger, "Incipient wigner localization in circular quantum dots," *Phys. Rev. B*, vol. 76, p. 085341, Aug 2007. [Online]. Available: https://link.aps.org/doi/10.1103/PhysRevB.76.085341

[158] I. Shapir, A. Hamo, S. Pecker, C. P. Moca, Ö. Legeza, G. Zarand, and S. Ilani, "Imaging the electronic wigner crystal in one dimension," *Science*, vol. 364, pp. 870–875, 2019.

[159] A. M. Mintairov, J. Kapaldo, J. L. Merz, S. Rouvimov, D. V. Lebedev, N. A. Kalyuzhnyy, S. A. Mintairov, K. G. Belyaev, M. V. Rakhlin, A. A. Toropov, P. N. Brunkov, A. S. Vlasov, Y. Zadiranov, S. A. Blundell, A. M. Mozharov, I. Mukhin, M. Yakimov, S. Oktyabrsky, A. V. Shelaev, and V. A. Bykov, "Control of wigner localization and electron cavity effects in near-field emission spectra of In(Ga)P/GaInP quantum-dot structures a." *Phys. Rev. B*, vol. 97, no. 19, p. 195443, May 2018.

[160] S. Kalliakos, M. Rontani, V. Pellegrini, C. P. García, A. Pinczuk, G. Goldoni, E. M. ad Loren N. Pfeiffer, and K. W. West, "A molecular state of correlated electrons in a quantum dot," *Nat. Phys.*, vol. 4, pp. 467–471, Apr 2008.

[161] L. H. Kristinsdóttir, J. C. Cremon, H. A. Nilsson, H. Q. Xu, L. Samuelson, H. Linke, A. Wacker, and S. M. Reimann, "Signatures of wigner localization in epitaxially grown nanowires," *Phys. Rev. B*, vol. 83, p. 041101, Jan 2011. [Online]. Available: https://link.aps.org/doi/10.1103/PhysRevB.83.041101

[162] L. A. Tracy, D. R. Luhman, S. M. Carr, N. C. Bishop, G. A. T. Eyck, T. Pluym, J. R. Wendt, M. P. Lilly, and M. S. Carroll, "Single shot spin readout using a cryogenic high-electron-mobility transistor amplifier at sub-kelvin temperatures," *Appl. Phys. Lett.*, vol. 108, p. 063101, 2016.

[163] S. A. Studenikin, J. Thorgrimson, G. C. Aers, A. Kam, P. Zawadzki, Z. R. Wasilewski, A. Bogan, and A. S. Sachrajda, "Enhanced charge detection of spin qubit readout via an intermediate state," *Appl. Phys. Lett.*, vol. 101, p. 233101, 2012.

[164] "*NIST Digital Library of Mathematical Functions*," http://dlmf.nist.gov/, Release 1.0.21 of 2018-12-15, f. W. J. Olver, A. B. Olde Daalhuis, D. W. Lozier, B. I. Schneider, R. F. Boisvert, C. W. Clark, B. R. Miller and B. V. Saunders, eds. [Online]. Available: http://dlmf.nist.gov/

[165] N. E. Penthorn, J. S. Schoenfield, L. F. Edge, and H. Jiang, "Direct measurement of electron intervalley relaxation in a Si/Si-Ge quantum dot," *Phys. Rev. Applied*, vol. 14, p. 054015, Nov 2020. [Online]. Available: https://link.aps.org/doi/10.1103/PhysRevApplied.14.054015

[166] K. MacLean, S. Amasha, I. P. Radu, D. M. Zumbühl, M. A. Kastner, M. P. Hanson, and A. C. Gossard, "Energy-dependent tunneling in a quantum dot," *Phys. Rev. Lett.*, vol. 98, no. 3, p. 036802, Jan 2007.

[167] R. Hanson, L. P. Kouwenhoven, J. R. Petta, S. Tarucha, and L. M. K. Vandersypen, "Spins in few-electron quantum dots," *Rev. Mod. Phys.*, vol. 79, pp. 1217–1265, 2007.

[168] W. G. van der Wiel, S. De Franceschi, J. M. Elzerman, T. Fujisawa, S. Tarucha, and L. P. Kouwenhoven, "Electron transport through double quantum dots," *Rev. Mod. Phys.*, vol. 75, pp. 1–22, 2003.

[169] J. M. Elzerman, R. Hanson, J. S. Greidanus, L. H. Willems van Beveren, S. De Franceschi, L. M. K. Vandersypen, S. Tarucha, and L. P. Kouwenhoven, "Few-electron quantum dot circuit with integrated charge read out," *Phys. Rev. B*, vol. 67, p. 161308, Jan 2003.

[170] C. Kittel, H. Charles Kittel, K. Charles, H. Kroemer, and K. Herbert, *Thermal Physics*. W. H. Freeman, 1980.

[171] M. Stopa, "Quantum dot self-consistent electronic structure and the coulomb blockade," *Phys. Rev. B*, vol. 54, no. 19, pp. 13 767–13 783, 1996.

[172] B. P. Wuetz, M. P. Losert, A. Tosato, M. Lodari, P. L. Bavdaz, L. Stehouwer, P. Amin, J. S. Clarke, S. N. Coppersmith, A. Sammak, M. Veldhorst, M. Friesen, and G. Scappucci, "Effect of quantum hall edge strips on valley splitting in silicon quantum wells," *Phys. Rev. Lett.*, vol. 125, p. 186801, Oct 2020.

[173] D. A. Lidar and T. A. Brun, *Quantum Error Correction*. Cambridge University Press, 2013.

[174] S. B. Bravyi and A. Y. Kitaev, "Quantum codes on a lattice with boundary," *eprint arXiv:quant-ph/9811052*, Nov. 1998.

[175] R. Raussendorf and J. Harrington, "Fault-tolerant quantum computation with high threshold in two dimensions," *Phys. Rev. Lett.*, vol. 98, p. 190504, May 2007. [Online]. Available: http://link.aps.org/doi/10.1103/PhysRevLett.98.190504

[176] E. Kawakami, T. Jullien, P. Scarlino, D. R. Ward, D. E. Savage, M. G. Lagally, V. V. Dobrovitski, M. Friesen, S. N. Coppersmith, M. A. Eriksson, and L. M. K. Vandersypen, "Gate fidelity and coherence of an electron spin in an si/sige quantum dot with micromagnet," *Proc. Nat. Acad. Sci.*, vol. 113, no. 42, pp. 11 738–11 743, 2016. [Online]. Available: http://www.pnas.org/content/113/42/11738.abstract

[177] P. Scarlino, E. Kawakami, T. Jullien, D. R. Ward, D. E. Savage, M. G. Lagally, M. Friesen, S. N. Coppersmith, M. A. Eriksson, and L. M. K. Vandersypen, "Dressed photon-orbital states in a quantum dot: Intervalley spin resonance," *Phys. Rev. B*, vol. 95, p. 165429, Apr 2017. [Online]. Available: https://link.aps.org/doi/10.1103/PhysRevB.95.165429

[178] D. P. DiVincenzo and P. Aliferis, "Effective fault-tolerant quantum computation with slow measurements," *Phys. Rev. Lett.*, vol. 98, p. 020501, Jan 2007. [Online]. Available: http://link.aps.org/doi/10.1103/PhysRevLett.98.020501

[179] M. A. Nielsen and I. L. Chuang, *Quantum Computation and Quantum Information*. Cambridge University Press, 2000.

[180] V. Nebendahl, H. Häffner, and C. F. Roos, "Optimal control of entangling operations for trapped-ion quantum computing," *Phys. Rev. A*, vol. 79, p. 012312, Jan 2009. [Online]. Available: https://link.aps.org/doi/10.1103/PhysRevA.79.012312

[181] P. Schindler, J. T. Barreiro, T. Monz, V. Nebendahl, D. Nigg, M. Chwalla, M. Hennrich, and R. Blatt, "Experimental repetitive quantum error correction," *Science*, vol. 332, no. 6033, pp. 1059–1061, 2011. [Online]. Available: http://science.sciencemag.org/content/332/6033/1059

[182] C.-K. Li, M. Nakahara, Y.-T. Poon, N.-S. Sze, and H. Tomita, "Recovery in quantum error correction for general noise without measurement," *Quantum Info. Comput.*, vol. 12, no. 1-2, pp. 149–158, Jan. 2012. [Online]. Available: http://dl.acm.org/citation.cfm?id=2231036.2231046

[183] M. D. Reed, "Entanglement and Quantum Error Correction with Superconducting Qubits," Ph.D. dissertation, Yale University, 2014.

[184] V. Nebendahl, "Optimized quantum error-correction codes for experiments," *Phys. Rev. A*, vol. 91, p. 022332, Feb 2015. [Online]. Available: https://link.aps.org/doi/10.1103/PhysRevA.91.022332

[185] G. A. Paz-Silva, G. K. Brennen, and J. Twamley, "Fault tolerance with noisy and slow measurements and preparation," *Phys. Rev. Lett.*, vol. 105, p. 100501, Aug 2010. [Online]. Available: http://link.aps.org/doi/10.1103/PhysRevLett.105.100501

[186] D. Crow, R. Joynt, and M. Saffman, "Improved error thresholds for measurement-free error correction," *Phys. Rev. Lett.*, vol. 117, p. 130503, Sep 2016. [Online]. Available: http://link.aps.org/doi/10.1103/PhysRevLett.117.130503

[187] K. Fujii, M. Negoro, N. Imoto, and M. Kitagawa, "Measurement-free topological protection using dissipative feedback," *Phys. Rev. X*, vol. 4, p. 041039, Dec 2014. [Online]. Available: http://link.aps.org/doi/10.1103/PhysRevX.4.041039

[188] Y. C. Cheng and R. J. Silbey, "Microscopic quantum dynamics study on the noise threshold of fault-tolerant quantum error correction," *Phys. Rev. A*, vol. 72, p. 012320, Jul 2005. [Online]. Available: https://link.aps.org/doi/10.1103/PhysRevA.72.012320

[189] Y. Tomita and K. M. Svore, "Low-distance surface codes under realistic quantum noise," *Phys. Rev. A*, vol. 90, p. 062320, Dec 2014. [Online]. Available: http://link.aps.org/doi/10.1103/PhysRevA.90.062320

[190] J. Edmonds, "Paths, trees and flowers," *Canadian Journal of Mathematics*, vol. 17, pp. 449–467, 1965.

[191] E. Knill, "Quantum computing with realistically noisy devices," *Nature*, vol. 434, p. 39, Mar 2005. [Online]. Available: http://www.nature.com/nature/journal/v434/n7029/abs/nature03350.html#abs

[192] X. Mi, J. V. Cady, D. M. Zajac, P. W. Deelman, and J. R. Petta, "Strong coupling of a single electron in silicon to a microwave photon," *Science*, vol. 355, pp. 156–158, 2016. [Online]. Available: http://science.sciencemag.org/content/early/2016/12/21/science.aal2469

[193] J. R. Wootton, A. Peter, J. R. Winkler, and D. Loss, "A proposal for a minimal surface code experiment," *ArXiv e-prints*, Aug. 2016.

[194] S. Aaronson and D. Gottesman, "Improved simulation of stabilizer circuits," *Phys. Rev. A*, vol. 70, p. 052328, Nov 2004. [Online]. Available: http://link.aps.org/doi/10.1103/PhysRevA.70.052328

[195] D. S. Wang, A. G. Fowler, A. M. Stephens, and L. C. L. Hollenberg, "Threshold error rates for the toric and planar codes," *Quantum Info. Comput.*, vol. 10, no. 5, pp. 456–469, May 2010. [Online]. Available: http://dl.acm.org/citation.cfm?id=2011362.2011368

[196] A. G. Fowler, A. C. Whiteside, and L. C. L. Hollenberg, "Towards practical classical processing for the surface code: Timing analysis," *Phys. Rev. A*, vol. 86, p. 042313, Oct 2012. [Online]. Available: https://link.aps.org/doi/10.1103/PhysRevA.86.042313

[197] C. Barthel, M. Kjærgaard, J. Medford, M. Stopa, C. M. Marcus, M. P. Hanson, and A. C. Gossard, "Fast sensing of double-dot charge arrangement and spin state with a radio-frequency sensor quantum dot," *Phys. Rev. B*, vol. 81, p. 161308, Apr 2010. [Online]. Available: https://link.aps.org/doi/10.1103/PhysRevB.81.161308

[198] J. Petta, A. Johnson, J. Taylor, A. Yacoby, M. Lukin, C. Marcus, M. Hanson, and A. Gossard, "Charge and spin manipulation in a few-electron double dot," *Physica E: Low-dimensional Systems and Nanostructures*, vol. 34, no. 1, pp. 42 – 46, 2006. [Online]. Available: http://www.sciencedirect.com/science/article/pii/S138694770600083X